DYNAMIC THEORY OF VOLUME HOLOGRAPHIC RECORDING AND READOUT IN ELECTRO-OPTIC CRYSTALS

A THESIS

Presented to

The Faculty of the Graduate Division

by

Robert Magnusson

In Partial Fulfillment

of the Requirements for the Degree

Doctor of Philosophy

in the School of Electrical Engineering

Georgia Institute of Technology

November 1976

DYNAMIC THEORY OF VOLUME HOLOGRAPHIC RECORDING AND READOUT IN ELECTRO-OPTIC CRYSTALS

Approved:

T. K. Gaylord, Chairman

W. R. Callen

J. D. Norgard

Date approved by Chairman 11/19/76

This dissertation is dedicated to

my aunt

KRISTIN H. EYFELLS

for her continuous inspiration.

ACKNOWLEDGMENTS

I hereby express my sincere thanks to my thesis advisor, Dr. T. K. Gaylord, whose deep understanding, encouragement, and guidance were of fundamental academic and personal importance during the course of this work. I also thank Dr. W. R. Callen and Dr. J. D. Norgard for serving on the reading committee and for their many useful comments on this work. Many interesting and entertaining discussions with my colleagues Dr. S. F. Su and Mr. J. E. Weaver are also acknowledged. In addition, I am grateful to Mrs. Kathy Massett for her skillful typing of this thesis. The financial assistance of the School of Electrical Engineering is greatly appreciated.

TABLE OF CONTENTS

Page

ACKNOWLEDGMENTS iii

LIST OF SYMBOLS vi

LIST OF ILLUSTRATIONS x

SUMMARY xx

Chapter

I. INTRODUCTION 1

1.1 Basic Ideas and Definitions
1.2 Brief History
1.3 Volume Hologram Applications
1.4 Thesis Motivation
1.5 Thesis Overview

II. DYNAMIC HOLOGRAM THEORY 6

2.1 Perspective
2.2 Analytical Techniques
2.3 Model and Dynamic Theory
2.3.1 Model
2.3.2 Material Response
2.3.3 Equations
2.4 Internal Grating Profiles
2.5 Time Dependent Exposure Sensitivity

III. CALCULATED RESULTS AND EXPERIMENTAL BEHAVIOR. 19

3.1 Calculational Procedure
3.2 Writing
3.3 Readout
3.4 Angular Selectivity
3.5 Discussion
3.6 Conclusions

IV. THEORETICAL TERMINAL CHARACTERISTICS AND ASSOCIATED INTERNAL PROFILES 45

4.1 Introduction

TABLE OF CONTENTS

Page

4.2 Writing Diffraction Efficiency
4.3 Internal and External Features of Typical Holograms
4.4 Angular Selectivity of Typical Holograms
4.5 Dynamic Readout of Typical Holograms

V. QUANTITATIVE THEORY-EXPERIMENT COMPARISON 97

5.1 Experimental System
5.2 Evaluation of Experimental Parameters
5.2.1 Absorption Coefficients
5.2.2 Incident Fields and Diffraction Efficiency
5.2.3 Exposure Sensitivity
5.3 Writing
5.4 Readout
5.5 Angular Selectivity
5.6 Discussion

VI. LASER SCATTERING EFFECTS. 123

6.1 Introduction
6.2 Analytical Description
6.3 Results
6.4 Discussion

VII. CONCLUSIONS AND RECOMMENDATIONS 134

7.1 Conclusions
7.2 Future Research

APPENDIX A. 140

APPENDIX B. 147

APPENDIX C. 158

APPENDIX D. 159

APPENDIX E. 161

BIBLIOGRAPHY. 163

VITA. 169

LIST OF SYMBOLS

$a, a(t)$	refractive index exposure sensitivity, $(V/m)^{-2}sec^{-1}$
$b, b(t)$	exposure sensitivity for absorption changes, $V^{-2}m\ sec^{-1}$
c	velocity of light in vacuum, m/sec
d	thickness of crystal, mm
$\bar{E}$	total rms complex electric field, V/m
E_o	incident electric field amplitude at input face of crystal, V/m
$\mathcal{E}$	exposure, $(V/m)^2 sec$
I_d	diffracted laser beam intensity, W/m^2
I_o	incident laser beam intensity, W/m^2
I_r	reflected laser beam intensity, W/m^2
I_t	transmitted laser beam intensity, W/m^2
I_{rr}	interference pattern produced by R-beam readout of a cosine grating
I_{ss}	interference pattern produced by S-beam readout of a cosine grating
j	the imaginary unit
k	$-2\beta_o \sin\theta$
K	propagation constant, m^{-1}
$\bar{K}$	wavevector of an incident beam, m^{-1}
$\bar{K}', \bar{K}'_p (p=1,2,3,4)$	wavevector of a diffracted (reconstructed) beam, m^{-1}
$\bar{K}_i$	wavevector of original incident writing beam, m^{-1}
$\bar{K}_s$	wavevector of a scattered wavelet, m^{-1}

LIST OF SYMBOLS

$\Delta\bar{K}_G$	fundamental holographic grating vector, m^{-1}
$\Delta\bar{K}_s$	grating vector for the scattering induced hologram pattern, m^{-1}
ℓ	optics loss factor
M	$\int_o^T \mathrm{Re}\{RS^*\}dt$
n	refractive index
n_o	average refractive index
n_1	holographic refractive index spatial modulation
n_{1c}	amplitude of the refractive index modulation along a cut through the crystal
n_{1p}	amplitude of the refractive index modulation along a peak in the grating
n_{1pa}	n_{1p} averaged over the crystal thickness
Δn	exposure induced change in the refractive index
Δn_{rr}	refractive index change produced by I_{rr}
Δn_{ss}	refractive index change produced by I_{ss}
N	$\int_o^T \mathrm{Im}\{RS^*\}dt$
$\bar{r}$	(x,y,z) position vector
$\hat{r}$	polarization unit vector for the reference wave
R	complex electric field amplitude of the reference wave, V/m
R_o	incident amplitude of the R-wave, V/m
R_r	reflection coefficient
$\hat{s}$	polarization unit vector for the signal wave
S	complex electric field amplitude of the signal wave, V/m
S_o	incident amplitude of the S-wave, V/m

LIST OF SYMBOLS

t	time, sec.
T	exposure time, sec.
$\hat{x}$	unit vector in x-direction
$\hat{z}$	unit vector in z-direction
Z_o	impedance of free space, ohms
α	absorption coefficient, m^{-1}
α_o	average absorption coefficient, m^{-1}
α_1	holographic absorption coefficient spatial modulation, m^{-1}
α'	angle of incidence
α''	refraction angle corresponding to α'
$\Delta\alpha$	exposure induced change in the absorption coefficient
β	$2\pi n/\lambda$
β_o	$2\pi n_o/\lambda$
ϵ_r	relative dielectric constant of the crystal
η	holographic diffraction efficiency
θ	writing angle inside the crystal
θ_1, θ_2	angles of incidence for the original writing beams
ϑ	dephasing measure, m^{-1}
λ	recording wavelength, μm
μ	magnetic permeability, henry/m
$\bar{\rho}$	wavevector of the reference wave, m^{-1}
ρ_x, ρ_z	x and z components of $\bar{\rho}$, m^{-1}

LIST OF SYMBOLS

$\bar{\sigma}$	wavevector of the signal wave, m^{-1}
σ_x, σ_z	x and z components of $\bar{\sigma}$, m^{-1}
σ'	magnitude of the wavevector of the diffracted wave, m^{-1}
ϕ_p (p=1,2,...6)	diffraction cone angles
ϕ_α	spatial phase difference between the hologram-forming light interference pattern and the resulting absorption grating
ϕ_n	spatial phase difference between the hologram-forming light interference pattern and the resulting refractive index grating
ϕ_r	phase of R-wave
ϕ_s	phase of S-wave
ψ	beam intensity ratio, SS*/RR*
ω	optical angular frequency, sec^{-1}

superscripts

*	complex conjugate
'	readout quantity

LIST OF ILLUSTRATIONS

Figure		Page
1	Model for (a) Hologram Recording, and (b) Hologram Reading	10
2	Calculated Hologram Writing Characteristic Exhibiting a Saturation-Like Appearance. Hologram Thickness is 2.00 mm, a = 10^{-12}(volt/m)$^{-2}$sec^{-1}, $\phi_n = 90°$, $\alpha_o = 0$, and Other Parameters as Given in Sec. 3.1.	22
3	Experimental Saturation-Like Hologram Writing Characteristic in Lithium Niobate. Sample Thickness is 3 mm, λ = 0.488 μm, and the Power Density is 6×10^{-3} W/mm^2 (after Ref. 33)	23
4	Experimental Saturation-Like Hologram Writing Characteristic in Lithium Niobate. Sample Thickness is 5 mm, λ = 0.5145 μm, and the Power Density is 1.09×10^{-2} W/mm^2 (after Ref. 28)	23
5	Calculated Oscillatory Hologram Writing Characteristic with Decreasing Amplitude and Increasing Period of the Diffraction Efficiency Oscillations. Hologram Thickness is 2.00 mm, a = 10^{-11} (volt/m)$^{-2}$sec^{-1}, $\phi_n = 90°$, $\alpha_o = 0$, and Other Paramters as Given in Sec. 3.1.	24
6	Experimental Oscillatory Hologram Writing Characteristic for 1.66 mm Thick, Iron-Doped Lithium Niobate Crystal. Writing Beam Polarizations are in the Plane of Incidence and the Experimental Configuration is as Shown in the Figure Inset.	25
7	Experimental Oscillatory Hologram Writing Characteristic in Lithium Niobate. Hologram Thickness is 2 mm, λ = 0.488 μm, and the Power Density is 5×10^{-4} W/mm^2 (after Ref. 33)	26
8	Experimental (a) Oscillatory and (b) Saturating Hologram Writing Characteristics in Lithium Niobate. Crystal Thickness is 2.5 mm, λ = 0.4880 μm, and the Power Density is 10^{-2} W/mm^2 (after Ref. 34)	26

LIST OF ILLUSTRATIONS

Figure		Page
9	Calculated Oscillatory Hologram Writing Characteristic with Diffraction Efficiency Minima Near 0%. Hologram Thickness is 2.00 mm, $a = 10^{-11}$ (volts/m)$^{-2}$ sec^{-1}, $\phi_n = 60°$, $\alpha_o = 10^2 m^{-1}$, and Other Parameters as Given in Sec. 3.1.	27
10	Experimental Oscillatory Hologram Writing Characteristic in a Photopolymer. Hologram Thickness is 1.8 mm and the Power Density is 10^{-6}W/mm^2 (after Ref. 8)	27
11	Calculated Exponential-Like Reading Characteristic. Note Slight Rise in Efficiency at a Reading Time of 200 Seconds. Hologram Thickness is 2.00 mm, $a = 10^{-12}$ (volt/m)$^{-2}$sec^{-1}, $\phi_n = 90°$, $\alpha_o = 0$, Readout with R Beam, and Other Parameters as Given in Sec. 3.1. The Original Hologram was Recorded Using These Same Parameters and an Exposure Time of 40 Seconds.	29
12	Experimental (a) Writing and (b) Reading Characteristics of Volume Holograms in Lithium Niobate. Crystal Thickness is 7 mm, $\lambda = 0.488$ μm, and the Power Density is $6x10^{-3}$ W/mm^2. The Reading Beam Orientation Relative to the Crystal C-Axis is shown in the Inset (after Ref. 20).	31
13	Experimental Exponential-Like Hologram Reading Characteristic in Lithium Niobate. Hologram Thickness is 5 mm, $\lambda = 0.5145$ μm, and the Power Density is $5.9x10^{-3}$ W/mm^2 (after Ref. 28).	31
14	Experimental Exponential-Like Reading Characteristic for a 1.66 mm Thick, Iron-Doped Lithium Niobate Crystal. Small Amplitude Diffraction Efficiency Oscillations are Present at Low Efficiencies. Reading Beam Polarization is in the Plane of Incidence and the Experimental Configuration is as Shown in the Figure Inset	32
15	Calculated Reading Characteristics Illustrating the Effect of Reading Beam Interchange. For R-Beam Readout, Oscillations Occur at Low Diffraction Efficiencies after Erasure. For S-Beam Readout, the Oscillations Occur at High Efficiencies after Enhancement. Hologram Thickness is 2.00 mm, $a = 10^{-11}$	

LIST OF ILLUSTRATIONS

Figure		Page
15	$(volt/m)^{-2}sec^{-1}$, $\phi_n = 90°$, $\alpha_o = 10^2 m^{-1}$, and Other Parameters as Given in Sec. 3.1. The Original Hologram was Recorded Using these Same Parameters and an Exposure Time of 10 Seconds.	33
16	Experimentally Observed Effect of Changing the Reading Beam Direction Relative to the Crystal C-Axis on the Hologram Reading Characteristic. The $LiNbO_3$ Crystal is 9 mm Thick and $\lambda = 0.488$ μm (after Ref. 39)	34
17	Experimentally Observed Effect of Changing the Reading Beam Direction Relative to the Crystal C-Axis. (a) Hologram Reading Characteristics. (b) Experimental Configuration. The $LiNbO_3$ Crystal is 1 mm Thick, $\lambda = 0.53$ μm, and $\eta_o = 1.71 \times 10^{-4}$. Self-Enhancement Occurs for the Reading Beam at $-\phi_{Bragg}$. Erasure Occurs for the Beam at $+\phi_{Bragg}$ (after Ref. 48)	34
18	Calculated Reading Characteristic Showing Diffraction Efficiency Oscillations Followed by Rapid Decay. Hologram Thickness is 2.00 mm, $a = 10^{-11}$ $(volt/m)^{-2}sec^{-1}$, $\phi_n = 0°$, $\alpha_o = 0$, Readout with R Beam, and Other Parameters as Given in Sec. 3.1. The Original Hologram was Recorded Using these Same Parameters and an Exposure Time of 35 Seconds	35
19	Experimental Hologram Reading Characteristic Exhibiting Initial Oscillations Followed by Monotonic Decay. The $LiNbO_3$ Sample is 2.5 mm Thick, $\lambda = 0.488$ μm, and the Power Density is 10^{-2} W/mm^2 (after Ref. 34)	36
20	Calculated Oscillatory Reading Characteristic Showing Large Variations in the Amplitude and Period of the Diffraction Efficiency Oscillations. Hologram Thickness is 2.00 mm, $a = 10^{-11}$ $(volt/m)^{-2}sec^{-1}$, $\phi_n = 0°$, $\alpha_o = 0$, Readout with R Beam, and Other Parameters as Given in Sec. 3.1. The Original Hologram was Recorded Using these Same Parameters and an Exposure Time of 10 Seconds.	36

LIST OF ILLUSTRATIONS

Figure		Page
21	Experimental Oscillatory Reading Characteristic for a 1.66 mm Thick, Iron-Doped Lithium Niobate Crystal. A Wide Variation in the Amplitude and Period of the Diffraction Efficiency Oscillations is Apparent. Reading Beam Polarization is in the Plane of Incidence and the Experimental Configuration is as Shown in the Figure Inset	37
22	Experimental and Calculated Angular Selectivity Exhibiting Zero Diffraction Efficiency at Minima. The Hologram is 1.66 mm Thick, Iron-Doped Lithium Niobate Crystal. Experimentally, the Hologram was Written with a Wavelength of 514.5 nm, a Total Power Density of 3.5 mw/mm^2, External Angles of Incidence of $\pm 5.00°$, a Writing Time of 5 sec., Polarization in the Plane of Incidence, and the Configuration Shown in the Inset of Figure 6. The Angular Selectivity was Measured with a Low Power Beam of the Same Wavelength. The Calculated Curve is for a Hologram of Thickness 1.66 mm, Written with R_o = 571 v/m, S_o = 518 v/m, for 5 sec. with a = 3.8×10^{-12} (volt/m)$^{-2}$sec^{-1}, $\phi_n = 0°$, and $\alpha_o = 0$, These Parameters Being Estimated from the Experimental Conditions	40
23	Calculated Angular Selectivity Exhibiting Nonzero Diffraction Efficiency at Minima. Nonzero Minima are Characteristic of a Phase Holographic Grating Having a Variation in Index of Refraction Through the Thickness of the Material. The Refractive Index Profile is Shown in the Inset. Hologram Thickness is 2.00 mm, a = 10^{-11} (volt/m)$^{-2}$sec^{-1}, $\phi_n = 90°$, $\alpha_o = 0$, and the Writing Time is 5 sec	41
24	Calculated Angular Selectivity Showing the Disappearance of Diffraction Efficiency Minima. The Same Condition as Figure 24 Prevail with a Longer Writing Time of 30 sec. The Increased Nonuniformity of the Grating Profile is Shown in the Inset.	42
25	Calculated Writing Characteristics for Lossless Holograms. $R_o = S_o$ = 1000 volt/m and $\alpha_o = 0$.	48

LIST OF ILLUSTRATIONS

Figure		Page
26	Calculated Writing Characteristics for Lossless Holograms Using Unequal Boundary Values. R_o = 1000 volt/m, S_o = 500 volt/m, and α_o = 0.	49
27	Same as Figure 26 but with S_o = 100 volt/m.	50
28	Same as Figure 26 but with R_o = 500 volt/m and S_o = 1000 volt/m	52
29	Same as Figure 28 but with R_o = 100 volt/m.	53
30	Calculated Writing Characteristics for Realistic Lossy Holograms. $R_o = S_o$ = 1000 volt/m and α_o = 100 m^{-1}	54
31	Calculated Writing Characteristics for Realistic Lossy Holograms Using Unequal Boundary Values. R_o = 1000 volt/m, S_o = 500 volt/m, and α_o = 100 m^{-1}	56
32	Same as Figure 31 but with R_o = 500 volt/m and S_o = 1000 volt/m	57
33	Calculated Grating Peak Amplitudes Produced by the Writing Processes of Figure 31. T = 50 sec	58
34	Calculated Grating Peak Amplitudes Produced by the Writing Processes of Figure 32. T = 50 sec	59
35	Calculated Writing Characteristics Using a Time Dependent Exposure Sensitivity $a = a_o \exp(-t/T_o)$. $a_o = 10^{-11}$ $(volt/m)^{-2} sec^{-1}$, T_o = 20 sec, $S_o = R_o$ = 1000 volt/m and α_o = 100 m^{-1}.	61
36	Same as Figure 35 but with T_o = 10 sec.	62
37	Calculated Grating Profiles at a Selected x-Value Corresponding to the Holograms of Figure 30. T = 50 sec	64
38	Calculated Grating Peak Amplitudes Corresponding to the Holograms of Figure 30. T = 50 sec.	65
39	Calculated Spatial Phase Variations of the Grating Peaks of Figure 38.	66

LIST OF ILLUSTRATIONS

Figure		Page
40	Calculated Distributions of the Irradiances of the Signal and Reference Waves Corresponding to the Holograms of Figure 30. T = 50 sec	67
41	Calculated Phase Differences of the Writing Waves Corresponding to the Holograms of Figure 30. T = 50 sec.	69
42	Calculated Time-Variations of the Thickness Average of the Grating Peak Amplitudes Corresponding to the Holograms of Figure 30	70
43	Calculated Temporal Variations of the Transmitted Waves (Z=1) Corresponding to the Holograms of Figure 30.	72
44	Calculated Temporal Variations of the Phase Differences of the Transmitted Waves of Figure 43.	74
45	Calculated Temporal Evolution of the Angular Selectivity Characteristic Corresponding to the Hologram with ϕ_n = 0 in Figure 30	75
46	Calculated Temporal Evolution of the Grating Peak Amplitude Corresponding to Figure 45	76
47	Same as Figure 45 but with ϕ_n = 45°. Vertical Dashed Line Indicates Position of Bragg Angle	78
48	Calculated Temporal Evolution of the Grating Peak Amplitude Corresponding to Figure 47	79
49	Calculated Temporal Evolution of the Grating Phase Associated with the Grating Peak Amplitudes of Figure 48.	80
50	Same as Figure 45 but with ϕ_n = 90°	81
51	Calculated Temporal Evolution of the Grating Peak Amplitude Corresponding to Figure 50	82

LIST OF ILLUSTRATIONS

Figure		Page
52	Calculated Angular Selectivity Characteristics Corresponding to the Gratings of Figures 38 and 39. T = 50 sec. Vertical Dashed Line Indicates Position of Bragg Angle	84
53	Schematic Explanation of the Erasure-Enhancement Phenomenon. (a) Relative Positions of the Original Grating and the Readout Light Interference Patterns. (b) Relative Grating Positions for $\phi_n = 90°$.	88
54	Calculated Readout Characteristics Corresponding to Initial (T' = 0) Diffraction Efficiency at One-Half First Maxima in Figure 30. $R_o' = 1000$ volt/m and $S_o' = 0$.	90
55	Same as Figure 54 but with $R_o' = 0$ and $S_o' =$ 1000 volt/m	91
56	Calculated Readout Characteristics Corresponding to Initial Diffraction Efficiency at the First Maxima in Figure 30. $R_o' = 1000$ volt/m and $S_o' =$ 0	92
57	Same as Figure 56 but with $R_o' = 0$ and $S_o' =$ 1000 volt/m	93
58	Calculated Readout Characteristics Corresponding to Initial Diffraction Efficiency at the First Minima in Figure 30. $R_o' = 1000$ volt/m and $S_o' = 0$	95
59	Same as Figure 58 but with $R_o' = 0$ and $S_o' =$ 1000 volt/m	96
60	Experimental Configuration for Measuring the Optical Holographic Storage Properties of Electro-Optic Crystals.	98
61	Comparison of Experimental and Theoretical Writing Characteristics. The Recording Material is a Crystal of $LiNbO_3$ Doped with 0.1 Mole % Fe. The Hologram Parameters are: $\lambda = 0.5145$ μm, $\lambda' = 0.6328$ μm, $\alpha_o =$ 87 m^{-1}, $\alpha_o' = 24.8$ m^{-1}, d = 1.86 mm, $\phi_n = 30°$, a = 2.22×10^{-11} $(V/m)^{-2} sec^{-1}$, $R_o = 639$ V/m, and $S_o = 610$ V/m. . .	104

LIST OF ILLUSTRATIONS

Figure — Page

62 Comparison of Experimental and Theoretical Writing Characteristics. The Recording Material is an Anti-Reflection Coated Crystal of $LiNbO_3$ Doped with 0.02 Mole % Fe. The Hologram Parameters are: $\lambda = 0.5145$ μm, $\lambda' = 0.6328$ μm, $\alpha_o = 111\ m^{-1}$, $\alpha_o' = 19.5\ m^{-1}$, $d = 2.12$ mm, $\phi_n = 36°$, $a = 1.96 \times 10^{-11} (V/m)^{-2} sec^{-1}$, $R_o = 671$ V/m, and $S_o = 639$ V/m 105

63 Comparison of Experimental and Theoretical Writing Characteristics. The Recording Material is a Crystal of $LiNbO_3$ Doped with 0.1 Mole % Fe. The Hologram Parameters are: $\lambda = 0.5145$ μm, $\lambda' = 0.6328$ μm, $\alpha_o = 59\ m^{-1}$, $\alpha_o' = 22.8\ m^{-1}$, $d = 1.66$ mm, $\phi_n = 85°$, $a = 5.20 \times 10^{-12} (V/m)^{-2} sec^{-1}$, $R_o = 1181$ V/m, and $S_o = 1130$ V/m. 106

64 Experimentally Observed Writing Characteristics Measured by Periodically Blocking One of the Recording Beams. Thus, Readout is Performed by a Beam Fully Illuminating the Hologram which Enhances the Influence of the Spatially Varying Diffraction Efficiency. As a Result, the Diffraction Efficiency Oscillations are Reduced in Amplitude. 109

65 Comparison of Experimental and Theoretical R-Beam Readout Characteristics. The Recording Material is a Crystal of $LiNbO_3$ Doped with 0.1 Mole % Fe. The Hologram Parameters are: $\lambda = 0.5145$ μm, $\lambda' = 0.6328$ μm, $\alpha_o = 87\ m^{-1}$, $\alpha_o' = 25\ m^{-1}$, $d = 1.86$ mm, $\phi_n = 10°$, $a = 2.4 \times 10^{-11} (V/m)^{-2} sec^{-1}$, $R_o = 636$ V/m, $S_o = 605$ V/m, $T = 5$ sec, $R_o' = 633$ V/m, and $S_o' = 0$ 113

66 Comparison of Experimental and Theoretical S-Beam Readout Characteristics. The Recording Material is a Crystal of $LiNbO_3$ Doped with 0.1 Mole % Fe. The Hologram Parameters are: $\lambda = 0.5145$ μm, $\lambda' = 0.6328$ μm, $\alpha_o = 87\ m^{-1}$, $\alpha_o' = 25\ m^{-1}$, $d = 1.86$ mm, $\phi_n = 0°$, $a = 2.6 \times 10^{-11} (V/m)^{-2} sec^{-1}$, $R_o = 582$ V/m, $S_o = 545$ V/m, $T = 7$ sec, $S_o' = 539$ V/m, and $R_o' = 0$ 114

67 Comparison of Experimental and Theoretical Readout Characteristics. The Recording Material is an Anti-Reflection Coated Crystal of $LiNbO_3$ Doped with 0.1 Mole % Fe. The Hologram Parameters are: $\lambda = 0.5145$ μm, $\lambda' = 0.6328$ μm, $\alpha_o = 158\ m^{-1}$, $\alpha_o' = 28.8\ m^{-1}$, $d = 2.12$ mm, $\phi_n = 15°$, $a = 1.48 \times 10^{-11} (V/m)^{-2} sec^{-1}$, $R_o = 1015$ V/m, $S_o = 973$ V/m, $T = 3$ sec, $R_o' = 1015$ V/m, and $S_o' = 947$ V/m. . 115

LIST OF ILLUSTRATIONS

Figure — Page

68 Comparison of Experimental and Theoretical Angular Selectivity Characteristics. The Recording Material is an Anti-Reflection Coated Crystal of $LiNbO_3$ Doped with 0.1 Mole % Fe. The Hologram Parameters are: $\lambda = 0.5145$ μm, $\lambda' = 0.6328$ μm, $\alpha_o = 109$ m^{-1}, $\alpha_o' = 42.1$ m^{-1}, $d = 1.66$ mm, $\phi_n = 15°$, $a = 5.16 \times 10^{-12}$ $(V/m)^{-2}$ sec^{-1}, $R_o = 1094$ V/m, $S_o = 1064$ V/m, and $T = 10$ sec. Vertical Dashed Line Indicates Position of Bragg Angle 117

69 Comparison of Experimental and Theoretical Angular Selectivity Characteristics. The Recording Material is an Anti-Reflection Coated Crystal of $LiNbO_3$ Doped with 0.02 Mole % Fe. The Hologram Parameters are: $\lambda = 0.5145$ μm, $\lambda' = 0.6328$ μm, $\alpha_o = 107$ m^{-1}, $\alpha_o' = 25.7$ m^{-1}, $d = 2.12$ mm, $\phi_n = 20°$, $a = 9.5 \times 10^{-12}$ $(V/m)^{-2}$ sec^{-1}, $R_o = 1063$ V/m, $S_o = 1030$ V/m, and $T = 4$ sec. Vertical Dashed Line Indicates Position of Bragg Angle 119

70 Comparison of Experimental and Theoretical Angular Selectivity Characteristics. The Recording Material is an Anti-Reflection Coated Crystal of $LiNbO_3$ Doped with 0.02 Mole % Fe. The Hologram Parameters are: $\lambda = 0.5145$ μm, $\lambda' = 0.6328$ μm, $\alpha_o = 107$ m^{-1}, $\alpha_o' = 25.7$ m^{-1}, $d = 2.12$ mm, $\phi_n = 20°$, $a = 8.0 \times 10^{-12}$ $(V/m)^{-2}$ sec^{-1}, $R_o = 1082$ V/m, $S_o = 1049$ V/m, and $T = 15$ sec. Vertical Dashed Line Indicates Position of Bragg Angle 120

71 Typical Observed Diffraction Rings from a Lithium Niobate Crystal in which a Plane Holographic Grating had been Recorded. The Original Writing Beam had a Wavelength $\lambda = 515$ nm and the Subsequent Probing Beam for the Above Photographs was of $\lambda' = 633$ nm and had an Angle of Incidence in (a) of $\theta' = 0°$, Resulting in Cone Angles of $\phi_1 = 5.7°$ and $\phi_2 = -5.7°$ and an Angle of Incidence in (b) of $\theta' = 4.5°$, Resulting in a Cone Angle $\phi_1 = 10.6°$. Note in (b) the First Order Diffracted Beam Just to the Left of the Diffraction Ring. 125

LIST OF ILLUSTRATIONS

Figure		Page
72	Diffraction Ring Pattern Observed During Holographic Recording in an Iron-Doped Lithium Niobate Crystal. The Readout Beam is Incident at the Bragg Angle. The Diffracted Beam is on the Left and the Left and the Transmitted Beam is on the Right of the Picture	126
73	Ewald Sphere Construction Used in Deriving the Relationship Between the Diffraction Cone Angles, ϕ, and the Angle of Incidence, θ'	128
74	Comparison of Theoretical and Experimental Results for a $LiNbO_3$ Crystal Originally Exposed to Two Intersecting Laser Beams of λ = 515 nm having Angles of Incidence Equal to +5° and -5° and Subsequently Probed with a Single Low Power Laser Beam of λ' = 488 nm, 515 nm, and 633 nm. The Theoretical Curves are the Same as Those in Figure 75, the Patterns having been Displaced by $\Delta\theta' = \pm 5°$.	130
75	Comparison of Theoretical and Experimental Results for a $LiNbO_3$ Crystal Originally Exposed to a Single Laser Beam of λ = 515 nm at Normal Incidence and Subsequently Probed with a Laser Beam of λ' = 488 nm, 515 nm, and 633 nm.	132

SUMMARY

It is shown in this dissertation that the dynamic theory of volume holography qualitatively and, to some extent, quantitatively describes all aspects of experimentally observed thick (phase) hologram terminal (output) characteristics measured in electro-optic crystals such as $LiNbO_3$. That is, the description of the formation (recording), static readout (angular selectivity), and dynamic readout of the hologram are all contained in the dynamic theory formalism. The experimentally observed erasure-enhancement effect during dynamic readout is predicted by the theory with correct initial slopes. Angular selectivity patterns predicted may be asymmetric with the maximum diffraction efficiency occurring off the Bragg angle. Thus, it is believed that the dynamic theory is the most comprehensive thick hologram theory presently in existence.

In dynamic theory, the influence of the hologram grating on the electromagnetic fields that produce it is taken into consideration (feedback). Beginning with the wave equation, the governing equations are obtained using coupled-wave techniques. Although the dynamic theory is thus, fundamentally, a macroscopic theory, the microphysics of the charge transport mechanisms operative during hologram formation enter the theory through the grating phase shift relative to the light interference pattern. Therefore, observing the hologram terminal characteristics yields microphysical information.

The theory is then useful as a diagnostic tool as well as for analysis and synthesis of thick hologram behavior.

In addition, in this work, correlations of certain structural features of the hologram gratings to the terminal characteristics are established. It is shown that, as a result of dynamic recording, thick holographic gratings may exhibit significant amplitude and grating phase variations with thickness including grating phase reversal. The reduction in angular selectivity sidelobe definition is found to be associated with general grating amplitude variations with thickness while the asymmetry of the pattern around the Bragg angle is associated with grating phase variations (grating bending). For equal writing beam incident amplitudes, the reduction in maximum obtainable diffraction efficiency corresponds to increased grating amplitude nonuniformity.

It is found that the relative values of the recording beam incident amplitudes, R_o and S_o, can significantly influence the hologram behavior. The writing characteristics calculated with $R_o < S_o$ are drastically different from those obtained for $S_o < R_o$ in a manner consistent with the erasure-enhancement effect observed in thick electro-optic holograms. It is shown that by judiciously applying unequal boundary values it is possible to compensate partially for the otherwise unavoidable loss-induced grating nonuniformity.

An experimental study conducted for this dissertation indicates that the dynamic theory consistently predicts the major features of the experimental behavior. It is believed that hologram aperture

effects are mainly responsible for the quantitative deviations that are largest at the maxima and the minima of the recording characteristics. That is, spatially varying (Gaussian) laboratory beam intensity profiles (as opposed to the theoretical infinite plane waves) and the subsequent distortion of these (due to the hologram being written) are experimentally found to give rise to spatially inhomogeneous diffraction efficiency. This causes less efficient light energy coupling between the transmitted and the diffracted beams and thus limits the amplitude of the diffraction efficiency oscillations.

Finally, as a separate topic, the discovery of laser scattering induced holograms in lithium niobate is reported. Light scattered from material inhomogeneities is shown to interfere with the original incident beam(s) and to record scattering holograms. These effects are externally manifested as diffraction, or scattering, rings. An experimental and theoretical description of these phenomena is given and an excellent agreement is shown.

CHAPTER I

INTRODUCTION

1.1 Basic Ideas and Definitions

In this work a hologram is defined as the record of an interference pattern produced by two coherent optical waves. One of the waves may be information-bearing (the signal wave) but the other (the reference wave) is usually simple (planar or spherical). The hologram stores information about both the amplitudes and relative phases of the different points in the scene (signal) being recorded. This is to be contrasted with photography in which all phase information is lost, yielding a two-dimensional record. The recording of phase relationships accounts for the possible retrieval of truly three-dimensional scenes.

Holography is the science of the construction (writing) and reconstruction (reading) of holograms. The reconstruction is accomplished by illuminating the hologram with a reference wave. The signal wave is then reconstructed via diffraction. Diffraction efficiency is defined as the ratio of the power in the diffracted wave to that in the incident reference wave.

1.2 Brief History

Gabor[1] introduced the concept of holography in 1948. Since then, the field has vastly expanded. The short coherence length of the mercury lamp used in Gabor's early work required an "in line" experimental arrangement, that is, the signal and reference waves propagated

approximately along the same axis. On reconstruction, the superposition of the real and conjugate images is then a very disturbing effect. Later, when the laser with its large coherence length became available, Leith and Upatnieks[2-4] greatly improved the imagery of holograms by separating the axes of the two waves, thus removing the pseudoscopic, real image from the useful, virtual image. If the recording medium is two-dimensional, or thin, the real image is always present. This is because, fundamentally, a thin grating diffracts the input wave into many orders simultaneously. In contrast, thick gratings allow only a single diffracted wave for a given input wave. Denisyuk[5] and van Heerden[6] were the first to consider hologram recording in thick media. In the present work, only thick, or volume, holograms are considered.

1.3 Volume Hologram Applications

It is appropriate to mention briefly some of the applications of volume holograms and volume gratings that account for the intensive research conducted in this area in recent years. The properties on which these applications are based are high diffraction efficiency,[7] wavelength selectivity,[7] angular selectivity,[7] and reduced noise.[8] Thick gratings may be used as highly efficient diffraction gratings, narrow band spectral filters,[9] thick grating lenses,[10] imaging systems capable of spectral resolution of extended objects,[8] wave guides for surface waves,[11] frequency-selective grating reflectors for thin-film distributed feedback lasers,[12] thin-film waveguide couplers,[13,14] and as deflectors and modulators.[15] Thick (volume) holograms are of interest due to their use in high-capacity information storage,[6] color holography,[16] and in white light reconstruction of holograms.[17]

1.4 Thesis Motivation

Of particular interest among these applications is the possibility of high-capacity holographic information storage. The theoretical packing density has been estimated as 8×10^{12} bits/cm^3 for thick hologram storage.[6] To actually achieve such high densities and to implement a functional memory system, a detailed characterization of the basic components of the system is necessary. Adequate development of memory building blocks such as the optical source, beam deflectors, page composer, and detector matrix seems to be within the reach of existing technologies.[18] The biggest obstacle appears to be the lack of understanding of the holographic response of the recording material as the memory storage medium. This has been evidenced in the past by the marked discrepancies between experimental volume holography results and available theoretical descriptions. More basic research on the holographic material response and the associated hologram terminal output (i.e. externally measurable) characteristics is, therefore, of paramount importance.

The selection of materials for holographic memory applications is an important consideration. According to Gaylord[18] the ideal recording material must have the following properties: 1) high sensitivity, 2) high diffraction efficiency, 3) erasable and rewritable, 4) long lifetime of holograms, 5) nonvolatility, 6) nondestructive readout, 7) thick, and 8) high resolution. These requirements lead to the selection of photorefractive materials such as ferroelectric crystals[18] in order to aspire to the goal of achieving all of these characteristics simultaneously. Specifically, iron-doped lithium niobate is a promising

candidate. The experimental work described in this thesis, consequently, involves this material.

In addition to the above-mentioned poorly understood hologram terminal (output) characteristics reported in various materials, light scattering effects have been observed in lithium niobate as well as in other materials which have not been understood. It is the purpose of this thesis to clarify these phenomena and thereby, perhaps, bring ultrahigh-capacity holographic memories closer to reality. The understanding gained will also facilitate reliable implementation of volume holography techniques in integrated optics and in other applications.

1.5 Thesis Overview

In Chapter II, the set of dynamic coupled-wave equations appropriate for the experimental holographic arrangement used in this work is presented. This set of equations is also pertinent to much of the data already published in the literature (the E-mode configuration). The dynamic formalism is much more general and powerful than the previous static approaches.

The dynamic coupled-wave equations are solved by numerical methods in Chapter III. It is shown that a wide variety of published volume holography experimental results are qualitatively explained by the dynamic theory. New experimental results are presented that are also consistent with the theory. This indicates the general applicability of the dynamic theory and supports the model and the assumptions used.

In Chapter IV, the dynamic theory is used to calculate the various terminal (output) characteristics of transmission volume phase

hologram gratings and the associated internal material profiles. Using experimentally realistic parameters, the possible multiformity of the diffraction efficiency characteristics of volume holograms is shown. Also, examples of the spatial and temporal variations of important internal and external holographic features are presented.

Quantitative comparison of the dynamic theory and corresponding experimental data is undertaken in Chapter V. Carefully conducted experiments are used to obtain quantitative estimates on the validity and limitations of the dynamic theory in describing the terminal characteristics of volume holograms recorded in iron-doped lithium niobate.

Chapter VI deals with light scattering phenomena observed in iron-doped lithium niobate crystals. It is shown that these effects are due to laser scattering induced holographic patterns recorded in the thick material. An analytical description of these effects is given. It is important to study and to understand these scattering phenomena since they may represent a possible limitation of lithium niobate for some applications.

Finally, in Chapter VII, the major conclusions of this dissertation are summarized and possible related future research is indicated.

CHAPTER II

DYNAMIC HOLOGRAM THEORY

2.1 Perspective

The static diffraction characteristics of a thick grating have been analyzed by Burckhardt[19] by solving the exact electromagnetic boundary-value problem and by Kogelnik[7] by employing a coupled-wave theory. In these theories, the thick grating is assumed to exist already (as opposed to analyzing the recording process); it is assumed to be uniform through the thickness of the material; and it is assumed to be unaffected by the reconstruction process. These theories have been applied successfully to a large number of experimental situations. There remain, however, numerous types of experimentally observed behavior that are not predicted with these static theories. These include certain writing effects, reading effects, and angular selectivity effects (to be discussed in this thesis).

It has been recognized[20] that the volume nature of thick holograms permits the interference of an incident light beam with its own diffracted beam inside the recording medium. This effect causes the continous recording of a new grating that may add to or subtract from the initial grating producing a resultant grating that is not uniform through the thickness of the material. As is shown in this work, the explanation of the resulting characteristics, in general, requires a dynamical theory such as that developed by Ninomiya.[21]

Among the materials used for recording volume holograms are those that exhibit light-induced refractive index changes (photorefractive materials), those that exhibit light-induced changes in optical absorption (photochromic materials), and those that exhibit both of these effects. Numerous recording materials exist in each of these categories.[18]

2.2 Analytical Techniques

The coupled-wave theory used here originated in acoustics.[22] This method has since been adapted to the analysis of volume holograms. Kogelnik[7] analyzed diffraction from sinusoidal hologram gratings and Su and Gaylord[23] analyzed nonsinusoidal gratings. These authors assumed the existence of a uniform grating through the thickness of the medium. Further, they assumed that the hologram grating can be addressed with a light beam without affecting the grating. Thus, these approaches are essentially static.

A more general approach, combining and extending the initial efforts of Kogelnik[7] and Kermisch,[24] has been presented by Ninomiya.[21] He included in the basic coupled-wave formalism, the dynamic behavior of holograms during recording and reading. That is, during recording, the development of the hologram continuously affects the diffraction process (feedback). Similarly, during reading, the incident beam is diffracted inside the medium and the resultant two beams interfere with each other, producing changes that may either add to or subtract from the existing holographic grating.

There has been little study of the characteristics of hologram gratings that are not uniform in the direction perpendicular to the

hologram surface. Kermisch[25] and Uchida[26] have theoretically analyzed the case of an exponentially attenuated grating, the latter using the coupled-wave approach. In the present work, nonuniformity is shown to occur for photorefractive materials as a result of the spatial phase difference (represented by ϕ_n) between the hologram-forming light interference pattern and the resulting index of refraction grating. Also, of course, an attenuated profile is produced if α_o, the average absorption coefficient of the material, is nonzero. It is found that the index profiles can have many forms in addition to exponential. The above theories[7,21,23-26] have been presented without experimental results.

In this work, the dynamic coupled-wave equations have been generalized to allow deviations in the angle of incidence and the wavelength, and are given for the E-mode polarization which corresponds to the laboratory arrangement used here. These are then used to calculate the grating profiles and the writing, reading, and angular selectivity characteristics of unslanted, phase volume holograms. Numerous types of experimental behavior cited in the literature as well as new experimental results presented here are shown to be predicted by the dynamic theory. The theory presented can also be made applicable to the H-mode case simply by setting the scalar product $\hat{r}\cdot\hat{s}$ equal to one.

2.3 Model and Dynamic Theory

2.3.1 Model

The thick hologram gratings treated here are assumed to be recorded by the intersection of two coherent light-waves in a thick (relative to the grating period) photosensitive medium. They are read

by a single wave incident upon the hologram. The recording and reading configurations are shown in Fig. 1. The signal and reference waves, represented by the vectors $\overline{S}$ and $\overline{R}$, respectively, are taken to be infinite plane waves. They are polarized in the plane of incidence of the grating (E-mode) with polarization vectors $\hat{s}$ and $\hat{r}$. The medium is unbounded in the x and y directions. It is to be noted that, during recording, the waves are symmetric in their angle of incidence and, therefore, the grating fringes are normal (unslanted) to the material surface. The extension to slanted gratings is straightforward. For convenience, it is assumed that the same average refractive index exists inside and outside the grating, (this is a common simplification, see e.g. Ref. 7) and thus no reflections or deviations occur.

2.3.2 Material Response

It is of fundamental importance in any theoretical description of volume hologram characteristics to assess properly the response of the material under study to the electromagnetic fields that produce the useful hologram-constituting changes in the physical parameters of the medium. The rates of change of the refractive index and absorption coefficient with exposure can be expressed, respectively, as

$$\frac{dn}{d\mathcal{E}} = a(\mathcal{E}) \tag{1}$$

and

$$\frac{d\alpha}{d\mathcal{E}} = b(\mathcal{E}), \tag{2}$$

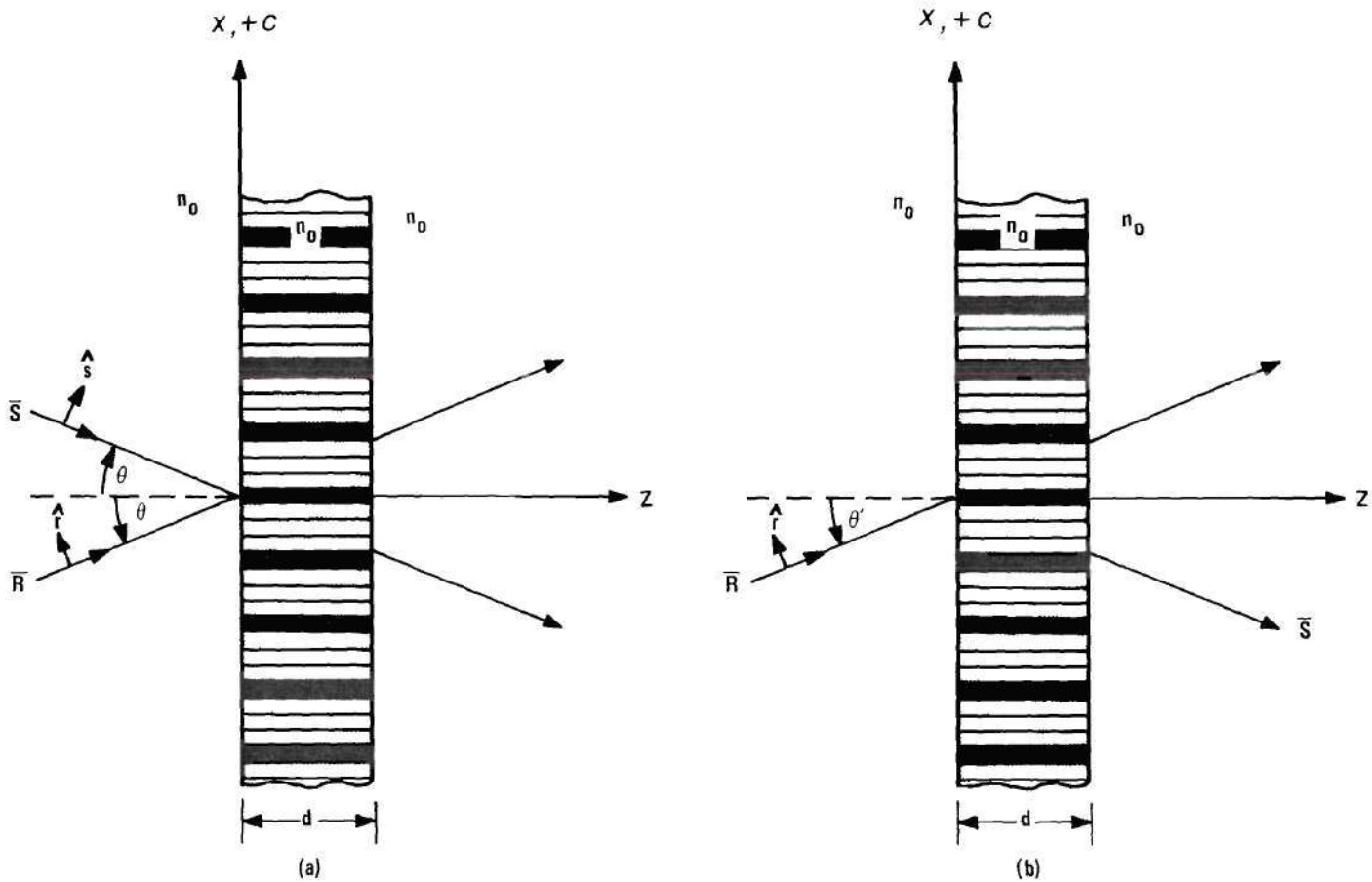

Figure 1. Model for (a) Hologram Recording, and (b) Hologram Reading. It is Found by (Reading) Experiments that the Crystal +c Axis Must Point in the +x Direction in Order to Obtain Experimentally and Theoretically Consistent Results in the (Anisotropic) $LiNbO_3$ Crystals Used in this Work.

where $\mathcal{E} \triangleq \int_0^T \bar{E} \cdot \bar{E}^* dt$ is the exposure, $\bar{E}$ is the total rms complex electric field in the medium, $\bar{E}^*$ is its complex conjugate, and T is the exposure time. The exposure sensitivity for the refractive index changes is $a(\mathcal{E})$ and the exposure sensitivity for absorption changes is $b(\mathcal{E})$. Equation (1) can be rewritten as

$$\frac{dn}{dt} = \frac{dn}{d\mathcal{E}} \frac{d\mathcal{E}}{dt} = a(\mathcal{E}) \frac{d\mathcal{E}}{dt} = a(\mathcal{E})\bar{E} \cdot \bar{E}^*. \tag{3}$$

Similarly,

$$\frac{d\alpha}{dt} = b(\mathcal{E})\bar{E} \cdot \bar{E}^*. \tag{4}$$

Hence, the net changes induced during the time T are

$$\Delta n \triangleq n(t=T) - n(t=0) = \int_0^T a(\mathcal{E})\bar{E} \cdot \bar{E}^* dt \tag{5}$$

and

$$\Delta\alpha \triangleq \alpha(t=T) - \alpha(t=0) = \int_0^T b(\mathcal{E})\bar{E} \cdot \bar{E}^* dt. \tag{6}$$

In general, the exposure sensitivities are functions of both time and position because $\mathcal{E}$ is. Calculation of the grating form with the forthcoming dynamic theory yields nonsinusoidal gratings in this case. If the dependence of the sensitivities on the spatial coordinates is neglected, that is, a slow spatial variation is assumed, it can be shown

that a sinusoidal grating (in x for a given z and T) results. For sensitivities that are constant in time and space, sinusoidal gratings are also produced.

The full functions $a(\mathcal{E})$ and $b(\mathcal{E})$ are not known in detail. It is possible, however, to estimate the time-behavior of $a(\mathcal{E})$, at least for writing, as discussed in a later section. In this work, $a(\mathcal{E})$ is approximated with a constant, a. (Phase holograms are emphasized.) It is shown here that even with a constant exposure sensitivity, good qualitative agreement between theory and experiment is obtained for photorefractive ferroelectrics such as lithium niobate. As mentioned above, this assumption means that the holographic grating is sinusoidal in x, (see Fig. 1). Experimental evidence exists[27] that in $LiNbO_3$ the gratings are, indeed, approximately sinusoidal in many cases.

2.3.3 Equations

Ninomiya[21] developed the dynamic coupled-wave equations that describe the recording and readout of thick holograms for exact Bragg conditions and H-mode polarization $(\hat{s}||\hat{r})$. Here the dynamic equations for E-mode polarization (electric field in the plane of incidence) are used because the available experimental data are primarily for the E-mode configuration. In addition, the equations have been generalized to permit deviations in the incident angle from the writing angle and deviations in the wavelength from the writing wavelength. The notation used here is that of Ninomiya.[21]

Following Ninomiya's development, the wave equation for the total electric field

$$\nabla^2\bar{E} - \nabla(\nabla \cdot \bar{E}) + K^2\bar{E} = \bar{0} \tag{7}$$

where K is the propagation constant, is used as a starting point. The total electric field in the grating is assumed to be expressed by the vector

$$\bar{E}(\bar{r},t) = \bar{R}(\bar{r},t)e^{-j\bar{\rho}\cdot\bar{r}} + \bar{S}(\bar{r},t)e^{-j\bar{\sigma}\cdot\bar{r}}, \tag{8}$$

where $\bar{\rho}$ and $\bar{\sigma}$ are the wave vectors of the reference and signal beams respectively and $\bar{r} = (x,y,z)$. The exposure is $\int_o^T \bar{E} \cdot \bar{E}^* dt$ where t is time and T is exposure time. As shown in Appendix A, combining Eqs. (5), (6), (7), and (8) and an appropriate expression for K leads to the following coupled equations for the complex wave amplitudes R and S (functions of z and t)

$$\cos\theta \frac{\partial R}{\partial z} + \gamma R = -j\Gamma_1 S(\hat{r}\cdot\hat{s})^2, \tag{9}$$

$$\cos\theta \frac{\partial S}{\partial z} + (\gamma + j\vartheta)S = -j\Gamma_2 R(\hat{r}\cdot\hat{s})^2, \tag{10}$$

where

$$\gamma = (j\frac{2\pi a}{\lambda} + b)\int_o^T (RR^* + SS^*)dt + \alpha_o, \tag{11}$$

$$\Gamma_1 = (\frac{2\pi a}{\lambda} e^{j\phi_n} - jbe^{j\phi_\alpha})\int_o^T RS^* dt, \tag{12}$$

$$\Gamma_2 = (\frac{2\pi a}{\lambda} e^{-j\phi_n} - jbe^{-j\phi_\alpha})\int_o^T SR^* dt, \tag{13}$$

$$\vartheta = (\beta_o'^2 - \sigma'^2)/2\beta'_o, \tag{14}$$

$$\beta_o = 2\pi n_o/\lambda, \tag{15}$$

$$\hat{r}\cdot\hat{s} = \cos 2\theta, \tag{16}$$

and λ is the free space wavelength, n_o is the average index of refraction, α_o is the average absorption constant, ϕ_n and ϕ_α are the phase differences between the hologram-forming light interference pattern and the resulting refractive index and absorption gratings, respectively, and a and b are the exposure sensitivities (constants) of the refractive index changes and absorption changes, respectively. The quantity ϑ is the dephasing factor introduced by Kogelnik.[7] As shown in Appendix C, the magnitude of the propagation vector of the diffracted wave upon reading is

$$\sigma' = (\beta_o'^2 - 4\beta_o\beta'_o \sin\theta \sin\theta' + 4\beta_o^2 \sin^2\theta)^{\frac{1}{2}}, \tag{17}$$

where $\beta'_o = 2\pi n'_o/\lambda'$. The primed quantities represent the values associated with the reading process.

Equations (9) and (10) can be solved numerically on a digital computer. It is shown in this dissertation that the solutions thus obtained describe the various types of externally measurable diffraction behavior of volume holograms that have been experimentally measured and reported in the literature (sometimes with very little explanation).

2.4 Internal Grating Profiles

The solutions of the dynamic coupled-wave equations, the complex wave amplitudes R(z,t) and S(z,t), can be used to calculate the terminal characteristics (i.e. z=d) of volume holographic gratings as well as certain internal distributions ($0 \le z \le d$) that are not easily accessible by direct measurement. Because of the generality of the dynamic theory, no arbitrary conditions (such as grating uniformity[7,19]) on the variations with thickness of the hologram-constituting material changes are imposed. It is the purpose of this section to discuss the thickness variations of the refractive index modulation in volume phase hologram gratings as derived from the dynamic theory.

In the present context, it is assumed that the change in the refractive index, n, is related to the exposure, $\mathcal{E}$, by Eq. (1) with $a(\mathcal{E}) = a = \text{constant}$. For the recording geometry used in this work (see Fig. 1), the hologram-constituting refractive index variation is then given by (see Eq. (A7) in Appendix A)

$$n_1(x,z,T) = 2a\cos 2\theta \int_o^T |RS^*| \cos\{(\bar{\sigma} - \bar{\rho})\cdot\bar{r} + \xi + \phi_n\}dt, \tag{18}$$

where $(\bar{\sigma} - \bar{\rho})\cdot\bar{r} = -2\beta_o \sin\theta\, x \triangleq kx$ and $\cos\xi = \mathrm{Re}\{RS^*\}/|RS^*|$. This can be rewritten as

$$n_1(x,z,T) = 2a\cos 2\theta\, (M^2+N^2)^{1/2} \cos\{kx+\phi_n+\cos^{-1}[M/(M^2+N^2)^{1/2}]\}, \tag{19}$$

where $M=M(z,T) \triangleq \int_o^T \mathrm{Re}\{RS^*\}dt$, $N=N(z,T) \triangleq \int_o^T \mathrm{Im}\{RS^*\}dt$, and ϕ_n is the

spatial phase difference ($0° \leq \phi_n \leq 90°$) between the grating-forming light intensity pattern and the resulting refractive index pattern as previously defined. Thus, if the wave amplitudes R and S are known, the index modulation can be calculated by Eq. (19). It is noted that the grating is sinusoidal in x (symmetrical recording wave incidence) but with amplitude and phase dependent on the exposure time, T, and the thickness coordinate, z. The amplitude of the index modulation along a peak in the pattern, n_{1p}, is consequently

$$n_{1p}(z,T) = 2a \cos 2\theta \ (M^2+N^2)^{\frac{1}{2}}. \tag{20}$$

It is informative to calculate also the grating z-profile at a selected value of x. For this, $kx+\phi_n=0$ is chosen. Then, the index change at this particular x-cut is

$$n_{1c}(z,T) = 2a \cos 2\theta \, M. \tag{21}$$

This is a good choice for x since, for the boundary conditions $R(0,t)=R_o$ and $S(0,t)=S_o$ with R_o and S_o purely real, N=0 and, hence, $n_{1p}=n_{1c}$ at z=0 which is desirable for comparison.

The quantity $\cos^{-1}[M/(M^2+N^2)^{\frac{1}{2}}]$ is a measure of grating bending; that is, the deviation of a grating peak at an arbitrary value of z from its position at z=0. Note that if N=0, this quantity is zero and the grating does not bend. The grating bending can be related to the phases of the two waves that are present in the grating. Writing $R(z,t) = |R|\exp(j\phi_r)$ and $S(z,t) = |S|\exp(j\phi_s)$, then, from the definition of N,

$$N = \int_o^T |RS| \sin(\phi_r - \phi_s) dt. \tag{22}$$

Assuming that $|RS| \neq 0$, it is required that $\phi_r - \phi_s = 0$ for N=0. If $\phi_r - \phi_s \neq 0$, then $N \neq 0$ since $|RS| \neq 0$. Grating bending is, therefore, a direct result of the z-dependent phase difference between the two waves in the grating at any given time.

It may be of interest to follow the time-development of the index amplitude averaged over the material thickness during recording. Accordingly, the average index change along a grating peak is calculated from

$$n_{lpa}(T) = d^{-1} \int_o^d n_{lp}(z,T) dz \tag{23}$$

An analogous expression is used to calculate the average index change for the x-cut selected above.

2.5 Time Dependent Exposure Sensitivity

As will be discussed later in this thesis, it is possible that the exposure sensitivities for the photoinduced changes in the refractive index and absorption coefficient of the material are functions of time. In this case, Eqs. (9) and (10) still hold but the coefficients γ, Γ_1, and Γ_2 must be modified. It is easy to show that for time dependent sensitivities, a(t) and b(t), these coefficients must be written as

$$\gamma = \int_o^T \{ j \frac{2\pi}{\lambda} a(t) + b(t) \} [RR^* + SS^*] dt + \alpha_o, \tag{24}$$

$$\Gamma_1 = \int_o^T [\frac{2\pi}{\lambda} e^{j\phi_n} a(t) - j e^{j\phi_\alpha} b(t)] RS^* dt, \tag{25}$$

and

$$\Gamma_2 = \int_o^T [\frac{2\pi}{\lambda} e^{-j\phi_n} a(t) - je^{-j\phi_\alpha} b(t)] SR^* dt. \quad (26)$$

It can also be shown that the expression for the refractive index variation responsible for the holographic diffraction (see Eq. (19)) is, for time-varying exposure sensitivity,

$$n_1(x,z,T) = 2\cos 2\theta (M'^2+N'^2)^{\frac{1}{2}} \cos\{kx+\phi_n+\cos^{-1}[M'/(M'^2+N'^2)^{\frac{1}{2}}]\} \quad (27)$$

where

$$M' = M'(z,T) \triangleq \int_o^T a(t)\,\mathrm{Re}\{RS^*\}dt$$

and

$$N' = N'(z,T) \triangleq \int_o^T a(t)\,\mathrm{Im}\{RS^*\}dt.$$

CHAPTER III

CALCULATED RESULTS AND EXPERIMENTAL BEHAVIOR

3.1 Calculational Procedure

In this chapter, numerical results obtained by solving Eqs. (9) and (10) are presented for selected sets of hologram parameters. The solutions are seen to compare favorably with published experimental results. For writing, the equations are solved with $\vartheta = 0$ (no dephasing) and the boundary conditions $R(0,t) = R_o$ and $S(0,t) = S_o$. For reading, ϑ can be nonzero. Deviations in wavelength and/or incident angle from the corresponding writing quantities result in $\vartheta \neq 0$. The boundary conditions $R(0,t) = R_o'$ and $S(0,t) = 0$ are used for the case of readout with the R beam and $R(0,t) = 0$ and $S(0,t) = S_o'$ are used for readout with the S beam. Diffraction efficiency is then defined as $\eta = S(1,T)S^*(1,T)/R_o'^2$ for R beam readout and $\eta = R(1,T)R^*(1,T)/S_o'^2$ for S beam readout (the equations are normalized with respect to the thickness so that $0 \leq z \leq 1$).

The computer algorithm (see Appendix E) employs a fourth order Runge-Kutta method to solve the equations with respect to the z variable. The integrations in t were performed by replacing the integrals by the corresponding sums and using increments, Δt, small enough for convergence. The actual incremental step sizes used were $\Delta z = 0.01$ and $\Delta t = 0.5$ sec. The numerical accuracy was tested by decreasing the step sizes Δz and Δt until the improvements in convergence were insignificant.

The calculations presented are for a 1.66 mm and a 2.00 mm thick

crystal of $LiNbO_3$ with its optic axis (c-axis) in the plane of incidence of the writing beams. The writing and reading waves are polarized in the plane of incidence and have a wavelength of $\lambda = 0.5145$ μm. The angles of incidence for the writing beams are $\pm 2.23°$ (corresponding to external angles of incidence of $\pm 5.00°$ for a grating surrounded by a unity refractive index medium). For this wavelength, polarization, angle of incidence, and orientation of the lithium niobate crystal, the index of refraction is $n_o = 2.2426$. For writing $R_o = S_o = 1000$ volt/m. Reading is done with $R_o' = 1000$ volt/m. Only transmission phase holograms are considered, that is, b is set equal to zero (no photochromic effect).

3.2 Writing

With a few exceptions, the experimental diffraction efficiency writing characteristics (η vs. t) reported in the literature for volume holograms begin with zero initial slope and increase in a parabolic fashion. The magnitudes of the diffraction efficiencies reported, however, vary considerably. Several workers[28-31] report relatively low efficiencies (e.g. < 1%) exhibiting saturating behavior or a very low rate of increase. Others[32-37] have reported higher efficiencies, also showing saturation behavior. At times, instead of saturation, an oscillatory diffraction efficiency is observed.[8,33,34,36,37] It seems that experimental oscillatory writing characteristics are observed primarily for relatively high efficiency holograms. In many papers,[8,20,30,33,38-44] the writing is terminated before the onset of oscillation or saturation.

The types of behavior indicated above can be straightforwardly

predicted using the dynamic theory. The oscillatory behavior is seen to be inherent in the theory because of the assumption of constant refractive index exposure sensitivity, a. The material is thus assumed to respond continuously to the interaction of the wave fields at all times. Physically, the quantity a may be time dependent since the physical mechanisms (such as photochemical effects, drift of charge carriers, diffusion of charge carriers, etc.) that produce the sensitivity may be self-limiting in some materials. Therefore, saturation at low or high efficiency may be brought about by a vanishing sensitivity. At the turning point toward saturation, $|\frac{d\eta}{dt}|$ is strongly affected by $|\frac{da}{dt}|$. Thus, depending on the material and the experimental situation, gradual[28,30-34,36,37] or abrupt[29,35] turning points are observed in $\eta(t)$. Figure 2 demonstrates that an approximately saturating behavior may be predicted by the dynamic equations even with a constant refractive index exposure sensitivity. Figures 3 and 4 show similar behavior that has been experimentally obtained and reported in the literature. Figure 5 exhibits oscillatory behavior similar to that experimentally observed by the writer in lithium niobate and shown in Fig. 6. Note the decreasing amplitude and increasing period of the diffraction oscillations with exposure in both of these figures. Figure 5 also bears qualitative resemblance to the experimental characteristics of Figs. 7 and 8(a). Figure 9 illustrates large, increasing diffraction efficiency oscillations with minima near 0%. This behavior is like that depicted in Fig. 10 for a 1.8 mm thick photopolymer hologram grating.

The exceptional cases for which writing starts with an apparently linear $\eta(t)$ characteristic[29,31,34,45] (rather than parabolic) may

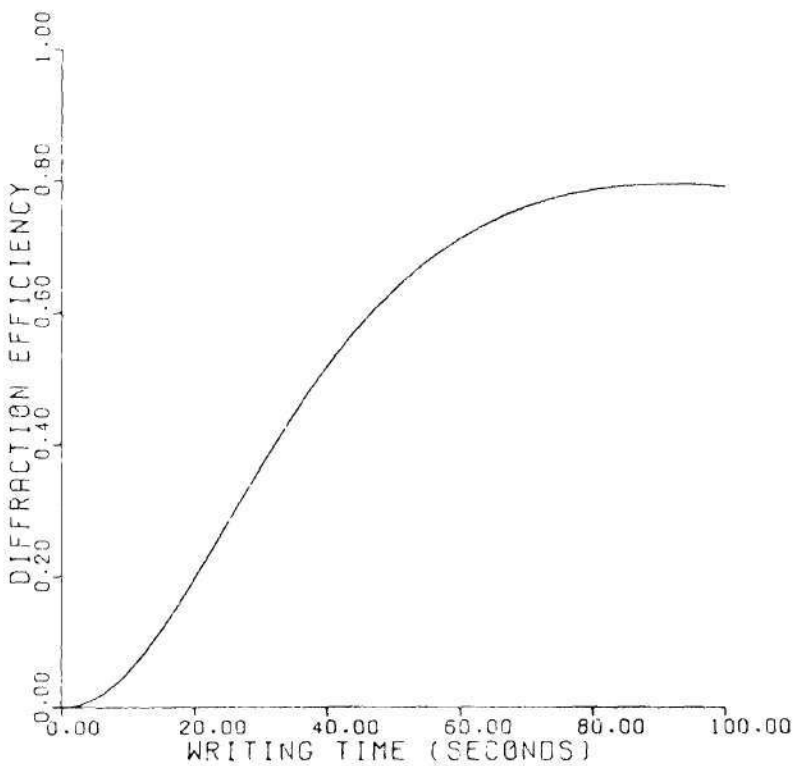

Figure 2. Calculated Hologram Writing Characteristic Exhibiting a Saturation-Like Appearance. Hologram Thickness is 2.00 mm, $a = 10^{-12}$ $(volt/m)^{-2}sec^{-1}$, $\phi_n = 90°$, $\alpha_o = 0$, and Other Parameters as Given in Sec. 3.1.

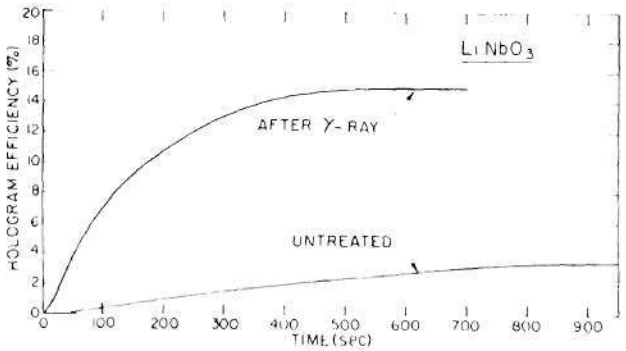

Figure 3. Experimental Saturation-Like Hologram Writing Characteristic in Lithium Niobate. Sample Thickness is 3 mm, λ = 0.488 μm, and the Power Density is 6×10^{-3} W/mm^2 (after Ref. 33).

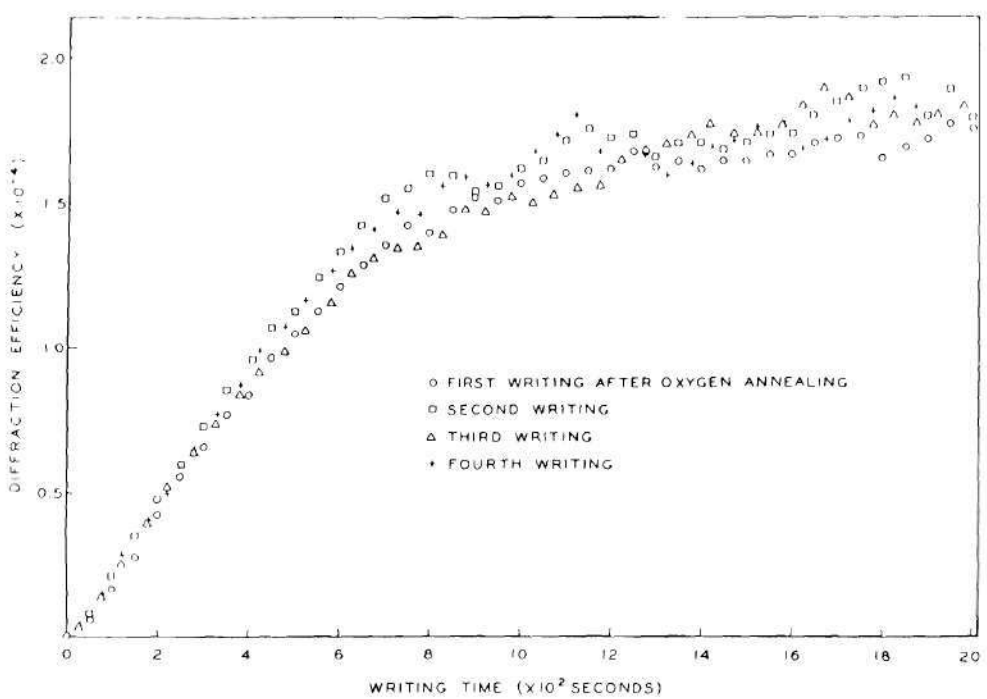

Figure 4. Experimental Saturation-Like Hologram Writing Characteristic in Lithium Niobate. Sample Thickness is 5 mm, λ = 0.5145 μm, and the Power Density is 1.09×10^{-2} W/mm^2 (after Ref. 28).

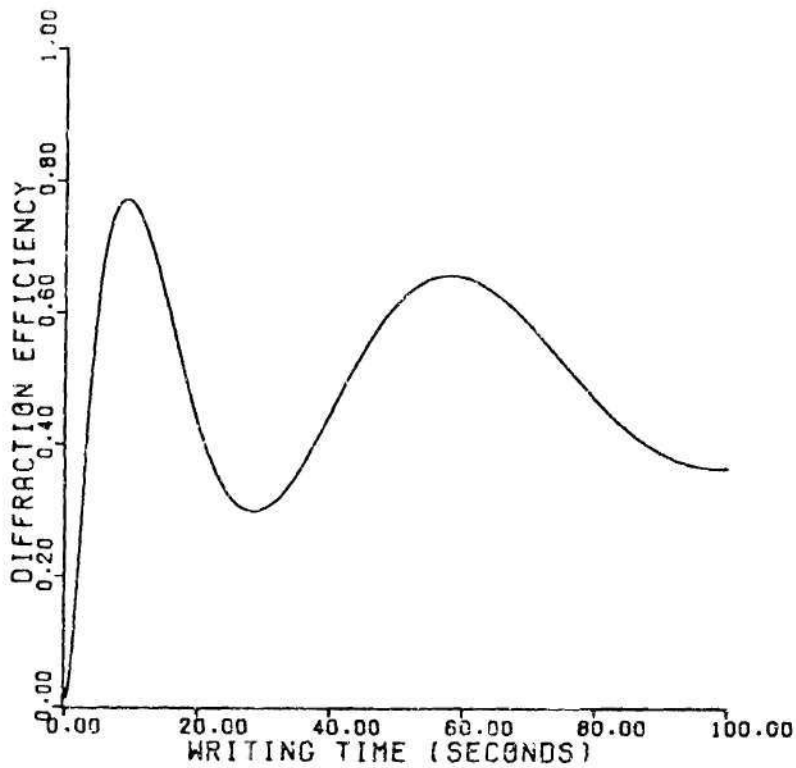

Figure 5. Calculated Oscillatory Hologram Writing Characteristic with Decreasing Amplitude and Increasing Period of the Diffraction Efficiency Oscillations. Hologram Thickness is 2.00 mm, $a = 10^{-11}$ $(volt/m)^{-2}sec^{-1}$, $\phi_n = 90°$, $\alpha_o = 0$, and Other Parameters as Given in Sec. 3.1.

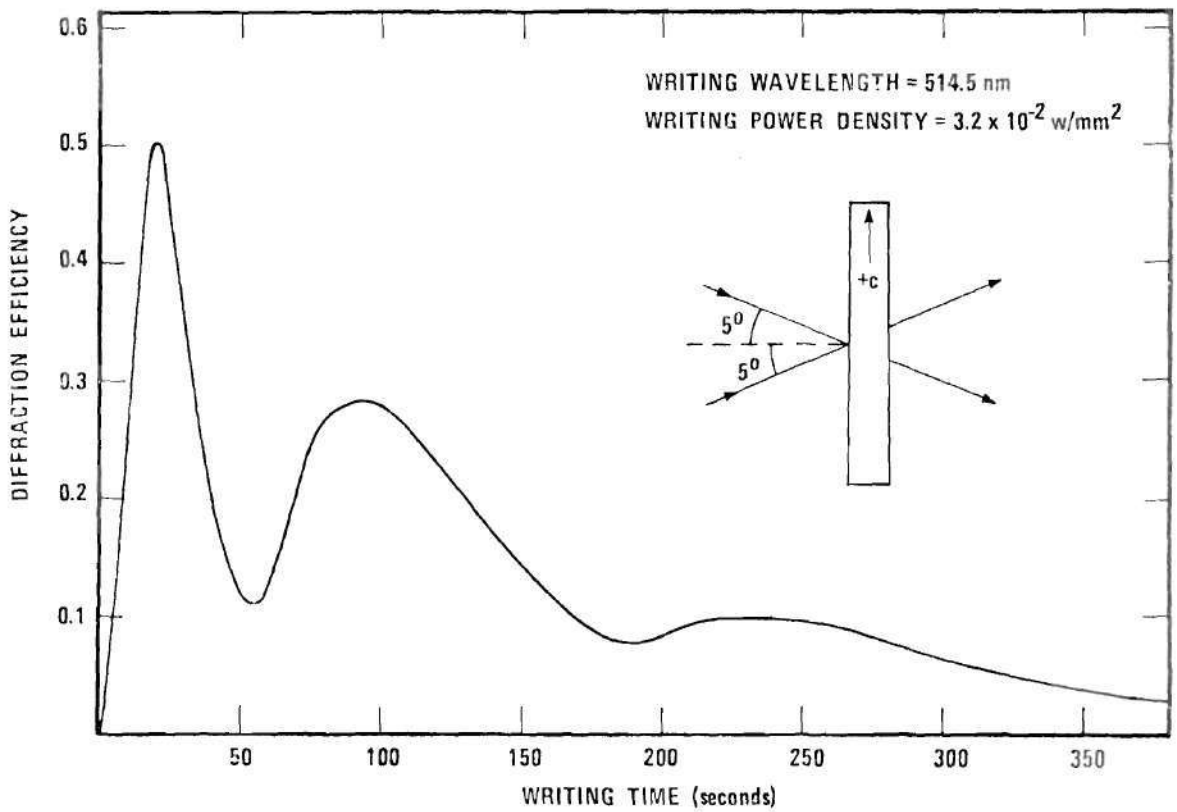

Figure 6. Experimental Oscillatory Hologram Writing Characteristic for a 1.66 mm Thick, Iron-Doped Lithium Niobate Crystal. Writing Beam Polarizations are in the Plane of Incidence and the Experimental Configuration is as Shown in the Figure Inset.

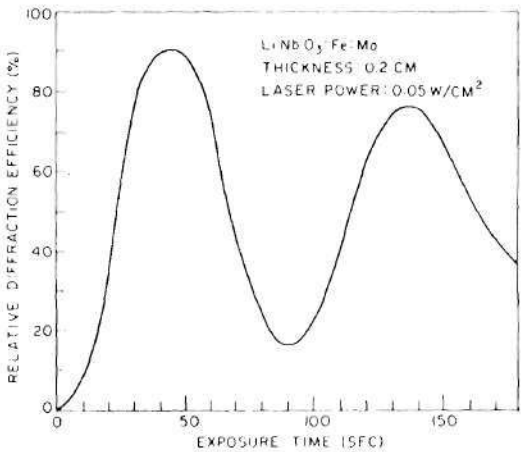

Figure 7. Experimental Oscillatory Hologram Writing Characteristic in Lithium Niobate. Hologram Thickness is 2 mm, λ = 0.488 μm, and the Power Density is 5×10^{-4} W/mm^2 (after Ref. 33).

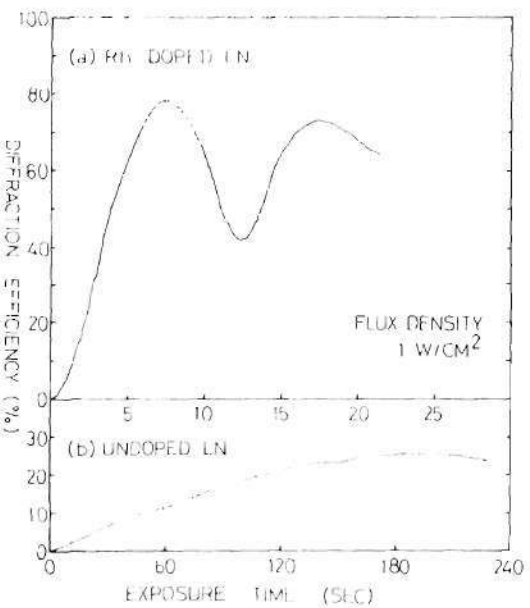

Figure 8. Experimental (a) Oscillatory and (b) Saturating Hologram Writing Characteristics in Lithium Niobate. Crystal Thickness is 2.5 mm, λ = 0.4880 μm, and the Power Density is 10^{-2} W/mm^2 (after Ref. 34).

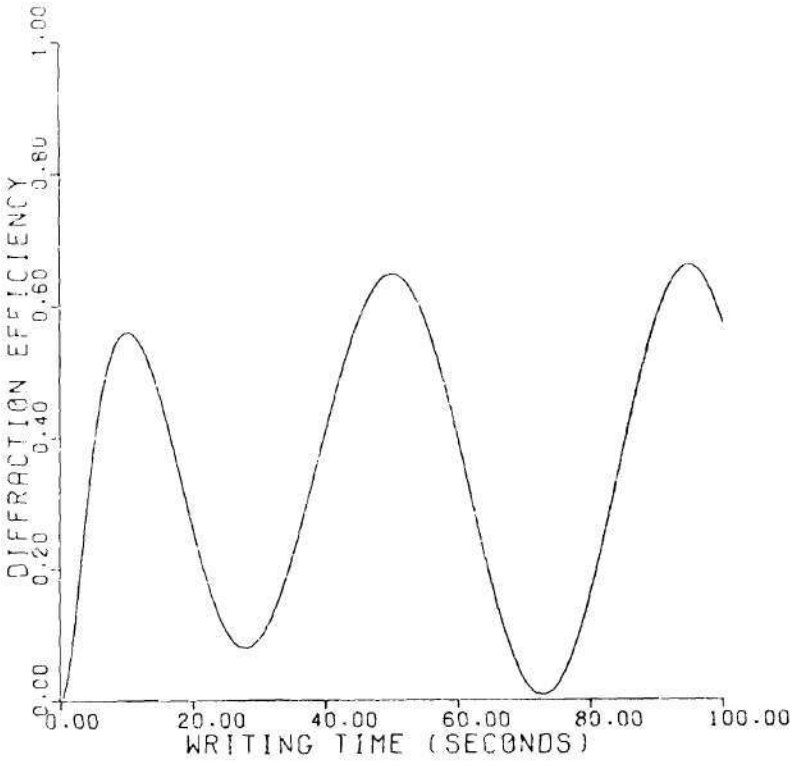

Figure 9. Calculated Oscillatory Hologram Writing Characteristic with Diffraction Efficiency Minima Near 0%. Hologram Thickness is 2.00 mm, $a = 10^{-11}$ $(volts/m)^{-2}sec^{-1}$, $\phi_n = 60°$, $\alpha_o = 10^2 m^{-1}$, and Other Parameters as Given in Sec. 3.1.

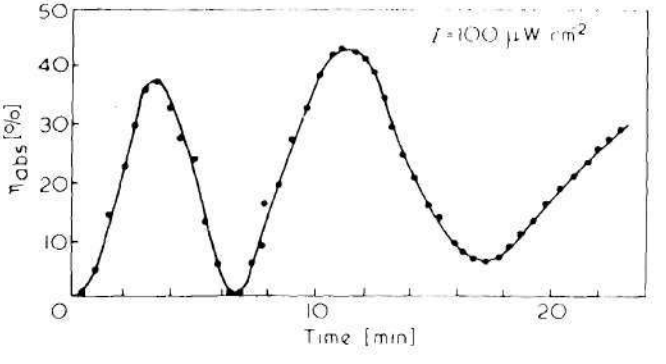

Figure 10. Experimental Oscillatory Hologram Writing Characteristic in a Photopolymer. Hologram Thickness is 1.8 mm and the Power Density is 10^{-6} W/mm (after Ref. 8).

possibly be reconciled by the fact that the zero-slope, initial portion of the $\eta(t)$ is sometimes of very brief duration (see, for example, Figs. 3, 4, and 6) and thus the curve appears to be approximately linear when in fact it may not be.

3.3 Readout

The application of a reading beam to a thick hologram may continually change its characteristics. Experimentally, the most commonly observed result seems to be exponential-like decay of the diffraction efficiency.[20,28-30,33,34,36,38-40,42,43,46,47] Oscillatory diffraction efficiency readout behavior has also been reported. In rhodium-doped $LiNbO_3$, for example, vivid oscillations have been observed during readout.[34] An iron-doped sample of $LiNbO_3$ has shown an initial rise and a subsequent decay of diffraction efficiency upon readout.[39] Oscillatory behavior at low efficiency following an exponential-like decay has also been noticed.[39] Self-enhancement (an increase of diffraction efficiency upon reading) of Fe-doped $LiNbO_3$ holograms has been observed.[48] In this case, erasure and enhancement were produced depending on which of the original writing beams was used for readout. Behavior such as this has been theoretically predicted by Staebler and Amodei.[20] Further experimental results are presented here for volume holograms that show this type and other effects upon changing the reading beam from the R beam to the S beam (see Fig. 1).

The various types of behavior discussed above are all predicted by the dynamic theory. In Fig. 11, for example, a calculated exponential-like decay of the hologram efficiency is shown. Note that, eventually,

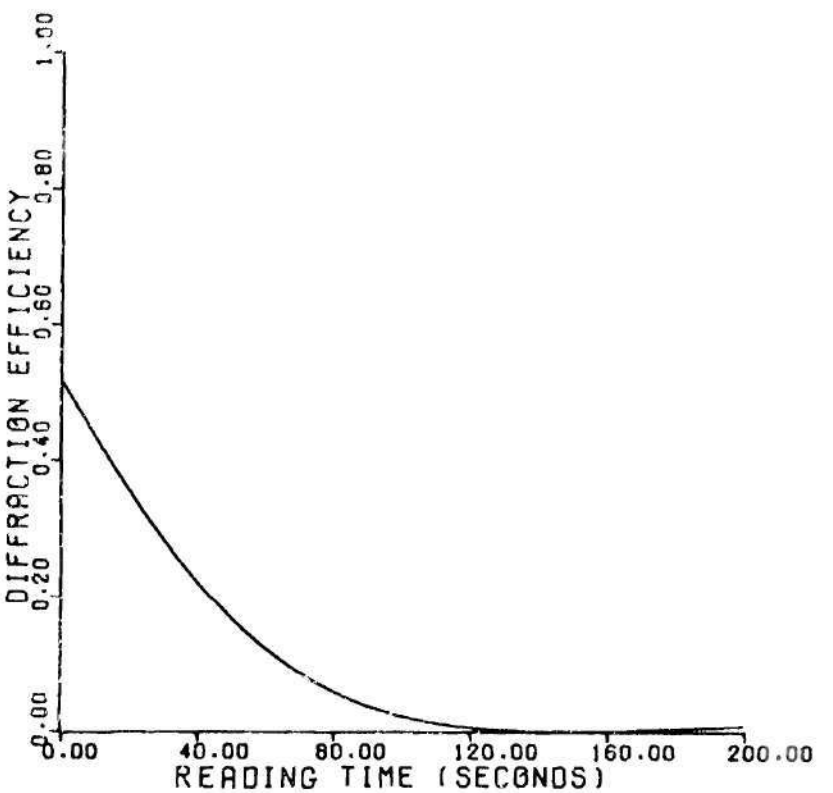

Figure 11. Calculated Exponential-Like Reading Characteristic. Note Slight Rise in Efficiency at a Reading Time of 200 Seconds. Hologram Thickness is 2.00 mm, $a = 10^{-12}$ $(volt/m)^{-2}sec^{-1}$, $\phi_n = 90°$, $\alpha_o = 0$, Readout with R beam, and Other Parameters as Given in Sec. 3.1. The Original Hologram was Recorded Using These Same Parameters and an Exposure Time of 40 Seconds.

the efficiency rises again (like experimentally reported in Ref. 39 and in Fig. 4 of Ref. 47). Figures 12(b) and 13 illustrate corresponding experimental results taken from the literature. Figure 14 depicts the experimentally recorded decay of the efficiency of a hologram written in a 1.66 mm thick, iron-doped crystal of $LiNbO_3$ for the beam configuration indicated in the inset of the figure as measured by the writer. Note the slight oscillations at low efficiency. Figure 15 illustrates the calculated effect of switching the reading beam to the symmetrical angular location. For R beam reading, an initial decrease in diffraction efficiency is predicted, whereas for S beam readout, an initial increase is predicted. Such effects have been reported in the literature as indicated in Figs. 16 and 17. In addition, in Fig. 21, an initial rise in the efficiency is observed. Figure 15 also clearly predicts oscillations at low efficiency such as have been experimentally observed. Figure 18 shows the behavior of efficiency oscillations followed by monotonic decay as calculated by the dynamic theory. This is qualitatively like the experimental readout behavior observed in rhodium-doped $LiNbO_3$ by Ishida et al.[34] and shown in Fig. 19. Figure 20 illustrates calculated diffraction efficiency oscillations that both decrease and increase as a function of readout exposure. In Fig. 21, experimentally measured oscillatory reading behavior is shown for the same hologram grating used in Fig. 14 except that reading is done with the beam at the symmetric recording angle (reading with the S beam instead of the R beam in the notation of Fig. 1). Large variations in both the amplitude and the period of the efficiency oscillations are observed. This behavior is qualitatively similar to the predicted readout diffraction efficiency of Fig. 20.

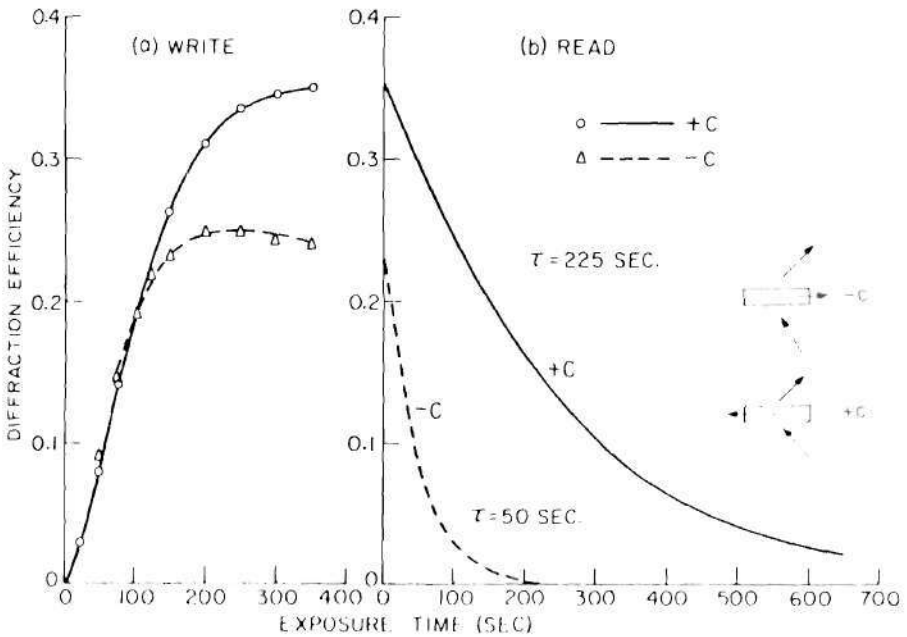

Figure 12. Experimental (a) Writing and (b) Reading Characteristics of Volume Holograms in Lithium Niobate. Crystal Thickness is 7 mm, λ = 0.488 μm, and the Power Density is 6×10^{-3} W/mm^2. The Reading Beam Orientation Relative to the Crystal C-Axis is Shown in the Inset (after Ref. 20).

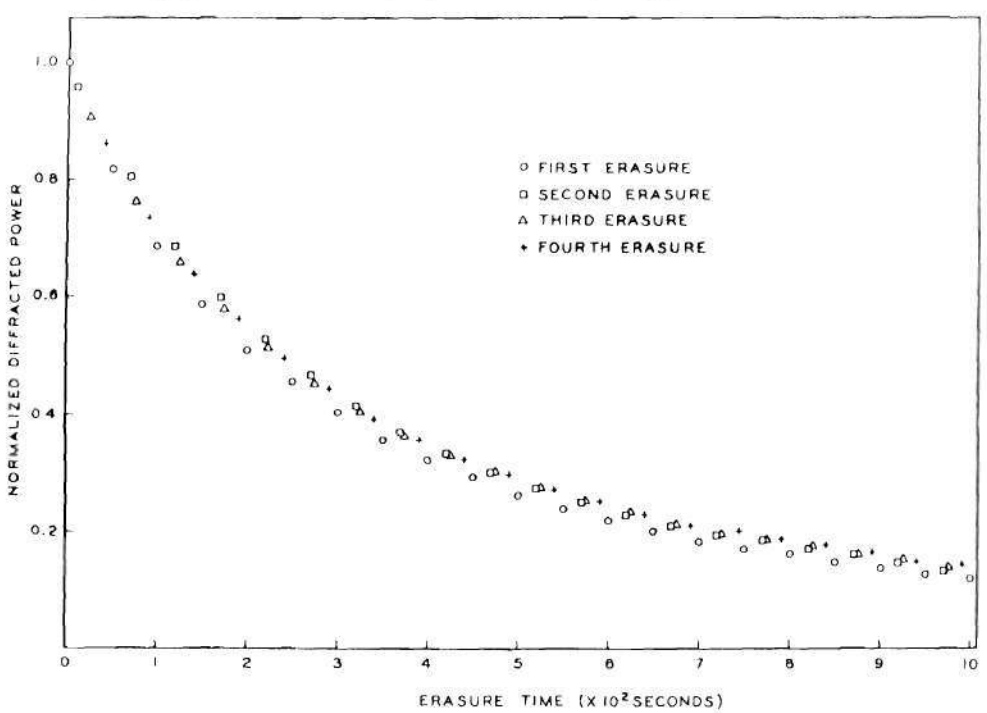

Figure 13. Experimental Exponential-Like Hologram Reading Characteristic in Lithium Niobate. Hologram Thickness is 5 mm, λ = 0.5145 μm, and the Power Density is 5.9×10^{-3} W/mm^2 (after Ref. 28).

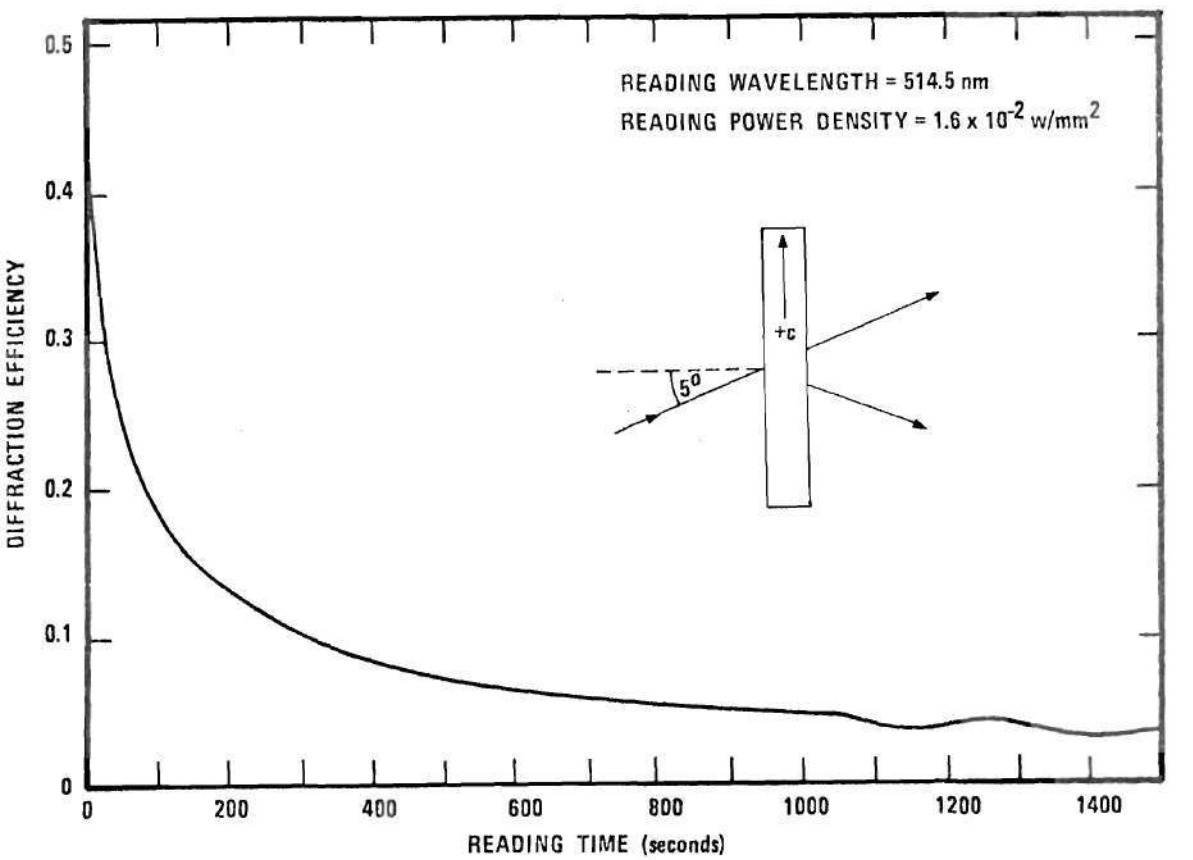

Figure 14. Experimental Exponential-Like Reading Characteristic for a 1.66 mm Thick, Iron-Doped Lithium Niobate Crystal. Small Amplitude Diffraction Efficiency Oscillations are Present at Low Efficiencies. Reading Beam Polarization is in the Plane of Incidence and the Experimental Configuration is as Shown in the Figure Inset.

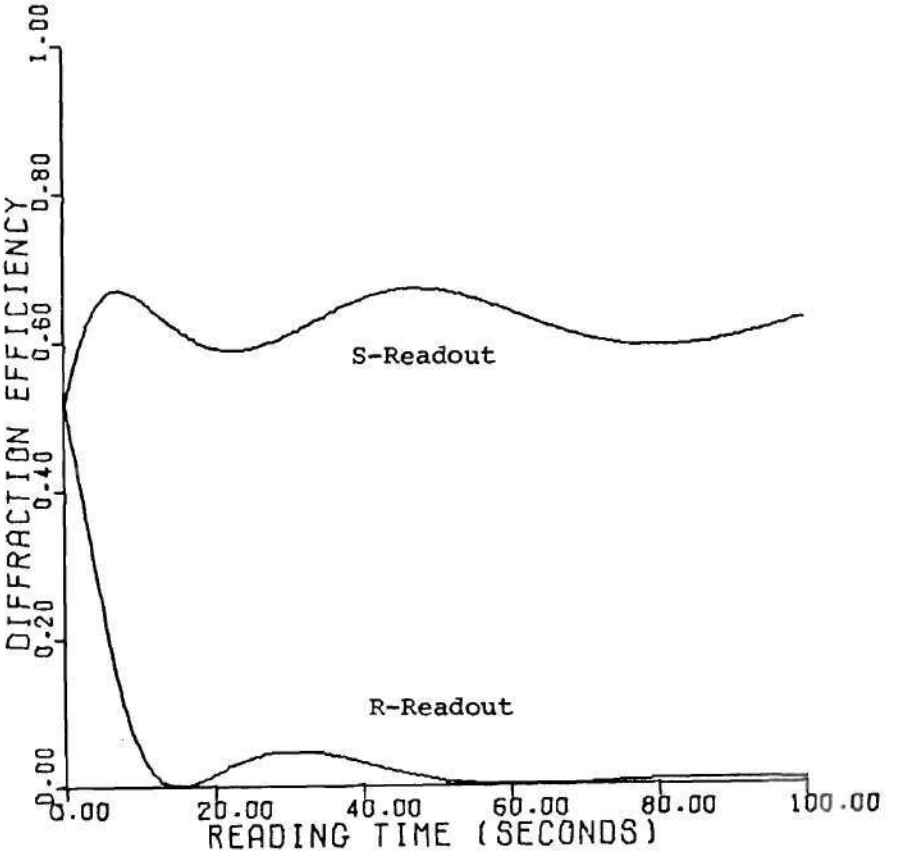

Figure 15. Calculated Reading Characteristics Illustrating the Effect of Reading Beam Interchange. For R-Beam Readout, Oscillations Occur at Low Diffraction Efficiencies After Erasure. For S-Beam Readout, the Oscillations Occur at High Efficiencies After Enhancement. Hologram Thickness is 2.00 mm, $a = 10^{-11}$ $(volt/m)^{-2}sec^{-1}$, $\phi_n = 90°$, $\alpha_o = 10^2 m^{-1}$, and Other Parameters as Given in Sec. 3.1. The Original Hologram was Recorded Using these Same Parameters and an Exposure Time of 10 Seconds.

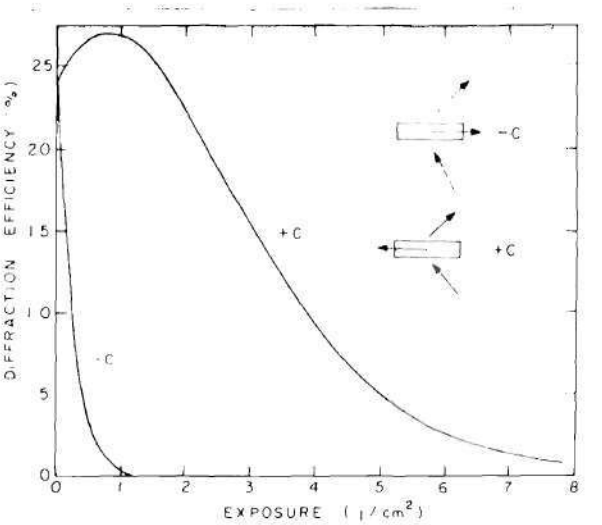

Figure 16. Experimentally Observed Effect of Changing the Reading Beam Direction Relative to the Crystal C-Axis on the Hologram Reading Characteristic. The $LiNbO_3$ Crystal is 9 mm Thick and λ = 0.488 μm (after Ref. 39).

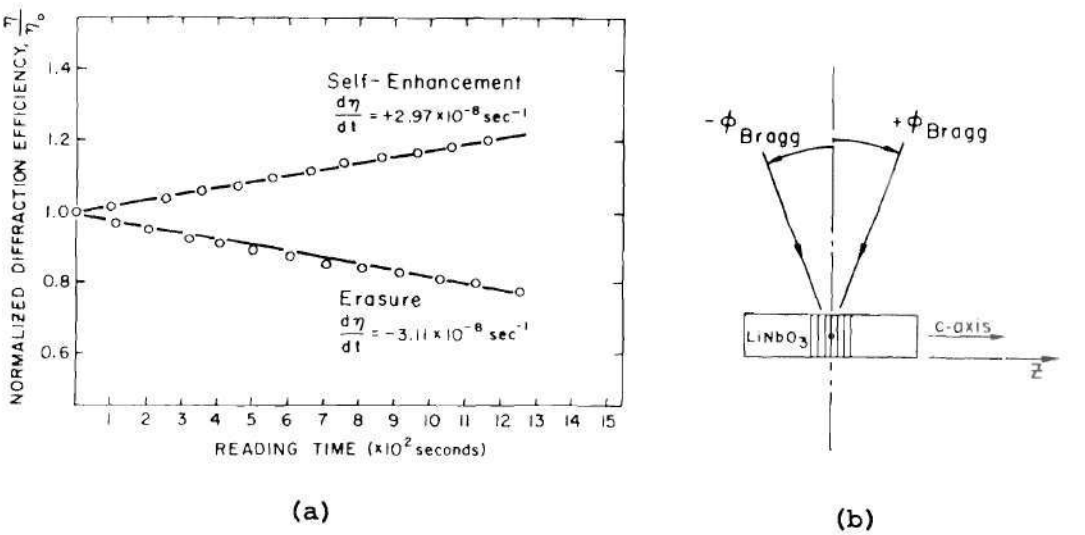

(a) (b)

Figure 17. Experimentally Observed Effect of Changing the Reading Beam Direction Relative to the Crystal C-Axis. (a) Hologram Reading Characteristics. (b) Experimental Configuration. The $LiNbO_3$ Crystal is 1 mm Thick, λ = 0.53 μm, and $\eta_o = 1.71 \times 10^{-4}$. Self-Enhancement Occurs for the Reading Beam at $-\phi_{Bragg}$. Erasure Occurs for the Beam at $+\phi_{Bragg}$ (after Ref. 48).

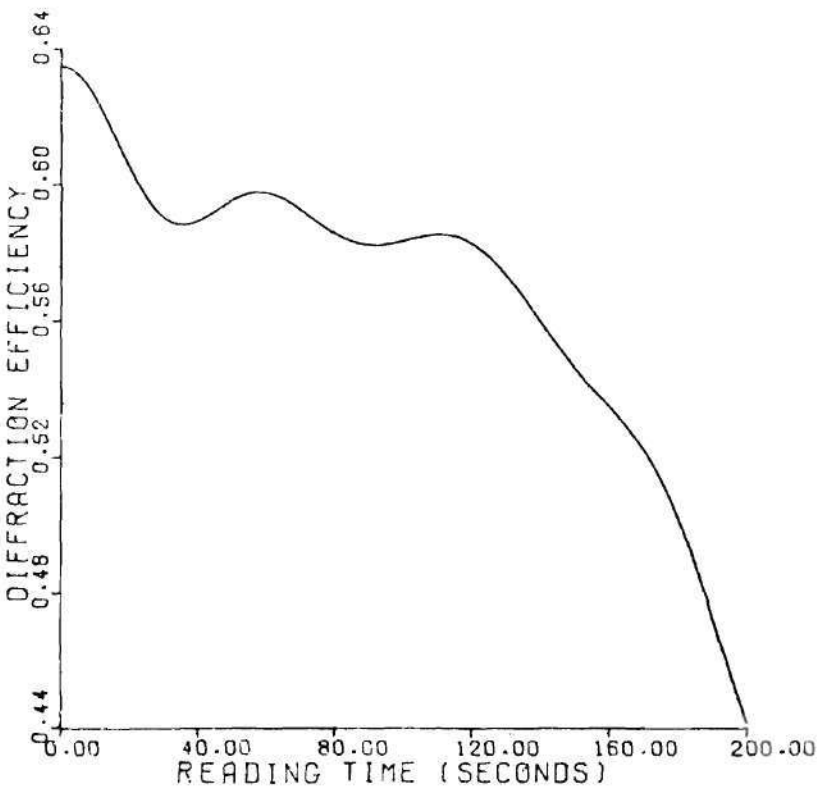

Figure 18. Calculated Reading Characteristic Showing Diffraction Efficiency Oscillations Followed by Rapid Decay. Hologram Thickness is 2.00 mm, $a = 10^{-11}$ $(volt/m)^{-2}sec^{-1}$, $\phi_n = 0°$, $\alpha_o = 0$, Readout with R beam, and Other Parameters as Given in Sec. 3.1. The Original Hologram was Recorded Using these Same Parameters and an Exposure Time of 35 Seconds.

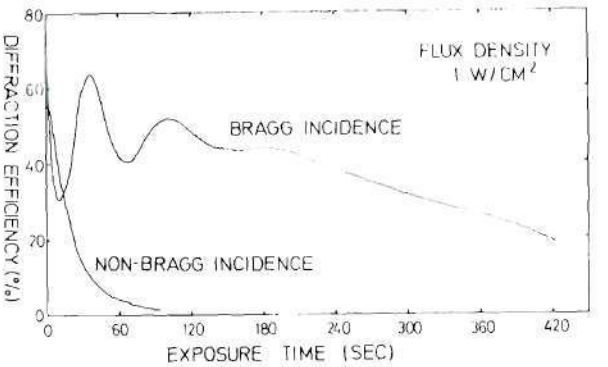

Figure 19. Experimental Hologram Reading Characteristic Exhibiting Initial Oscillations Followed by Monotonic Decay. The $LiNbO_3$ Sample is 2.5 mm Thick, λ = 0.488 μm, and the Power Density is 10^{-2} W/mm^2 (after Ref. 34).

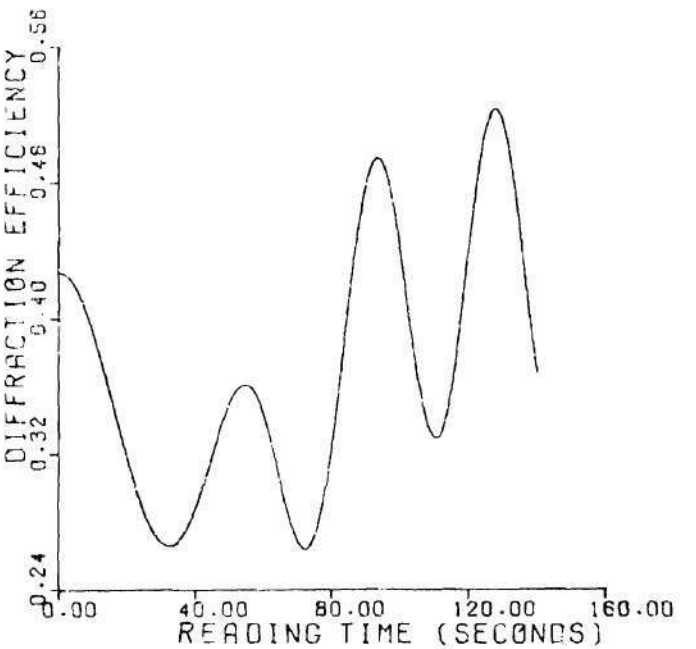

Figure 20. Calculated Oscillatory Reading Characteristic Showing Large Variations in the Amplitude and Period of the Diffraction Efficiency Oscillations. Hologram Thickness is 2.00 mm, a = 10^{-11} (volt/m)$^{-2}$ sec^{-1}, $\phi_n = 0°$, $\alpha_o = 0$, Readout with R beam, and Other Parameters as Given in Sec. 3.1. The Original Hologram was Recorded Using these Same Parameters and an Exposure Time of 10 Seconds.

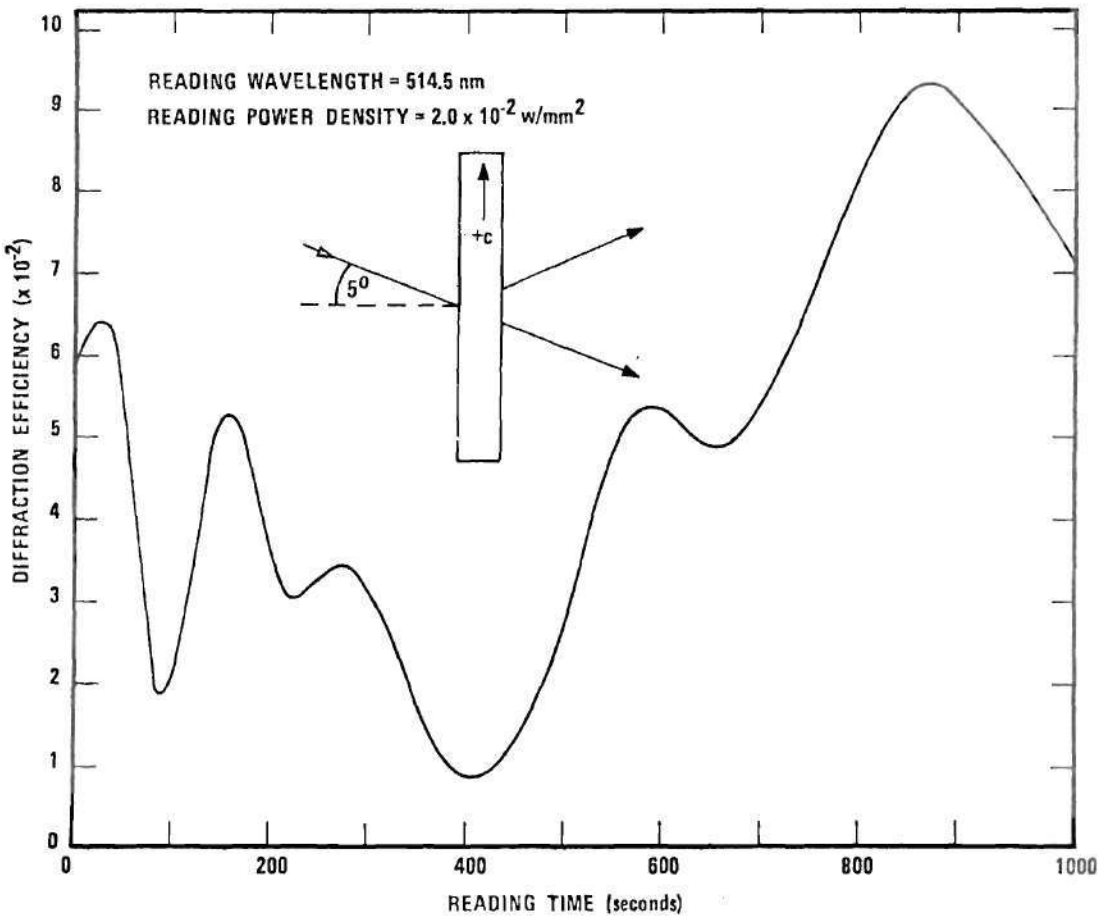

Figure 21. Experimental Oscillatory Reading Characteristic for a 1.66 mm Thick, Iron-Doped Lithium Niobate Crystal. A Wide Variation in the Amplitude and Period of the Diffraction Efficiency Oscillations is Apparent. Reading Beam Polarization is in the Plane of Incidence and the Experimental Configuration is as Shown in the Figure Inset.

3.4 Angular Selectivity

Angular selectivity refers to the variation of diffraction efficiency as a function of the angle of incidence of the reading wave. In experiments measuring this property of thick hologram gratings, a low power reading beam or a reading beam of a wavelength at which the material is insensitive is generally used so as not to affect the hologram by the process of measurement.

Experimental angular selectivity results are somewhat less plentiful than the other terminally measured characteristics of thick holograms. Some of the existing experimental results exhibit a series of nonzero minima in place of the nulls[49-53] predicted by static hologram theories. Some experimental data show no minima in the angular selectivity.[49,54] It is now well established[25,26,49] that nonuniformity of the grating with material thickness produces non-zero diffraction minima or causes the complete disappearance of the minima in the angular selectivity pattern.

The dynamic theory straightforwardly predicts the various types of angular selectivity behavior of volume holograms. Here, grating nonuniformity arises if $\phi_n \neq 0$, or $\alpha_o \neq 0$, or if both ϕ_n and α_o are nonzero. Nonuniformity, and the corresponding disappearance of angular selectivity minima for low loss materials ($\alpha_o \cong 0$), is explained by the dynamic theory but cannot be explained by the static theories. In Fig. 22 a logarithmic plot of experimental data is presented for a hologram written in a 1.66 mm thick, 0.05 mole-percent Fe-doped crystal of $LiNbO_3$ and compared to the solution of Eqs. (9) and (10) for the same conditions. Due to the short writing time and the low efficiency

($\lesssim$ 1%), the grating is still quite uniform through the thickness of the material (z direction) and thus the grating exhibits well defined nulls in the diffraction efficiency for a series of reading angles. Theory and experiment both show these nulls. Figure 23 indicates the vanishing of the angular selectivity nulls as the grating develops and begins to show nonuniformity in the amplitude of the refractive index modulation with z (see inset in Fig. 23). Figure 24 shows the angular selectivity and the index profile for the same conditions after further exposure. Note that $\alpha_o = 0$. Figure 24 illustrates that the absolute maximum diffraction intensity peak now occurs off the Bragg angle. The pattern is symmetric with respect to the Bragg angle and thus a second peak occurs for an angle of incidence on the other side of the Bragg angle.

3.5 Discussion

The prediction of a very wide variety of results in volume holography is possible with the dynamic theory. Writing and reading characteristic curves (usually presented as η vs. t) may have an infinitude of possible magnitudes and shapes. The calculated curves presented in this chapter are typical results taken from a much larger number of cases that have been analyzed by the writer. Many rapidly-varying, experimental writing and reading results (such as the data shown in Fig. 21) have previously, informally, been attributed to "experimental problems." It is now apparent that these types of oscillatory results are "normal" and are to be expected.

The dynamic theory is an important aid in identifying the "significant" parameters in volume holographic recording and readout.

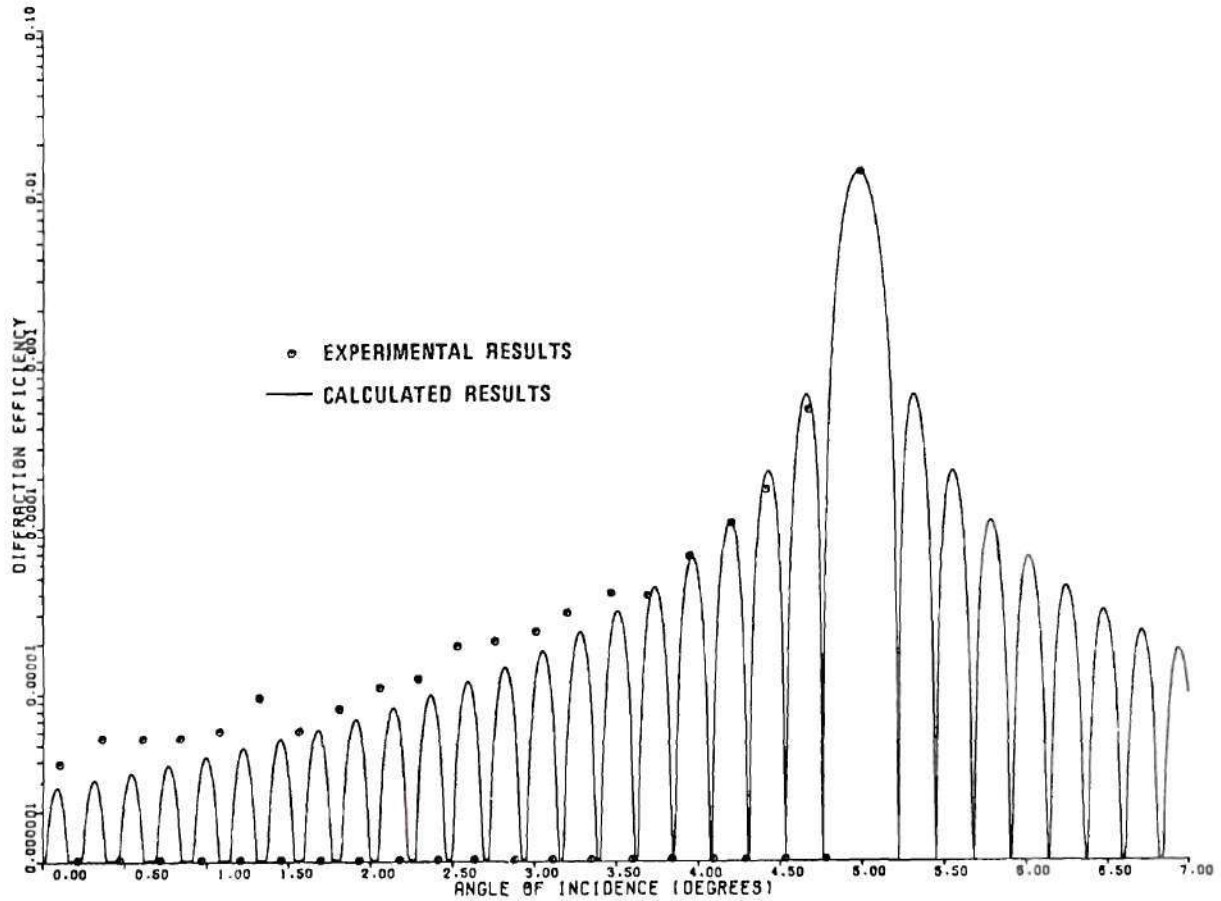

Figure 22. Experimental and Calculated Angular Selectivity Exhibiting Zero Diffraction Efficiency at Minima. The Hologram is 1.66 mm Thick, Iron-Doped Lithium Niobate Crystal. Experimentally, the Hologram was Written with a Wavelength of 514.5 nm, a Total Power Density of 3.5 mw/mm^2, External Angles of Incidence of $\pm 5.00°$, a Writing Time of 5 sec., Polarization in the Plane of Incidence, and the Configuration Shown in the Inset of Figure 6. The Angular Selectivity was Measured with a Low Power Beam of the Same Wavelength. The Calculated Curve is for a Hologram of Thickness 1.66 mm, Written with R_o = 571 v/m, S_o = 518 v/m for 5 sec. with a = 3.8×10^{-12} (volt/m)$^{-2}$ sec^{-1}, $\phi_n = 0°$, and $\alpha_o = 0$, These Parameters Being Estimated from the Experimental Conditions.

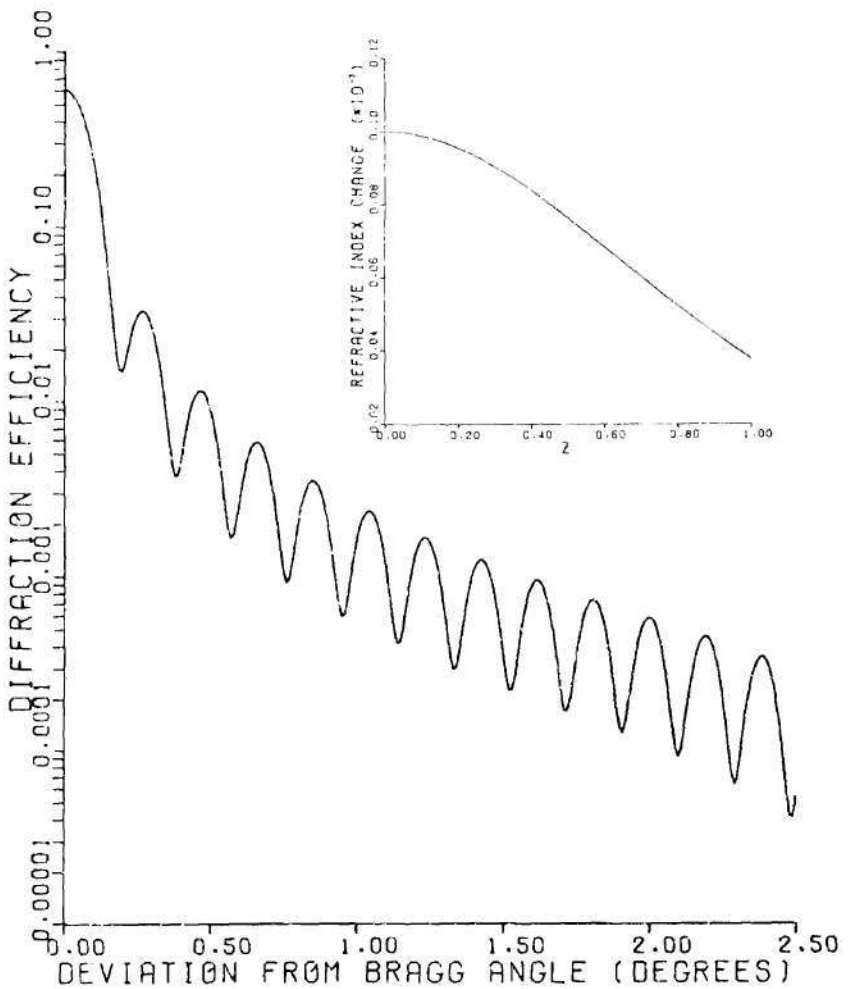

Figure 23. Calculated Angular Selectivity Exhibiting Nonzero Diffraction Efficiency at Minima. Nonzero Minima are Characteristic of a Phase Holographic Grating Having a Variation in Index of Refraction Through the Thickness of the Material. The Refractive Index Profile is Shown in the Inset. Hologram Thickness is 2.00 mm, $a = 10^{-11}(\text{volt/m})^{-2}\text{sec}^{-1}$, $\phi_n = 90°$, $\alpha_o = 0$, and the Writing Time is 5 sec.

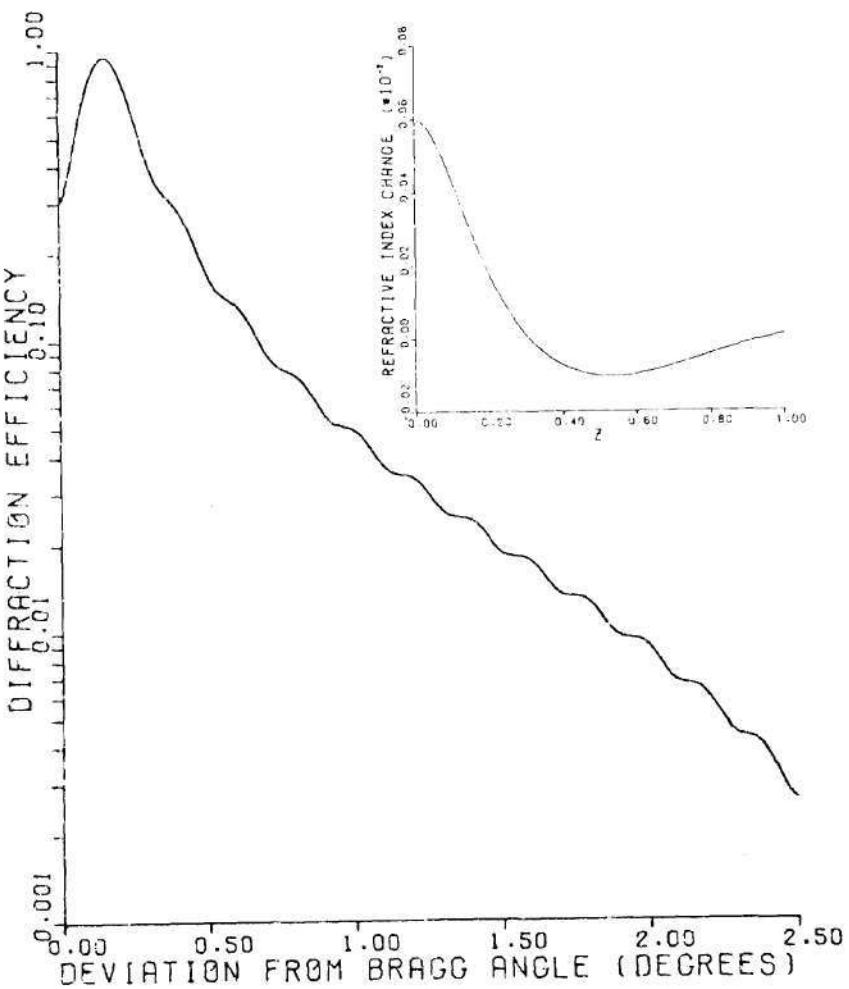

Figure 24. Calculated Angular Selectivity Showing the Disappearance of Diffraction Efficiency Minima. The Same Conditions as Figure 23 Prevail but with a Longer Writing Time of 30 Seconds. The Increased Nonuniformity of the Grating Profile is Shown in the Inset.

Relatively few parameters are needed in the dynamic theory. The role of each of these parameters can be determined in a given situation. This indicates the possibility of using the dynamic theory 1) as an aid in synthesis and 2) as a diagnostic tool.

As an aid in synthesis, the dynamic theory serves as an indicator of the parameter values that are needed to produce a particular desired situation (e.g. uniformity of induced change through the thickness of a hologram, a certain type of angular selectivity, an enhancing readout, a rapidly erasing readout, etc.). The dynamic theory parameters in some materials, indeed, may be controlled in a fairly direct manner. For example, in iron-doped lithium niobate, α_o and a may be dramatically changed by heat treating the material in various environments.[38,39] Microscopically, this has been shown to control the relative Fe^{2+} and Fe^{3+} concentrations in iron-doped lithium niobate.[38,39] In addition, the phase difference between the light and the refractive index grating, ϕ_n, approaches 0° when drift of the photo-excited electrons dominates[20] (which may be induced by externally applying an electric field). The phase difference approaches 90° when diffusion of the electrons dominates[20] (which may be induced by using a small fundamental grating spacing).

As a diagnostic tool, the dynamic theory, when coupled with experiment, is capable of determining certain material and hologram characteristics. By experimentally holding constant some of the dynamic theory parameters, other parameters and properties may be found. For example, the variations with grating thickness of the refractive index may be determined knowing the conditions of recording. This allows the

direct determination of the index profile (in the z-direction) as opposed to assuming a uniform grating or an exponential variation with thickness (both of which may be totally incorrect). As another example, the variation with exposure of the refractive index exposure sensitivity, a, may be measured. By holding the other dynamic theory parameters constant and measuring the hologram writing characteristic, the dynamic range of a may be estimated. Chronologically, in the literature, the earlier thick recording materials tended to show a saturating-type writing characteristic indicating a rapidly decreasing value of a. More recently, higher sensitivity materials have tended to show an oscillatory writing characteristic indicating a larger dynamic range for these materials (and thus the dynamic theory is valid in these cases with essentially a constant value of a).

3.6 Conclusions

A large number of different types of recording and reading behaviors have been reported for thick (volume) holograms in a wide variety of recording materials. Writing, reading, and angular selectivity experimental data from approximately 25 published articles are cited in this chapter as being representative of the known types of behavior. The dynamic theory of thick hologram recording and reading qualitatively predicts all of these various types of experimental behavior. Thus, the dynamic theory is potentially very powerful 1) in determining the material and recording parameters needed to produce a certain desired hologram characteristic and 2) as a diagnostic tool to analyze the parameters of thick photosensitive recording materials.

CHAPTER IV

THEORETICAL TERMINAL CHARACTERISTICS AND ASSOCIATED INTERNAL PROFILES

4.1 Introduction

In the previous chapter, it was shown that the dynamic theory is successful in qualitatively predicting the various types of experimentally observed terminal characteristics of thick holograms for arbitrary exposures. In support of the theory, reference was made to specific experimental data (from the published literature or measured by the writer) bearing resemblance to the calculated characteristics. In this chapter, the theory is used without much direct reference to experimental results to calculate the terminal (output) characteristics of transmission phase volume hologram gratings and the associated internal material profiles. The variations of the holographic diffraction efficiency with respect to the parameters that enter the theory are considered for writing. Examples of the functions associated with volume holograms are calculated and shown for typical experimental parameters. The angular selectivity and dynamic readout characteristics for these typical holographic gratings are then calculated. The material presented is intended to illustrate the possible multiformity of the holographic diffraction efficiency characteristics and to exemplify the spatial and temporal variations of the important internal distributions that can be expected in thick gratings.

The formulas and terminology used in this chapter are given in Chapter II. It is assumed that writing and readout are performed at the same wavelength, that is $\lambda = \lambda' = 0.5145$ μm. The material is assumed to be a 2mm thick crystal of $LiNbO_3$ that has average index of refraction $n_o = 2.2426$ at this wavelength and writing angle $\theta = \pm 2.23°$ ($\pm 5°$ externally). These values correspond to the experimental arrangement used in this work. The exposure sensitivity is taken to be $a = 10^{-11}$ $(volt/m)^{-2}$ sec^{-1} which is of the proper order of magnitude as estimated from several experiments (see Chapter V).

The parameters λ, θ, a, and d do not strongly influence the hologram behavior as calculated by the dynamic coupled-wave equations. The variation of $\cos\theta$ is not great in practice and the wavelength is in the visible region of the spectrum in this work. (Of course, the larger θ is and the smaller λ is, the smaller the grating period becomes. This affects the relative contributions of the microscopic transport processes (drift and diffusion) that occur and, thus, the value of ϕ_n. However, this is not a consideration here since the calculations are given with ϕ_n as a parameter and span its range.) The sensitivity, a, only governs the rate with which the holographic features develop in time but does not otherwise alter the behavior. The thickness has a similar effect but additionally has the usual influence on the width of the angular selectivity central lobe. That is, generally, the thicker the crystal is, the narrower the angular corridor (around the Bragg angle) for reconstruction becomes, allowing, in practice, higher density of angularly stacked holograms without crosstalk.

On the contrary, the parameters α_o, α_o', ϕ_n, and the boundary values (R_o, S_o, R_o', S_o') have strong and interesting effects on the behavior. Therefore, emphasis is presently placed on studying these. In this chapter, $\alpha_o' = \alpha_o$ is used for simplicity.

4.2 Writing Diffraction Efficiency

The maximum diffraction efficiency of a transmission volume phase hologram grating depends on the absorption constant for the readout process, the phase shift ϕ_n, and the relative values of the boundary conditions R_o and S_o. Figure 25 illustrates that for a lossless hologram with $R_o = S_o$, 100% efficiency is possible for $\phi_n = 0°$. The maximum value decreases with increasing ϕ_n. Also, the oscillations of the efficiency diminish as ϕ_n increases. For $\phi_n \neq 0°$, a z-dependent phase difference for the two waves develops with time. This causes grating bending as discussed in Chapter II. Only for $\phi_n = 0°$ is the grating produced uniform with thickness and not bent for this lossless hologram. For $\phi_n \neq 0°$, grating bending and grating nonuniformity arise.

Figures 26 and 27 show the effects of the boundary conditions for a lossless hologram. Since $R_o > S_o$, 100% efficiency is not achieved, even for $\phi_n = 0°$. The efficiency is also greatly reduced for the other phase shifts shown. The reason for this is the erasing action of the uninterfered component of the R-wave. This is consistent with the observation (see Sec. 4.5) that, generally, dynamic readout with the R-wave causes loss in diffraction efficiency (erasure). Figure 27 shows an extreme case where $R_o = 10\ S_o$. The gratings corresponding

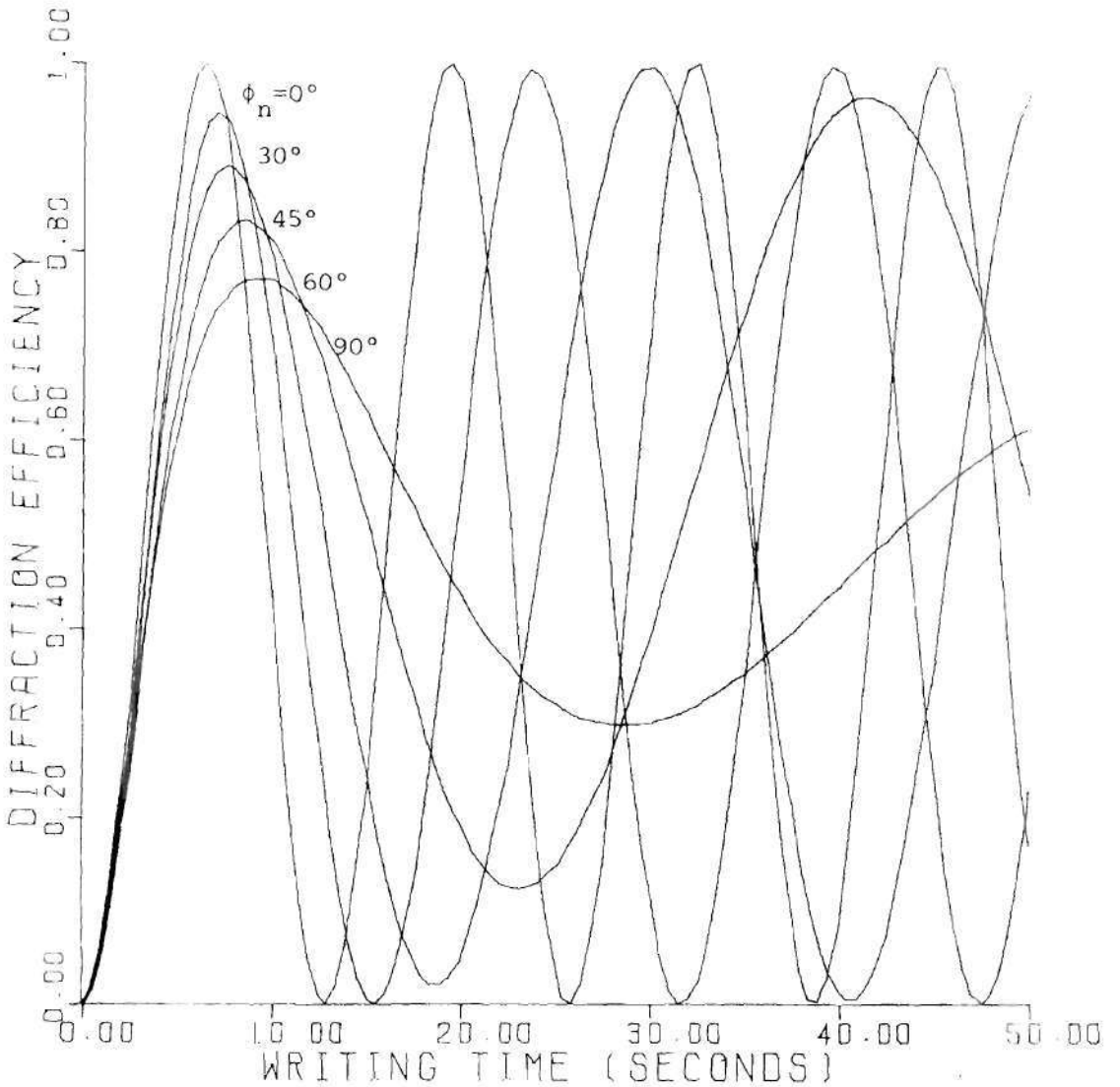

Figure 25. Calculated Writing Characteristics for Lossless Holograms. $R_o = S_o =$ 1000 volt/m and $\alpha_o = 0$.

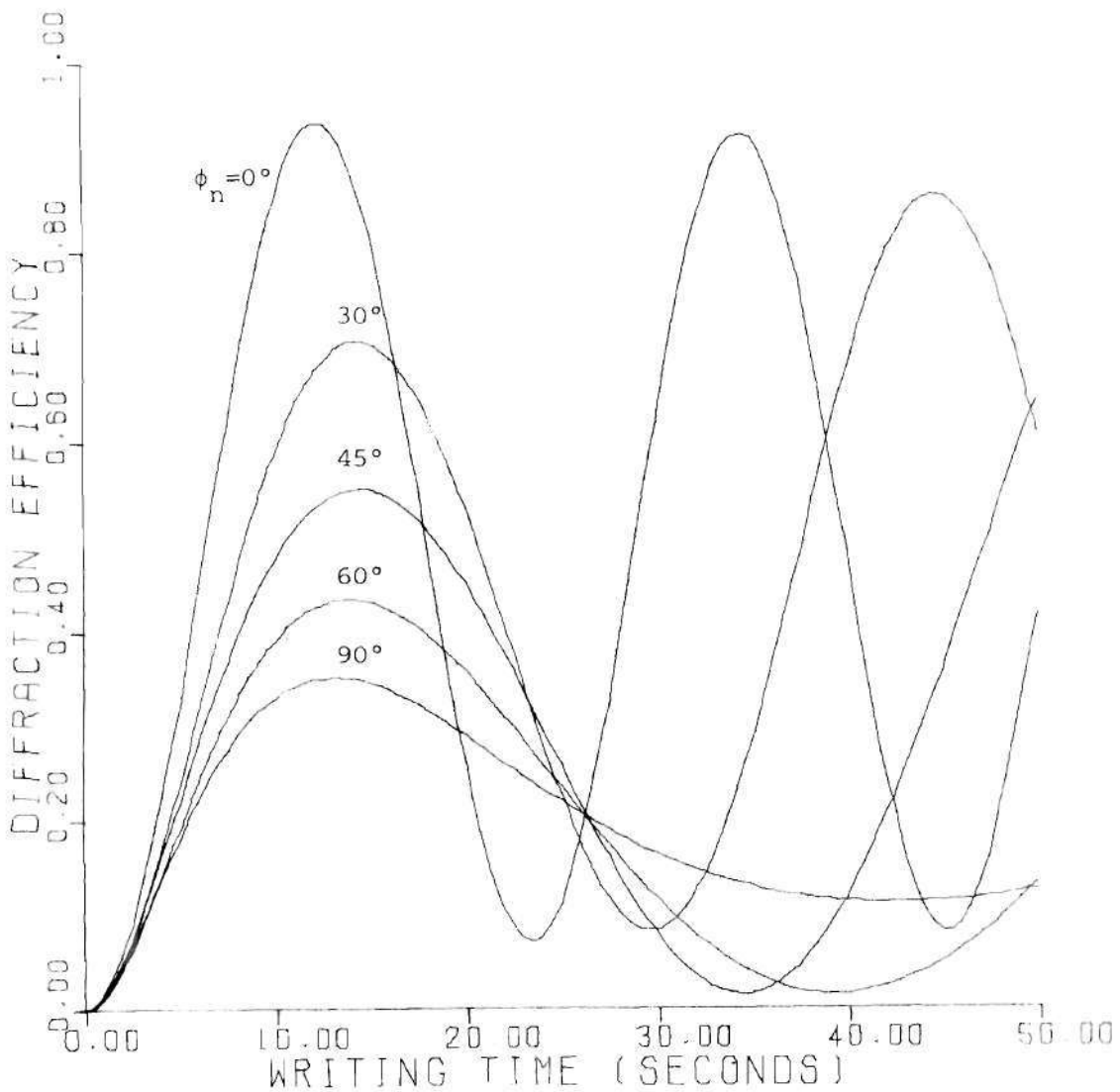

Figure 26. Calculated Writing Characteristics for Lossless Holograms Using Unequal Boundary Values. R_o = 1000 volt/m, S_o = 500 volt/m, and α_o = 0.

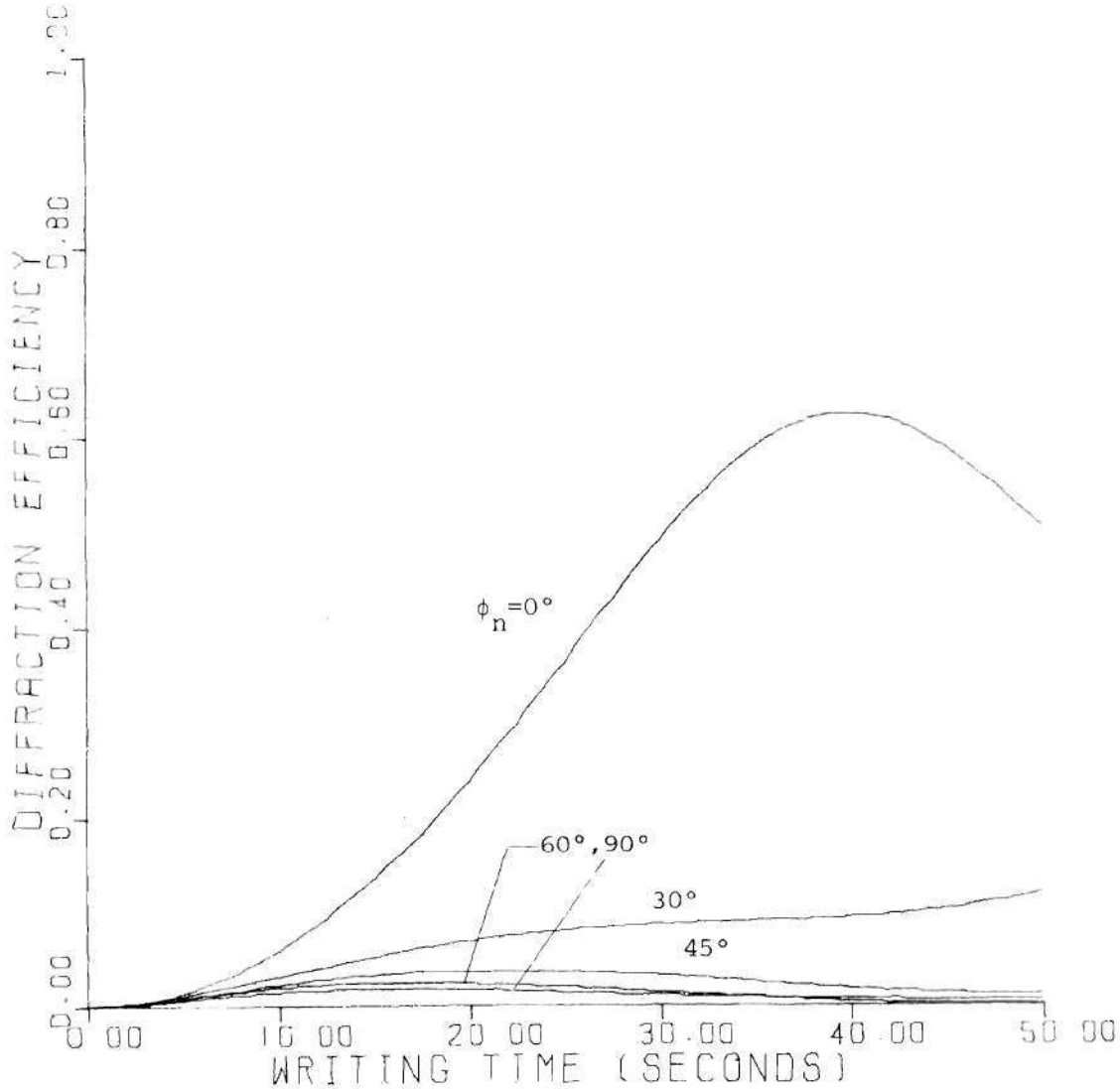

Figure 27. Calculated Writing Characteristics for Lossless Holograms Using Unequal Boundary Values. R_o = 1000 volt/m, S_o = 100 volt/m, and α_o = 0.

to Figs. 26 and 27 are bent and nonuniform for all ϕ_n. For $\phi_n = 0°$, the gratings actually grow in amplitude with thickness. Since, for all ϕ_n, when $R_o = S_o$ and $\alpha_o \neq 0$, the grating amplitudes decrease with thickness, this indicates that to produce uniform gratings in practical lossy materials, an electric field could be applied to make ϕ_n approach 0° (drift) and some beam inequality allowed to compensate for the grating amplitude drop due to absorption. The actual conditions necessary for a given situation can be obtained from the dynamic theory. The consequences of beam inequality are reduced index modulation amplitudes and slower development (less power applied).

Figures 28 and 29 illustrate the same case for $S_o > R_o$. The behavior is drastically different. Now almost 100% efficiency is reached for all ϕ_n except 0° when $S_o = 2\ R_o$. For $S_o = 10\ R_o$, the maximum efficiency occurs at $\phi_n = 90°$. The reason for these high efficiencies is the enhancing action of the uninterfered component of the S-wave. This is consistent with the observation (see Sec. 4.5) that, generally, dynamic readout with the S-wave causes an increase in diffraction efficiency (enhancement). The grating peaks and grating phases are functionally somewhat different from those corresponding to the previous two figures (except for $\phi_n = 0°$) but similar comments apply.

Figure 30 illustrates the realistic case of a lossy recording material. The maximum efficiencies are seen to drop but the functional forms remain similar to the corresponding lossless case (Fig. 25). It turns out that the curve for $\phi_n = 0°$ is accurately described for all times by the analytical expression for η given by Eq. (B24) in Appendix

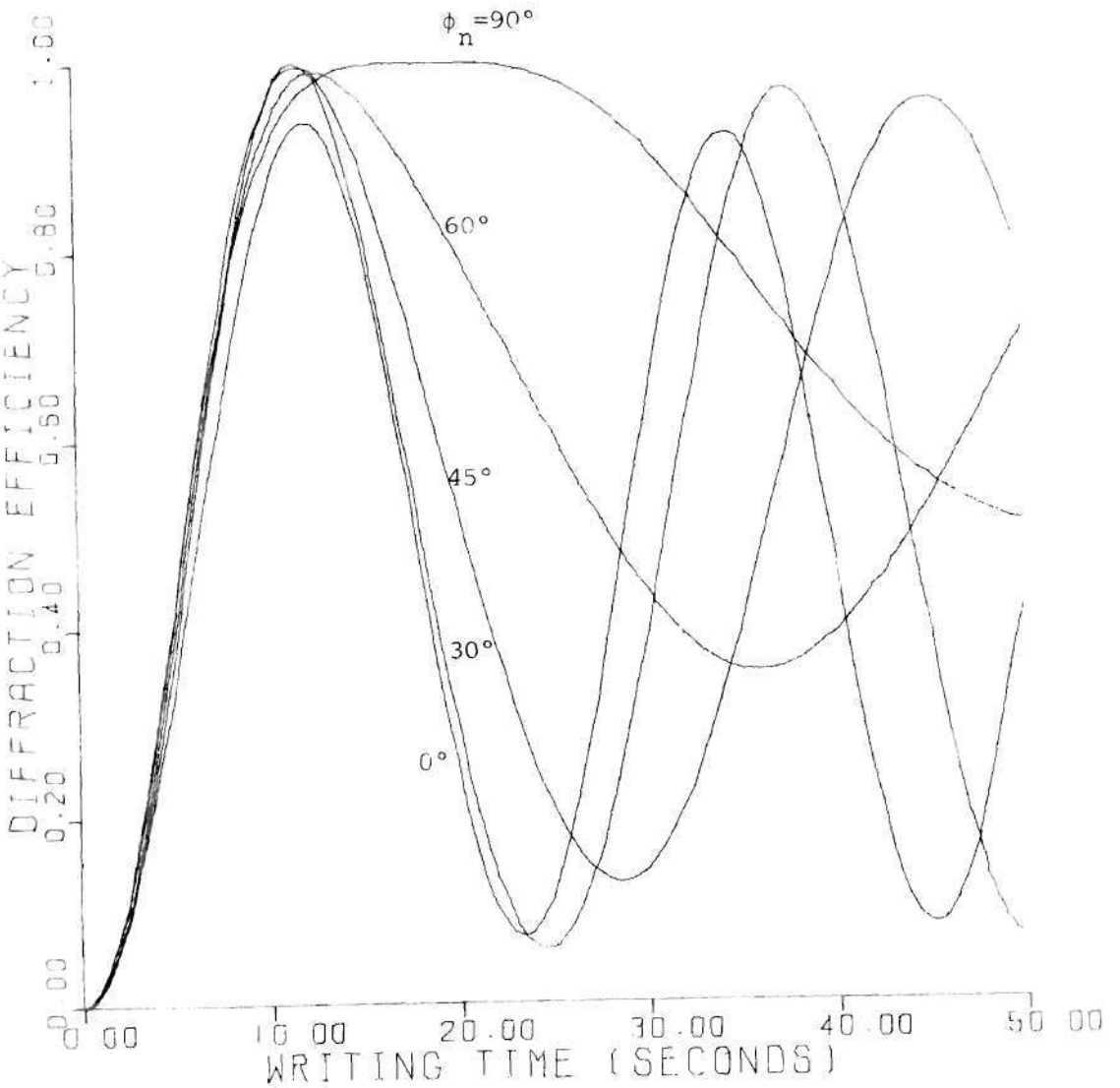

Figure 28. Calculated Writing Characteristics for Lossless Holograms Using Unequal Boundary Values. R_o = 500 volt/m and S_o = 1000 volt/m, and α_o = 0.

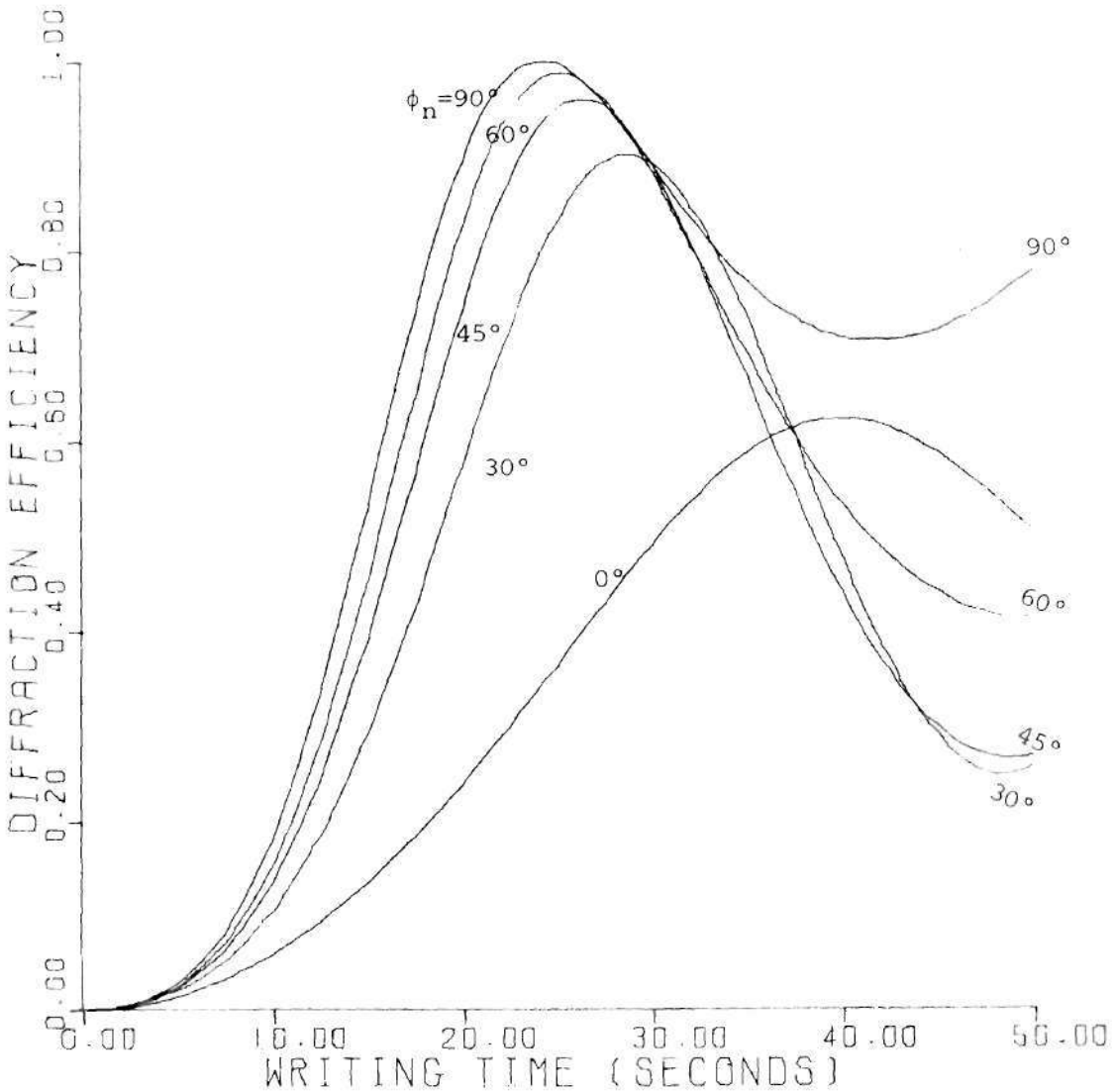

Figure 29. Calculated Writing Characteristics for Lossless Holograms Using Unequal Boundary Values. R_o = 100 volt/m, S_o = 1000 volt/m, and α_o = 0.

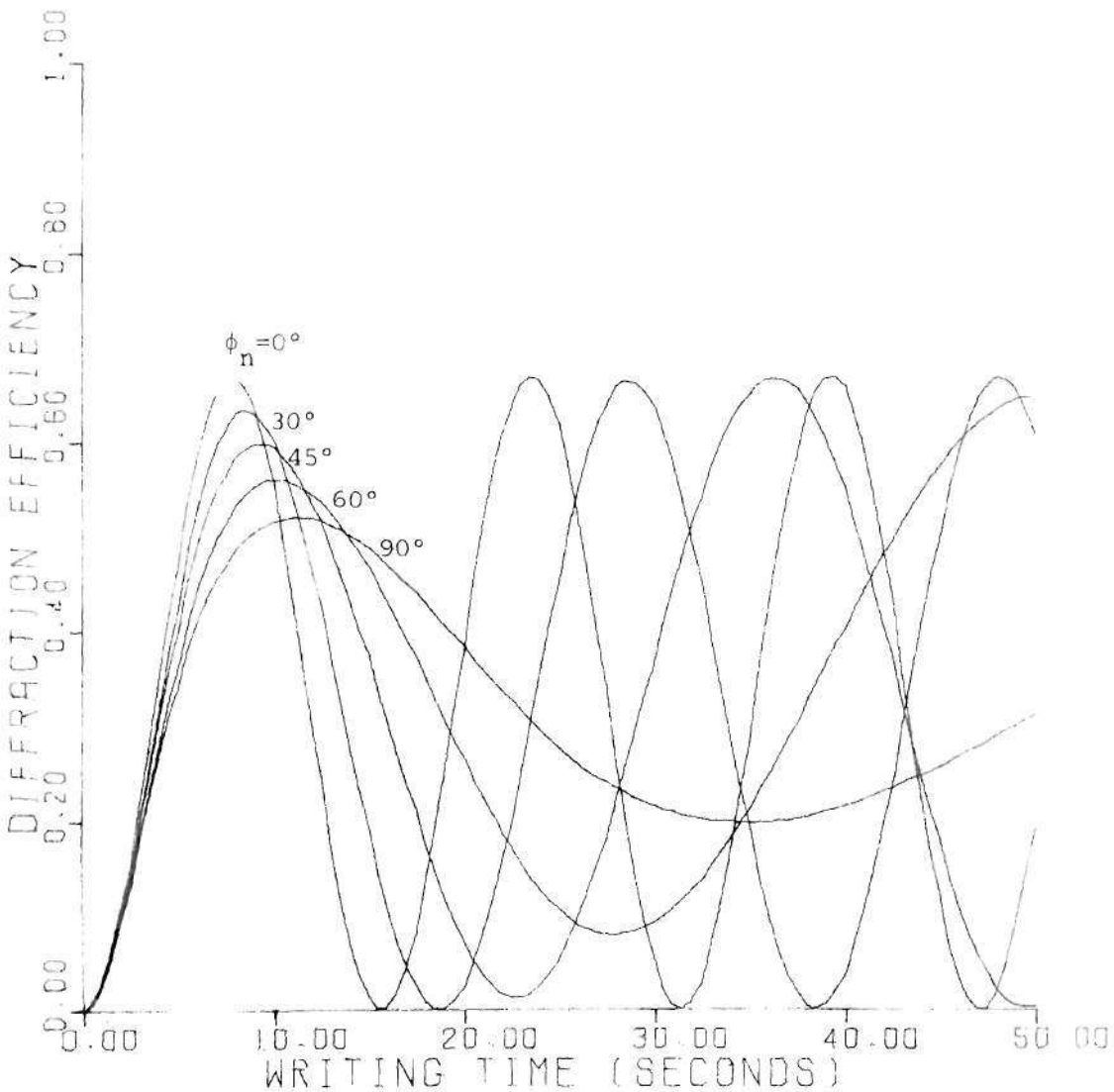

Figure 30. Calculated Writing Characteristics for Realistic Lossy Holograms. $R_o = S_o =$ 1000 volt/m and $\alpha_o = 100\ m^{-1}$.

B. The maximum diffraction efficiency obtainable for any transmission phase hologram with equal boundary conditions (the formula is valid only if $R_o = S_o$) is, therefore, less than or equal to $\exp(-2\alpha_o' d/\cos\theta')$. It is thus important to read the hologram at a wavelength at which the absorption coefficient α_o' is small in applications requiring high diffraction efficiency. This is consistent with observations by Ninomyia[21] that it is the absorption in the readout process that limits the maximum efficiency attainable but not the absorption associated with the recording process. However, the higher the absorption for the writing beams, the slower the hologram develops for a given input power density and exposure sensitivity.

Figures 31 and 32 depict the effects of unequal boundary conditions on realistic lossy holograms. These figures correspond to Figs. 26 and 28, respectively. It is interesting to note that the maximum diffraction efficiency reached, even in the case of an uninterfered enhancing writing beam component (Fig. 32), for several values of ϕ_n, is still $\exp(-2\alpha_o' d/\cos\theta')$. Thus, this appears to be an inherent property of volume holograms irrespective of phase shifts and beam ratios. The peak amplitudes of the gratings associated with the writing processes of Figs. 31 and 32 are shown in Figs. 33 and 34, respectively. Note the differences in the functional forms. For $\phi_n = 0°$, these are considerably more nearly uniform than the grating shown in Fig. 38 which corresponds to the lossy case with equal input beams (Fig. 30). It appears that partial compensation for loss-induced grating nonuniformity by using unequal boundary conditions has been accomplished. The amplitude of the index grating is, however, reduced by about 50% using such

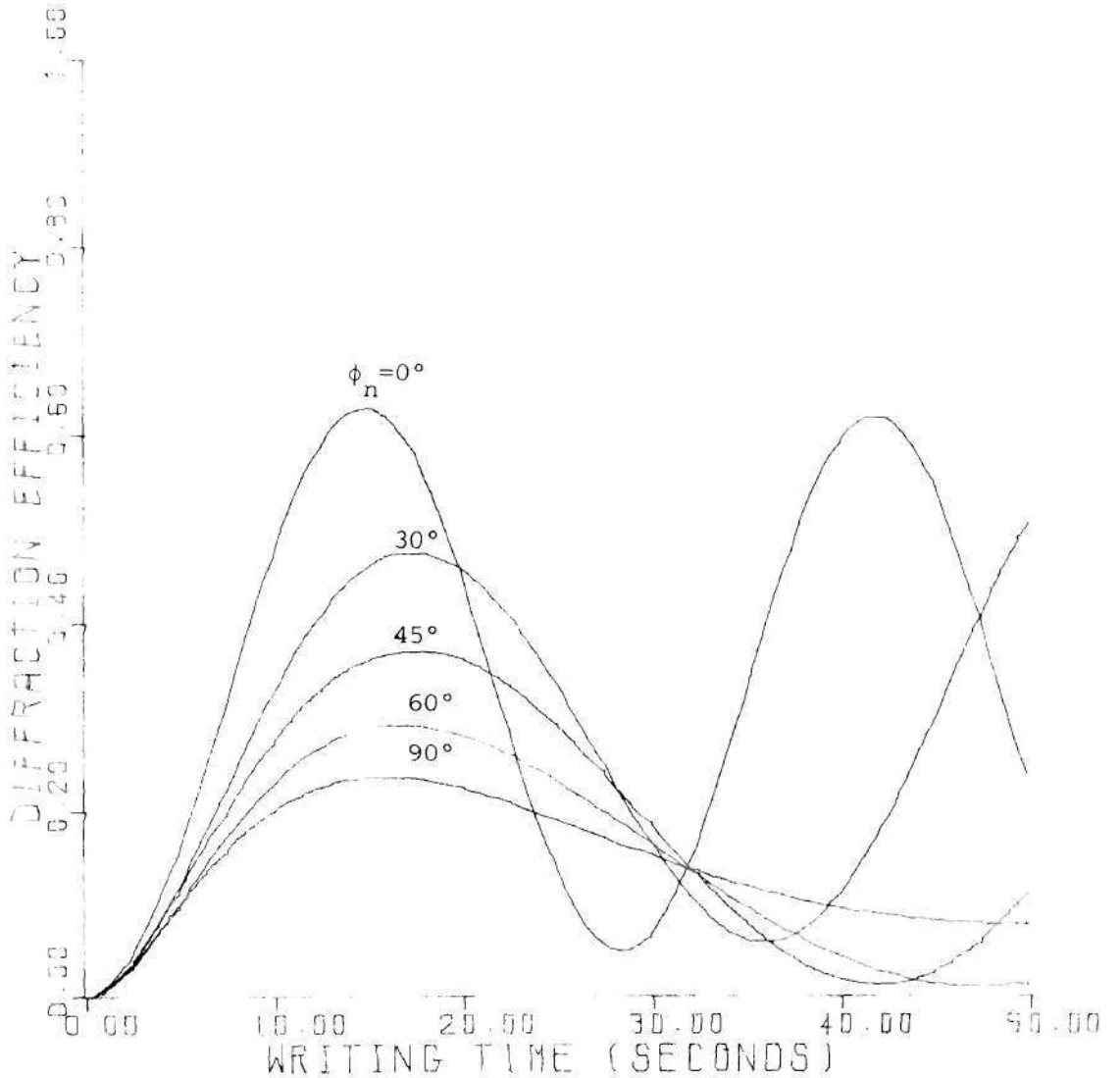

Figure 31. Calculated Writing Characteristics for Realistic Lossy Holograms Using Unequal Boundary Values. R_o = 1000 volt/m, S_o = 500 volt/m, and α_o = 100 m^{-1}.

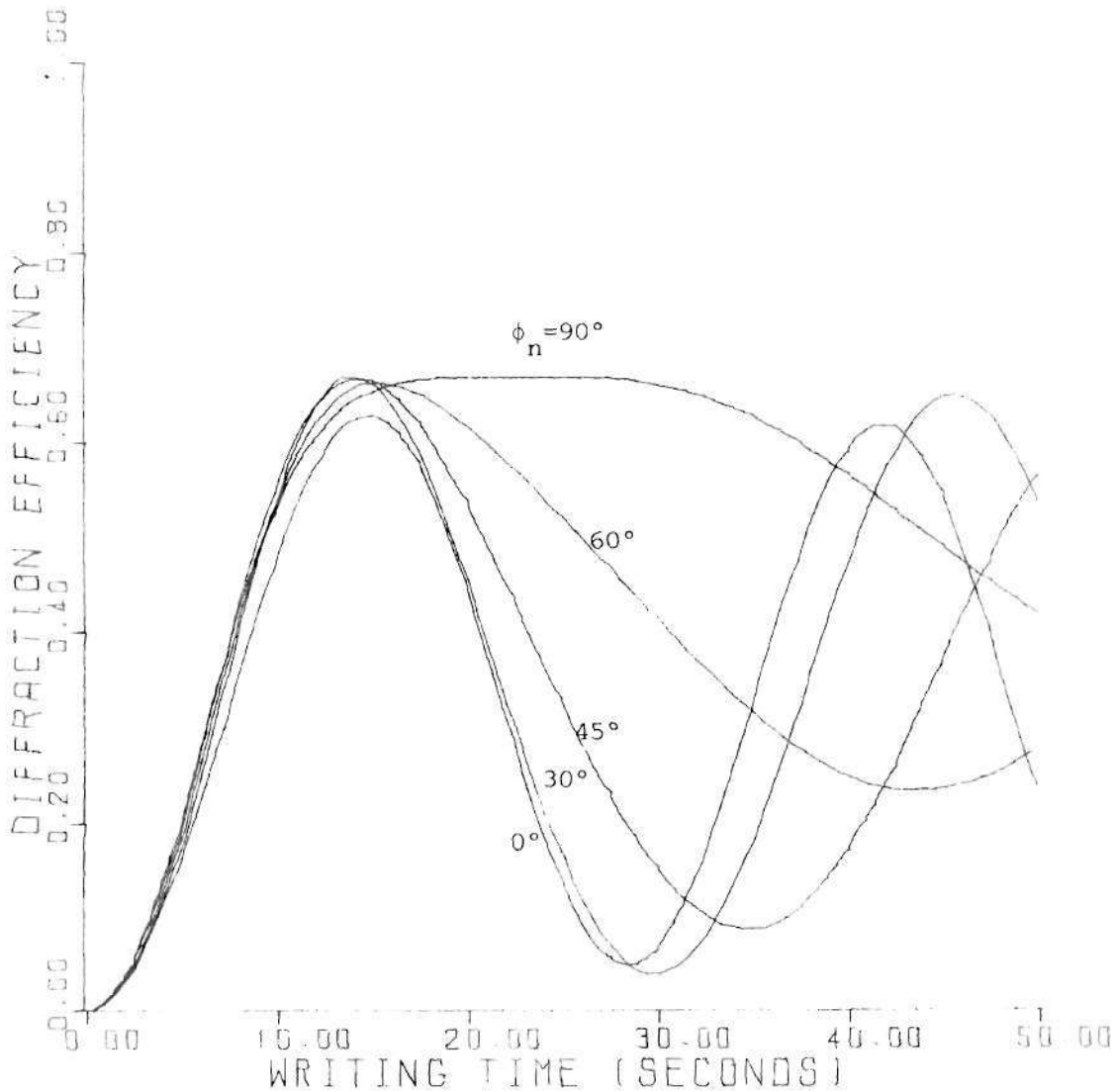

Figure 32. Calculated Writing Characteristics for Realistic Lossy Holograms Using Unequal Boundary Values. R_o = 500 volt/m, S_o = 1000 volt/m, and α_o = 100 m^{-1}.

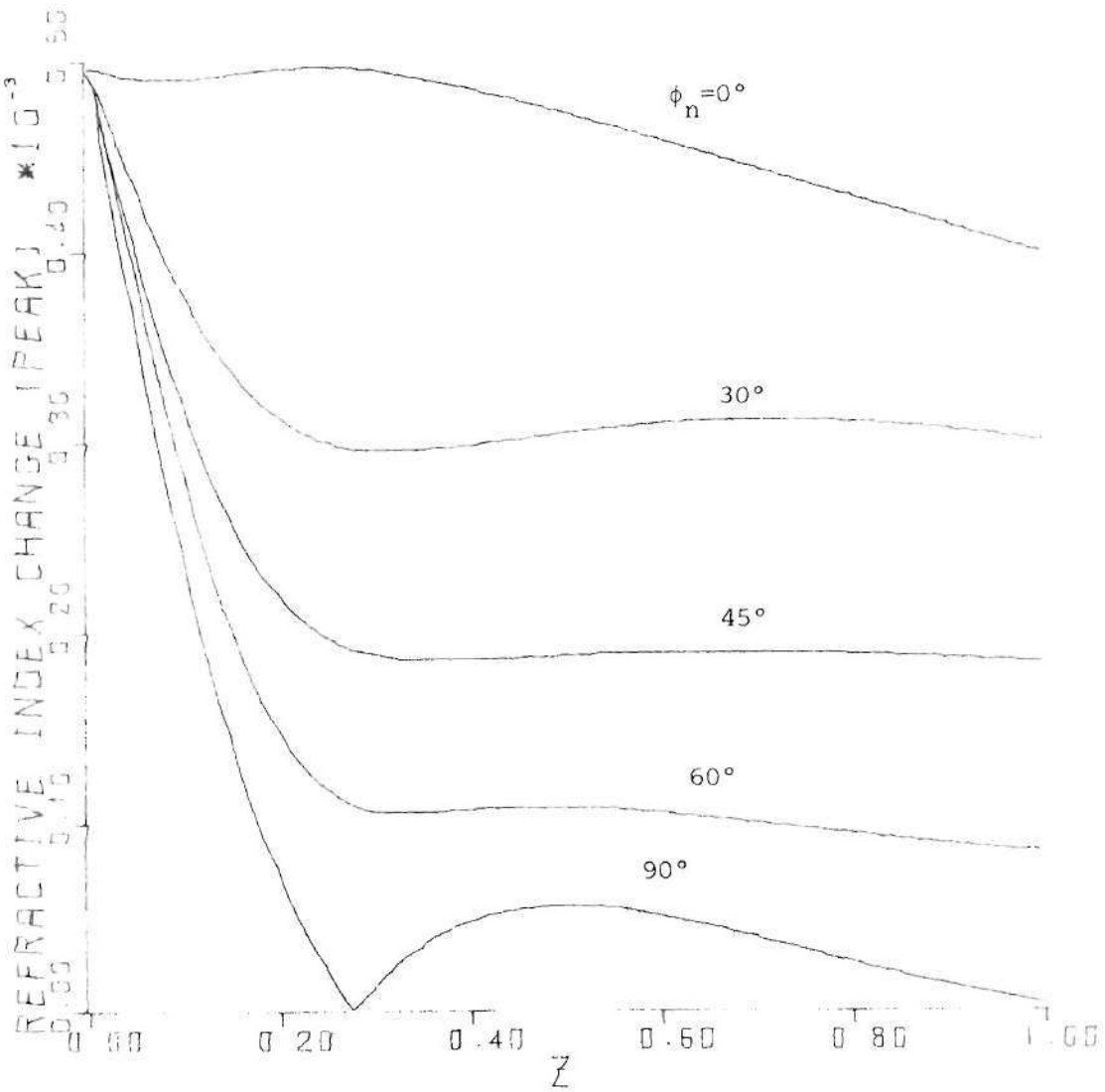

Figure 33. Calculated Grating Peak Amplitudes Produced by the Writing Processes of Figure 31. T = 50 sec.

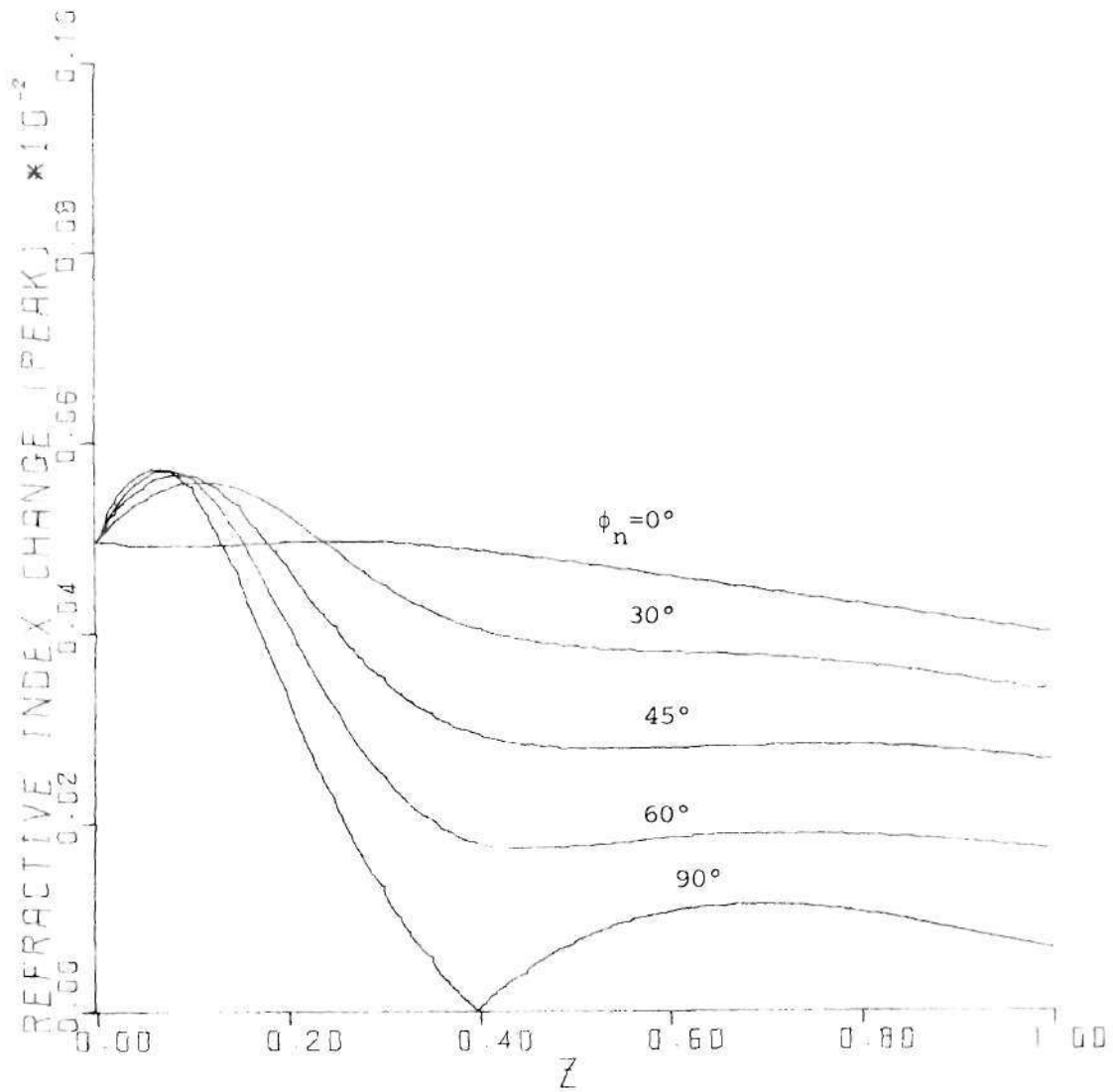

Figure 34. Calculated Grating Peak Amplitudes Produced by the Writing Processes of Figure 32. T = 50 sec.

compensation in this particular instance.

In Figs. 35 and 36, the effects of a time dependent exposure sensitivity are considered. As a first order approximation, the sensitivity is taken to be an exponentially decaying function of time. This is consistent with the conclusions of recent (independent) studies[55-57] on the form of the internal space-charge generated electric field pattern (x-direction) during hologram formation. This electric field pattern produces the hologram-constituting refractive index modulation via the linear electro-optic effect and these results[55-57] are, therefore, clearly relevant to the present discussion. The time constant in the exponential function, T_o, is approximately the illuminated dielectric relaxation time of the material. From the figures it is seen that a rapidly decaying sensitivity (small T_o) leads to pronounced saturation effects (Fig. 36). The value of ϕ_n can, however, be important (Fig. 35). The characteristics in Fig. 36 have the appearance of those in Figs. 3, 4, and 8(b) which were experimentally observed. In practice, time dependent exposure sensitivities should be used when analyzing hologram storage in materials with short dielectric relaxation times (i.e. if saturating behavior is observed).

4.3 Internal and External Features of Typical Holograms

In this section, examples of the various functions associated with volume holograms are presented for holograms with experimentally realistic parameters. The holograms selected as being representative are those of Fig. 30. The profiles in z given are calculated at the

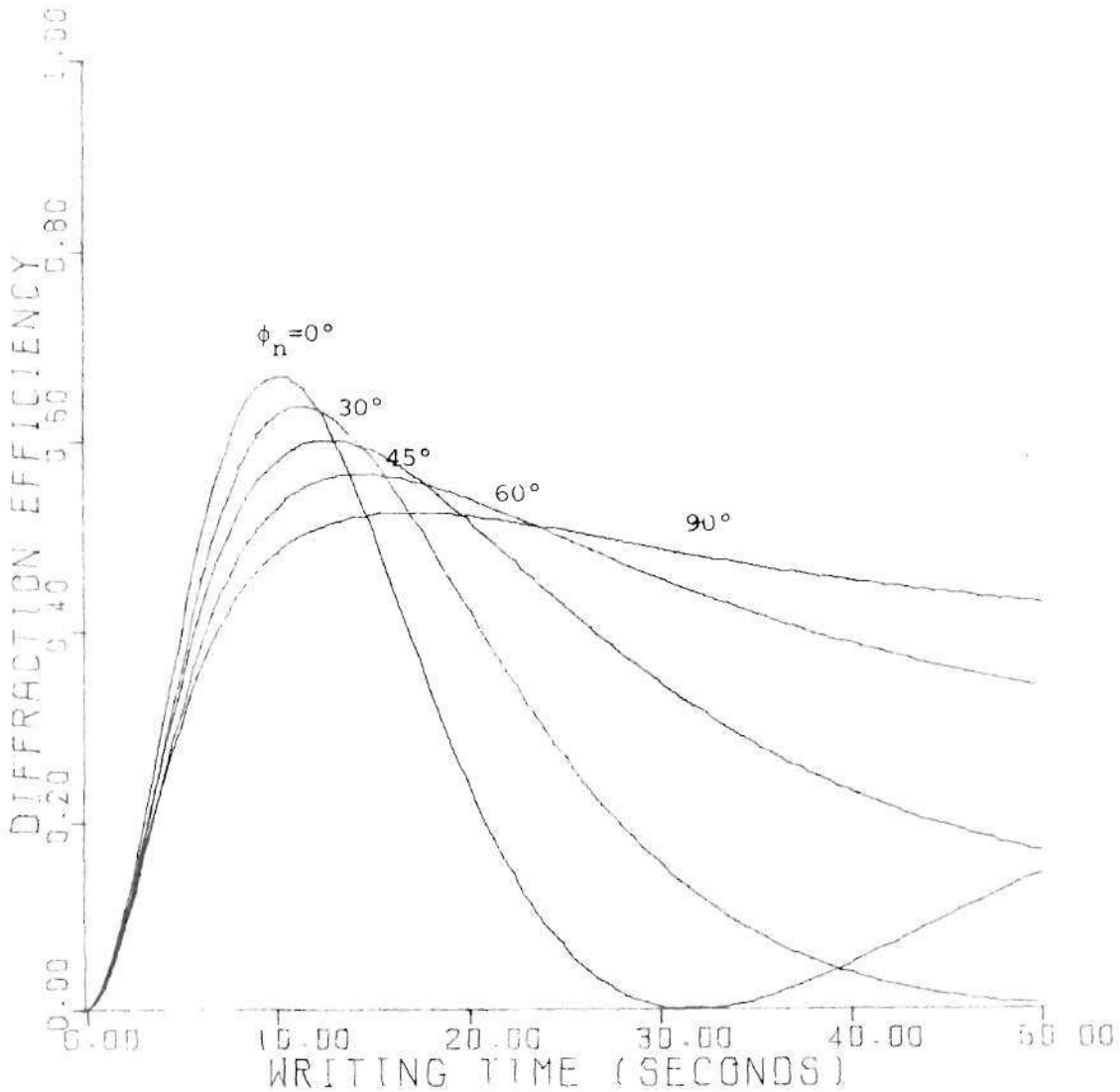

Figure 35. Calculated Writing Characteristics Using a Time Dependent Exposure Sensitivity, $a = a_o \exp(-t/T_o)$. $a_o = 10^{-11}(\text{volt/m})^{-2}\text{sec}^{-1}$, T_o = 20 sec, $S_o = R_o$ = 1000 volt/m, and α_o = 100 m^{-1}.

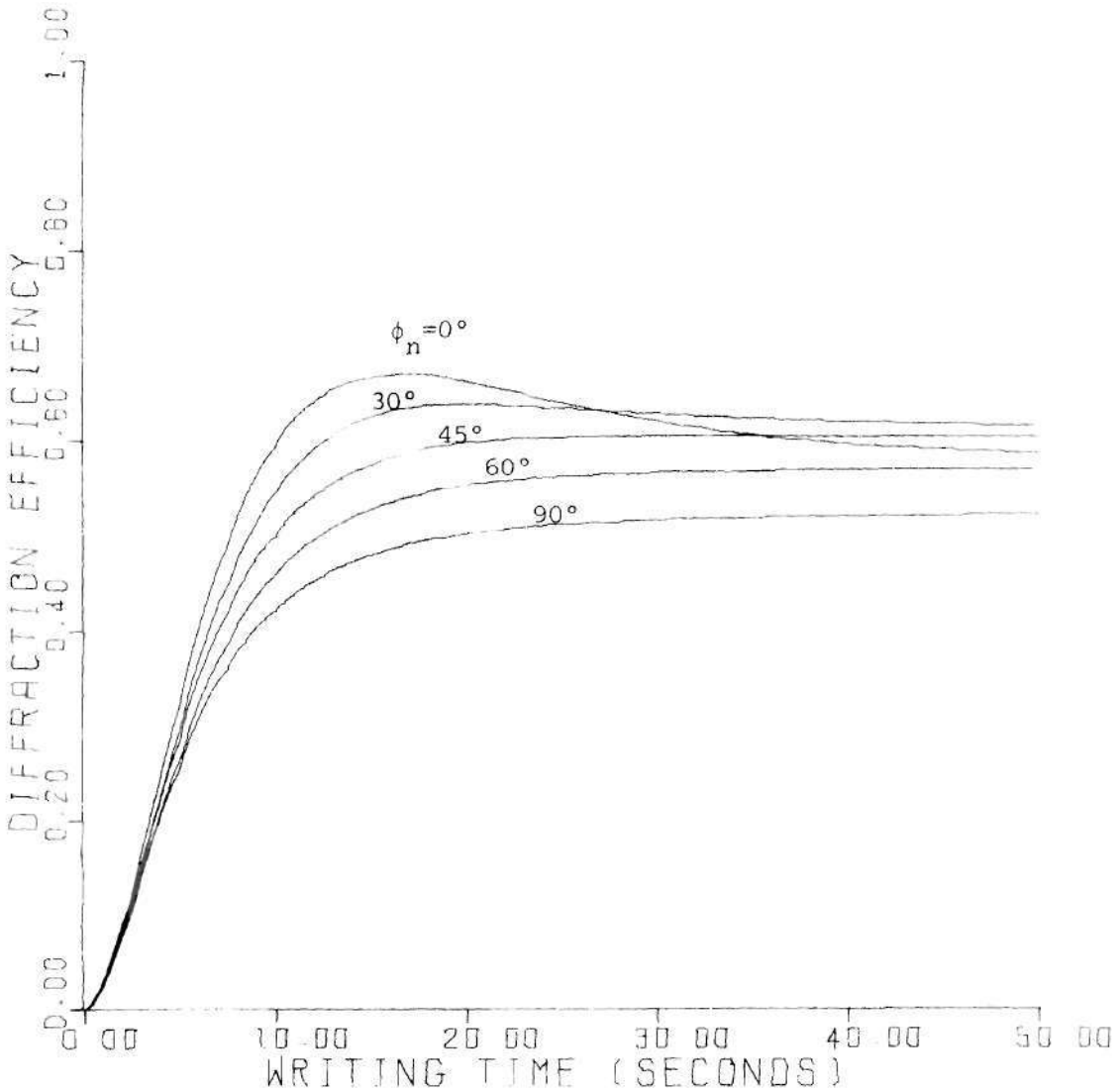

Figure 36. Calculated Writing Characteristics Using a Time Dependent Exposure Sensitivity, $a = a_o \exp(-t/T_o)$. $a_o = 10^{-11}(\text{volt/m})^{-2}\text{sec}^{-1}$, T_o = 10 sec, $S_o = R_o$ = 1000 volt/m, and $\alpha_o = 100\ \text{m}^{-1}$.

end of writing (i.e. the exposure time T = 50 seconds).

It is possible to calculate the holographic refractive index variation with thickness for a cut straight through (parallel to the z-axis) the grating at a specific value of x. Figure 37 gives the results of such a calculation using Eq. (21). A much clearer picture of the z-dependence of the amplitude of the index modulation is obtained by following a peak in the grating through the crystal slab. This is illustrated in Fig. 38. For $\phi_n = 0°$, the drop in the peak amplitude is due solely to the absorption of the material which attenuates the writing beams as they propagate through. The nonuniformity for the other phase shifts is due to the combined effects of the absorption and the interaction (interchange of power or coupling) of the writing waves that occurs for nonzero phase shifts (see Fig. 40). The grating amplitudes have their maxima at the input face, z=0, because no attenuation or wave interaction has occurred there. For large ϕ_n, grating phase reversal occurs. That is, the grating exhibits an amplitude sign-reversal for a range of the thickness coordinate. Figure 39 shows the spatial phase variations (grating bending) of the grating peaks of Fig. 38. Note the phase reversal for $\phi_n = 90°$. For $\phi_n = 60°$, the grating peak has shifted more than three-quarters of the grating period in x at the output plane. No phase shift is produced for $\phi_n = 0°$.

The next two figures illustrate direct properties of the solutions of the dynamic coupled-wave equations, the complex wave amplitudes R and S, for the present example. Figure 40 shows the thickness variations of the irradiances of the signal and reference waves. For $\phi_n = 0°$, the drops in RR* and SS* are caused entirely by

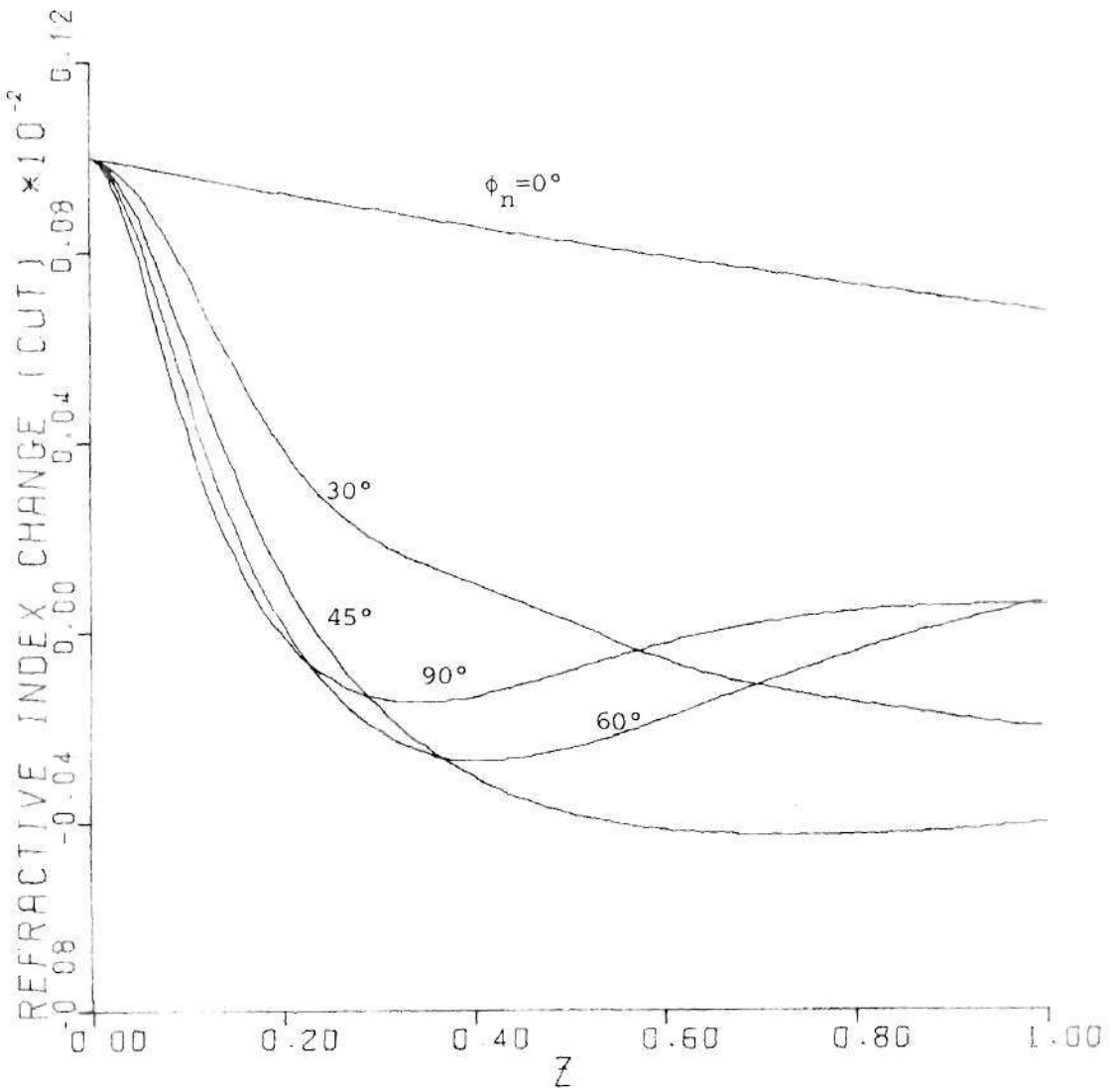

Figure 37. Calculated Grating Profiles at a Selected x-value Corresponding to the Holograms of Figure 30. T = 50 sec.

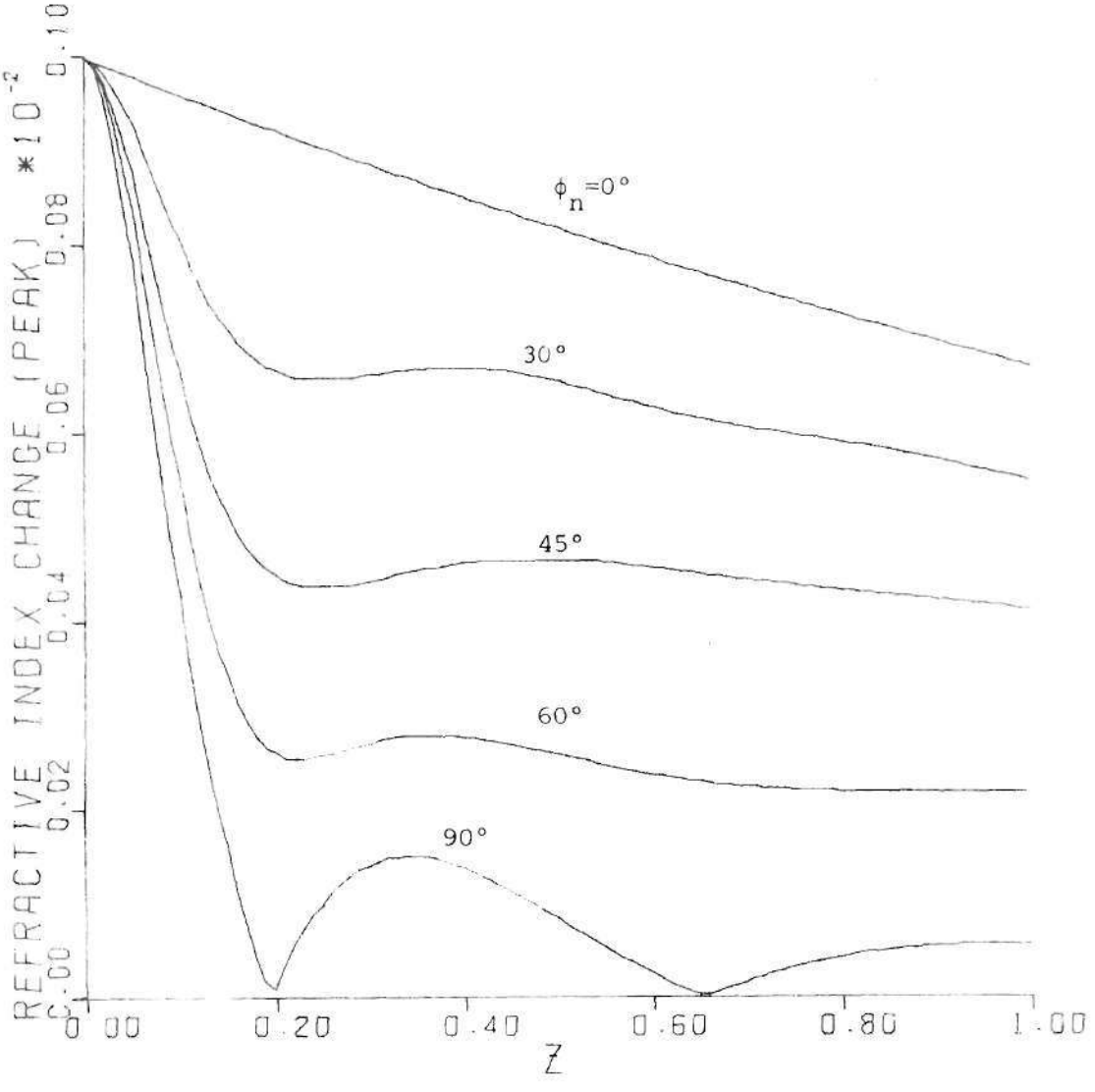

Figure 38. Calculated Grating Peak Amplitudes Corresponding to the Holograms of Figure 30. T = 50 sec.

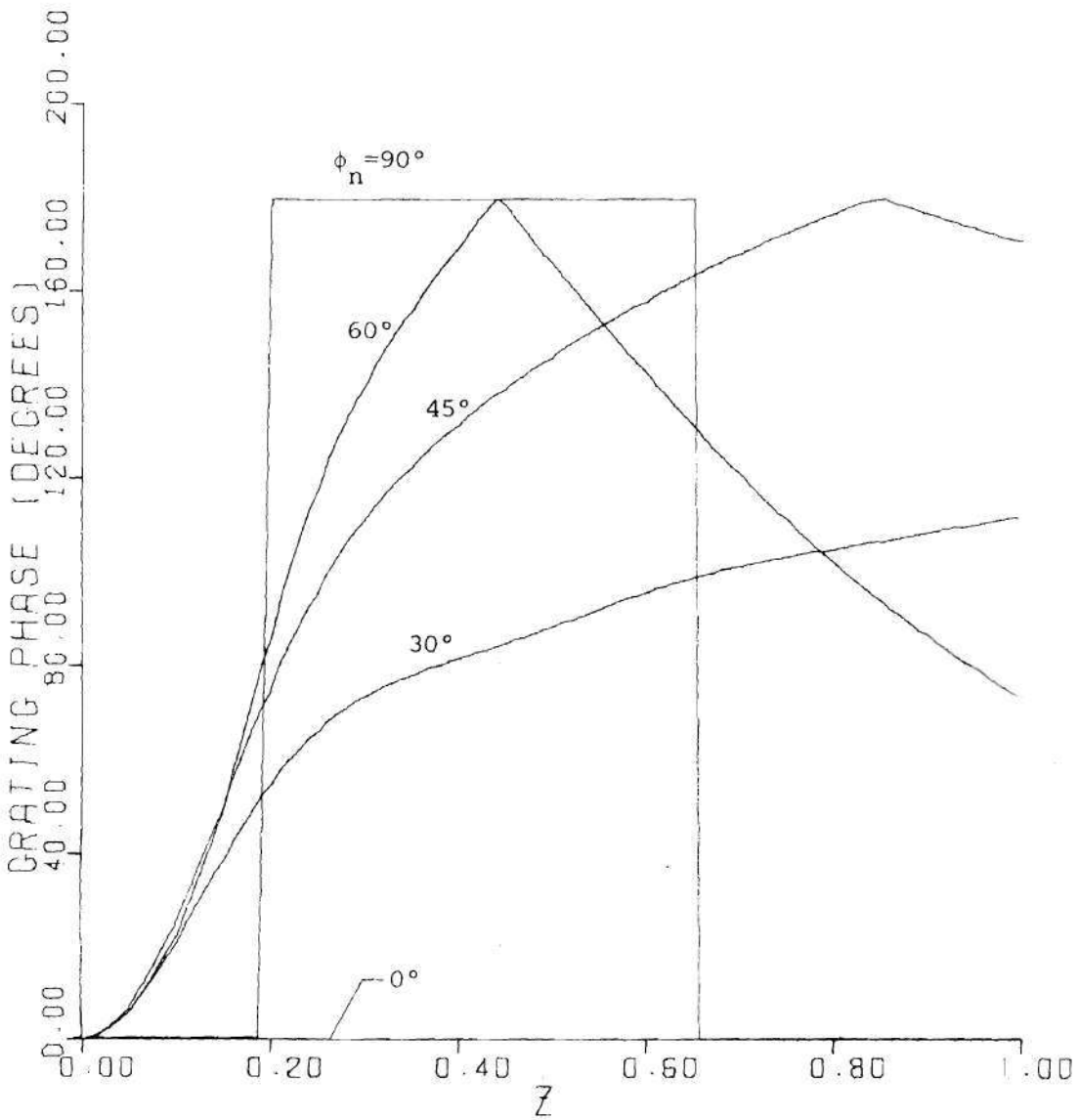

Figure 39. Calculated Spatial Phase Variations of the Grating Peaks of Figure 38.

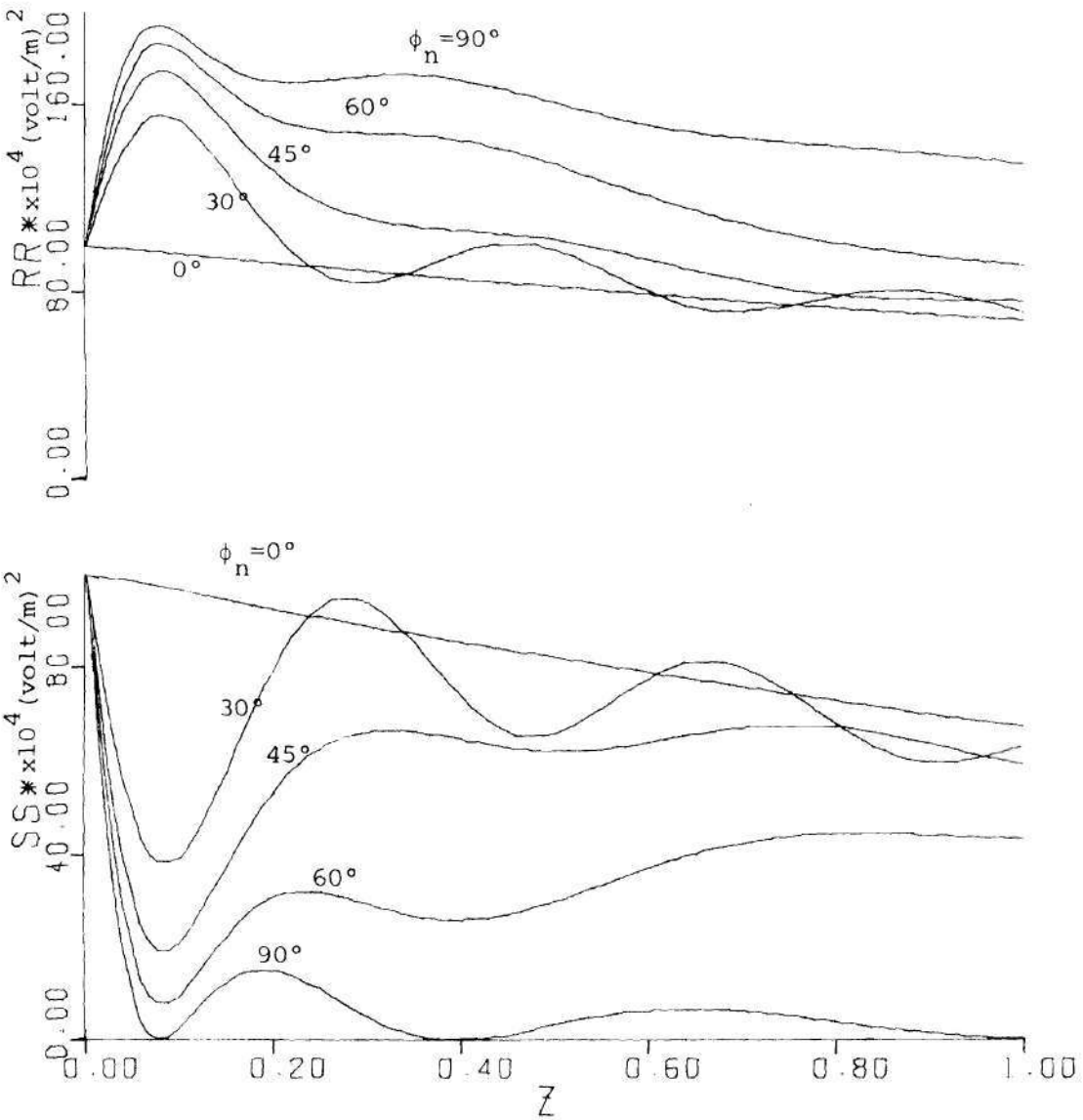

Figure 40. Calculated Distributions of the Irradiances of the Signal and Reference Waves Corresponding to the Holograms of Figure 30. T = 50 sec.

absorption as no coupling takes place. For the other phase shifts, however, strong coupling effects are evident. Of course, the absorption also affects the shapes of the curves for the nonzero phase shifts although not as vividly as the coupling phenomenon. The wave interaction leads to deviation from unity of the beam intensity ratio (defined as $\psi \equiv \psi(z,t) \triangleq SS^*/RR^*$) inside the material even for this case of equal writing beam boundary values ($R_o = S_o$). This can be associated with the nonuniformities of the gratings. That is, the grating formation in the crystal is less efficient where ψ deviates significantly from unity. In Fig. 41, the phase differences of the solutions are shown. The phase difference is zero for $\phi_n = 0°$. For $\phi_n = 90°$, the jump to 180° corresponds to a sign-reversal of the S wave amplitude (see Fig. 40). For $\phi_n = 60°$, the phase difference has almost reached 360° at $z=1$.

In Fig. 42, the amplitude of the refractive index grating along a peak averaged over thickness is given as a function of time as calculated by Eq. (23). For $\phi_n = 0°$, the result is a straight line given by

$$n_{1pa}(T) = 2a \cos 2\theta \, R_o^2 T(1 - \exp(-2a_2))/2a_2, \tag{28}$$

where $a_2 = \alpha_o d/\cos\theta$. The curve for $\phi_n = 0°$ in Fig. 30 is then described by [see Eq. (B24), Appendix B]

$$\eta = \exp(-2a_2)\sin^2(\pi d \cos 2\theta \, n_{1pa}(T)/\lambda \cos\theta) \tag{29}$$

for the present case. Thus, for $\phi_n = 0°$ and the corresponding exponential attenuation of the grating modulation amplitude, the diffraction

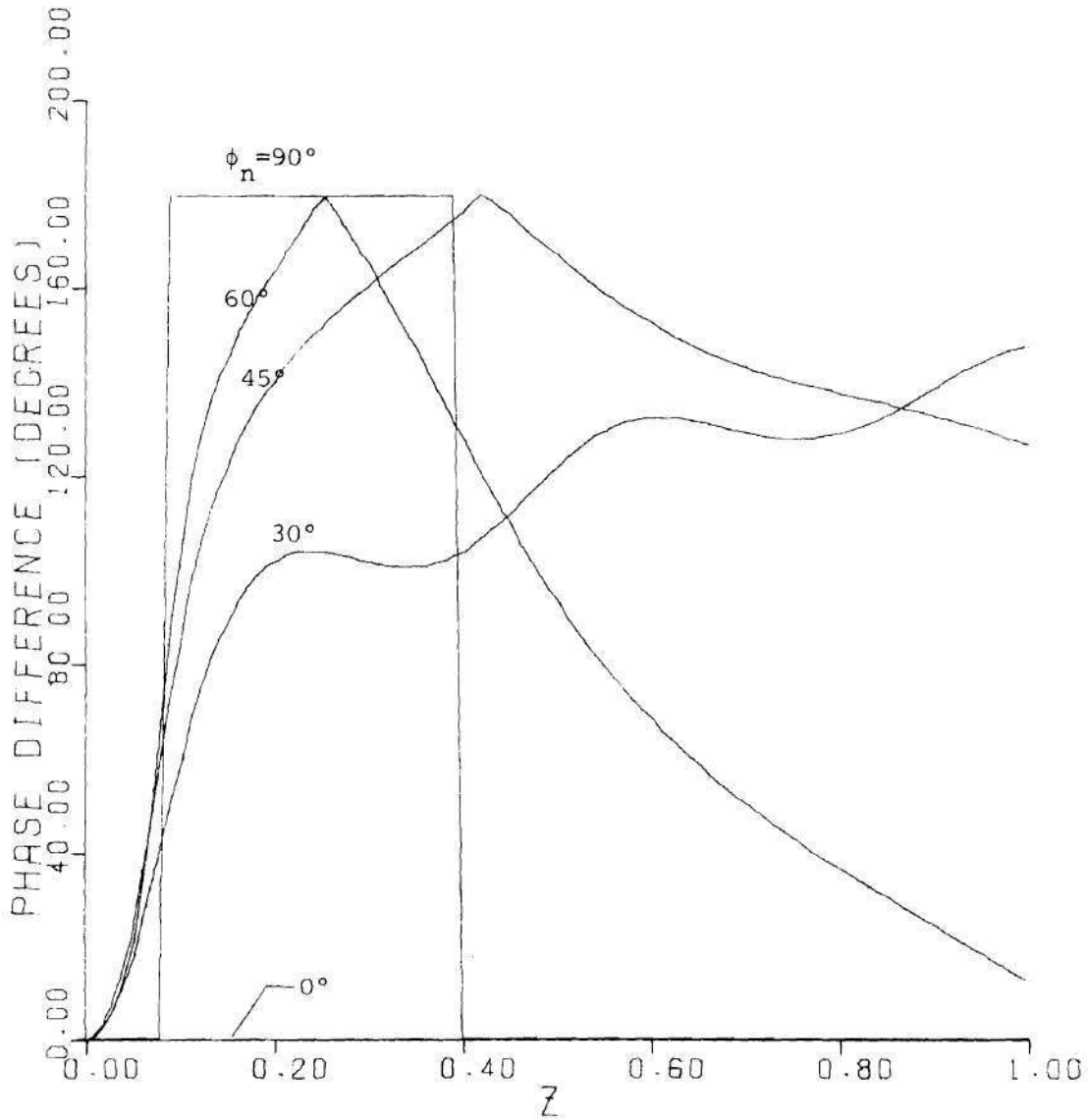

Figure 41. Calculated Phase Differences of the Writing Waves Corresponding to the Holograms of Figure 30. T = 50 sec.

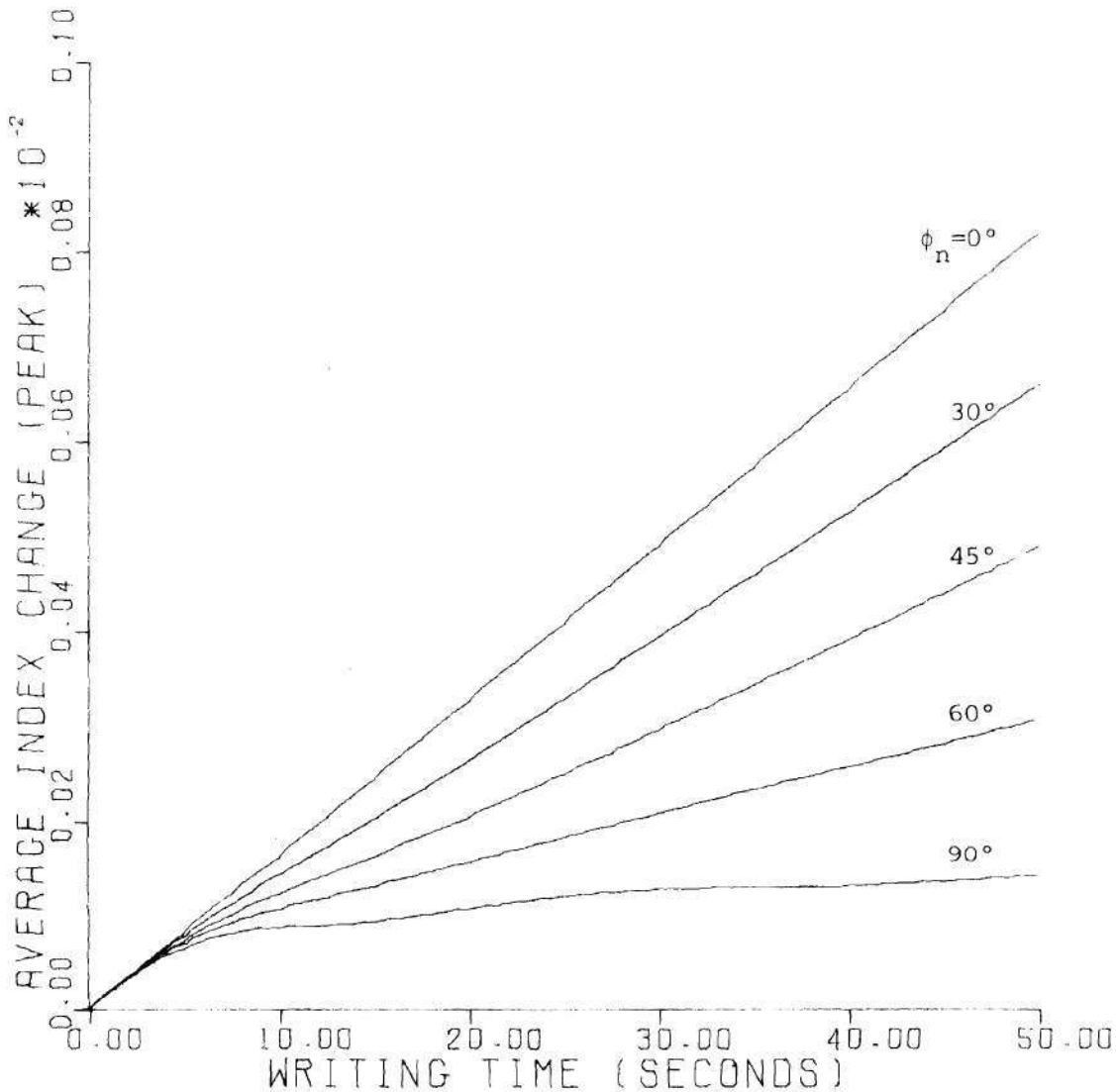

Figure 42. Calculated Time-Variations of the Thickness Average of the Grating Peak Amplitudes Corresponding to the Holograms of Figure 30.

efficiency depends on the (effective) modulation averaged over the grating thickness. This is consistent with the conclusions of Kermisch[25] who studied exponentially attenuated gratings such as produced by absorption only. As tested numerically for $\phi_n = 90°$, a similar formula for the diffraction efficiency is valid but with n_{1pa} replaced by the corresponding thickness average of the index of refraction along the x-cut considered in Chapter II. Of course, for $\phi_n = 0°$, this average is the same both along the cut and along the peak because no grating bending takes place. For the phase shifts $0° < \phi_n < 90°$, no similar results appear to hold, hinting that such relations are associated with unbent gratings. This is further supported by the fact that for $R_o \neq S_o$, in which case the gratings bend for all $\phi_n \neq 90°$, such a relation holds only if $\phi_n = 90°$ for which grating phase reversals may occur but no bending. From Fig. 42, it is also noticed that the averaged modulation amplitudes for all ϕ_n are approximately equal to about T = 5 seconds. At this time, the grating nonuniformities become appreciable and the curves separate.

Figure 43 shows the temporal variation of the irradiances RR* and SS* at the output plane (transmitted beams). Beam coupling increases with ϕ_n. Such behavior is readily externally measurable. This can be used to determine the value of ϕ_n for a given crystal and experimental situation. This measurement is simpler than a measurement of writing diffraction efficiency from which the value of ϕ_n can also be deduced. Transmission measurement is also a more reliable determinant of ϕ_n as the salient features are uncovered more readily and are more easily interpreted than with a diffraction efficiency measurement (compare

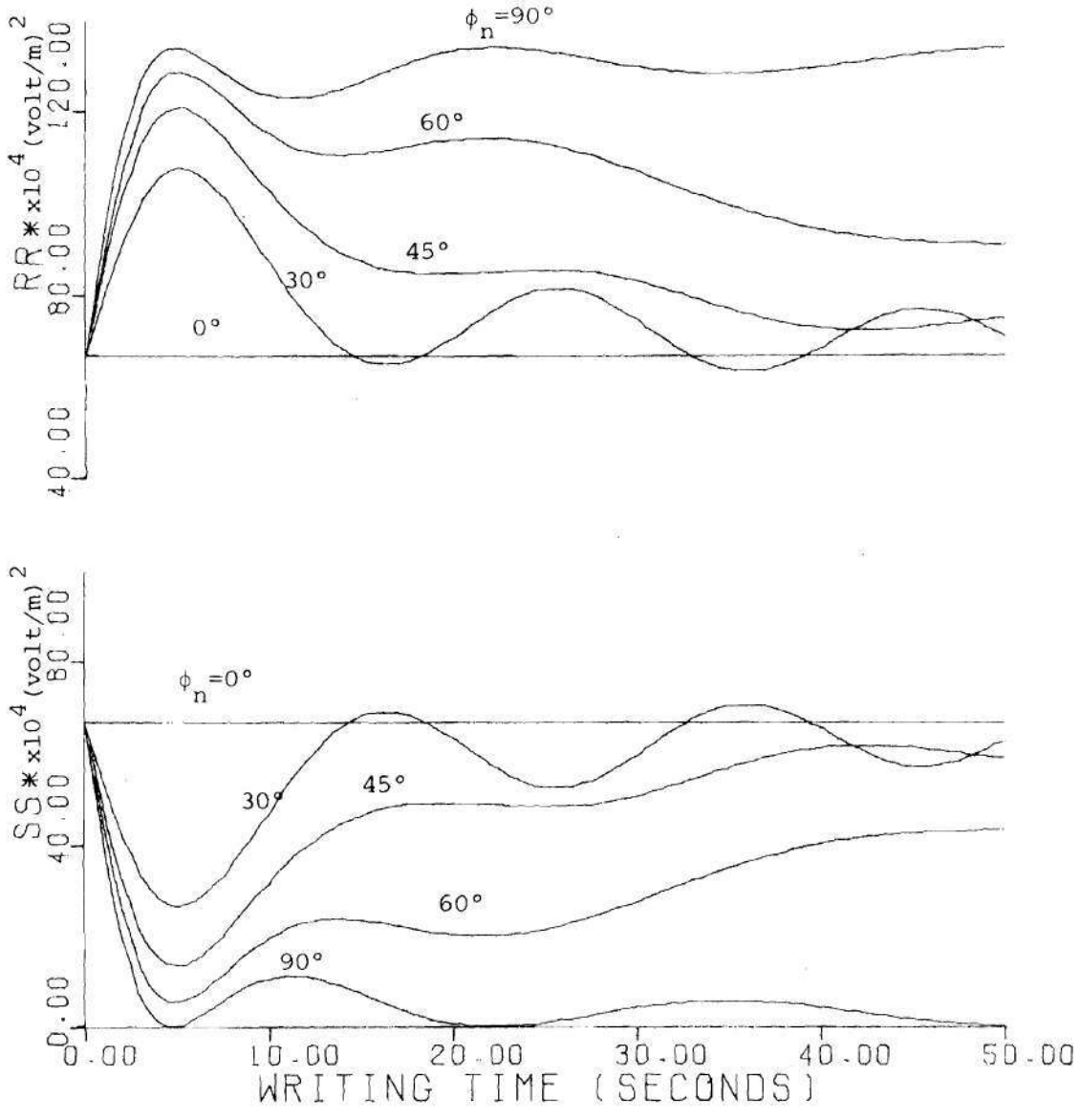

Figure 43. Calculated Temporal Variations of the Transmitted Waves (Z=1) Corresponding to the Holograms of Figure 30.

Fig. 30).

Finally, Fig. 44 gives the phase differences of the transmitted waves as a function of writing time. For $\phi_n = 0°$, the phase difference is zero as in Fig. 41. For $\phi_n = 90°$, the jump to 180° corresponds, again, to a sign-reversal of the S amplitude (see Fig. 43). The phase difference of the transmitted waves is externally measurable via interferometric techniques.

4.4 Angular Selectivity of Typical Holograms

Angular selectivity (reading) characteristics refer to the functional dependence of the diffraction efficiency on the angular deviation (of the readout wave) from the Bragg angle (defined here as $\theta' - \theta$). This section deals with the angular selectivity characteristics of the typical holograms whose writing characteristics are displayed in Fig. 30. For a given phase shift, ϕ_n, the angular selectivity characteristics are presented at selected (writing) times that correspond to an interesting location on the writing characteristic. Accordingly, the time values chosen correspond to diffraction efficiency at one-half maximum, at the first maximum, and at the first minimum on the writing characteristics. Consideration is also given to the relevant grating peak amplitudes and the associated grating phases.

Figure 45 illustrates the temporal development of the angular selectivity characteristic for $\phi_n = 0°$ and Fig. 46 shows the corresponding grating modulation amplitude at the selected time values. As the grating nonuniformity (entirely due to absorption in this case) increases, the pattern nulls become less pronounced. However, for this

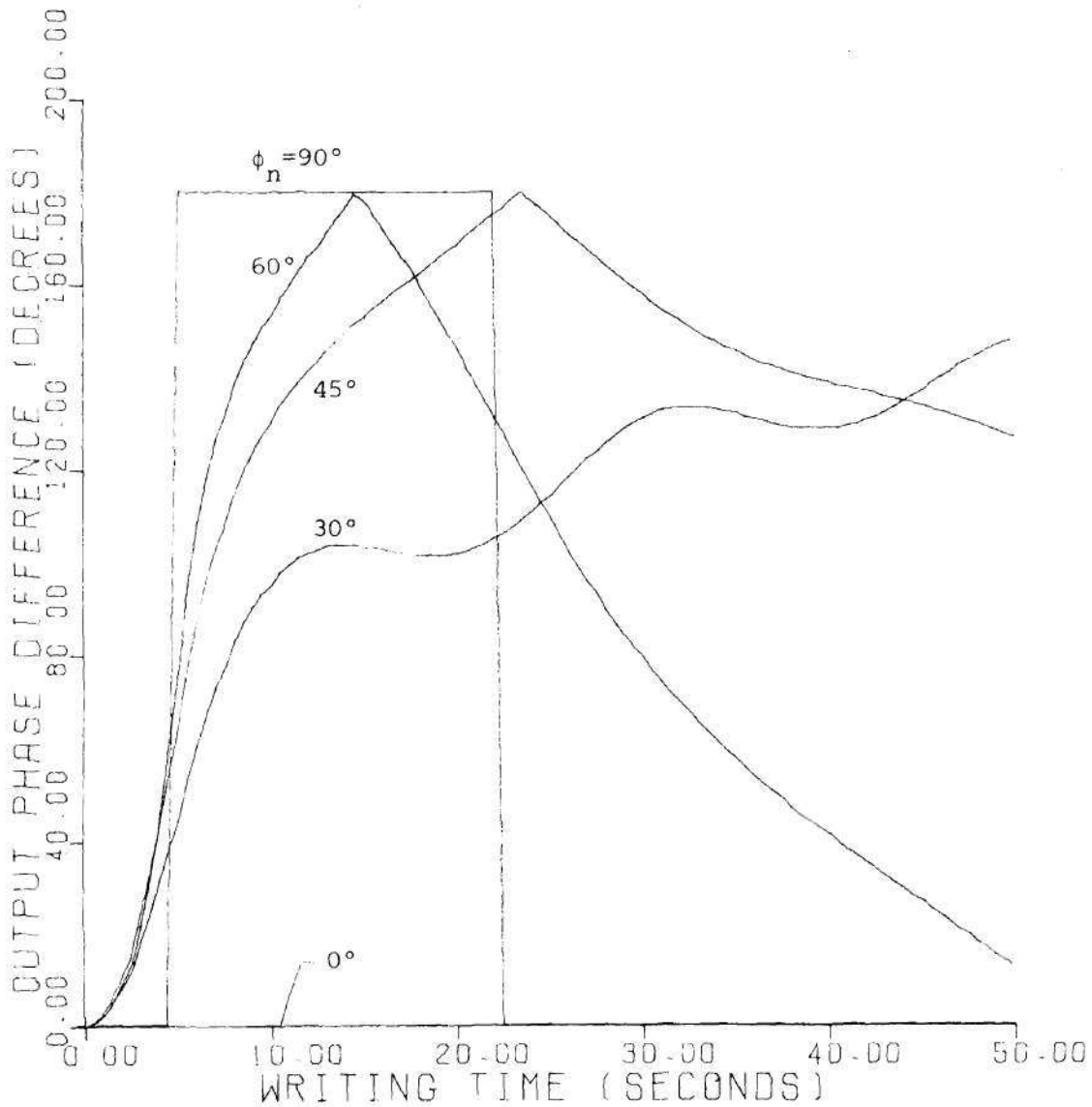

Figure 44. Calculated Temporal Variations of the Phase Differences of the Transmitted Waves of Figure 43.

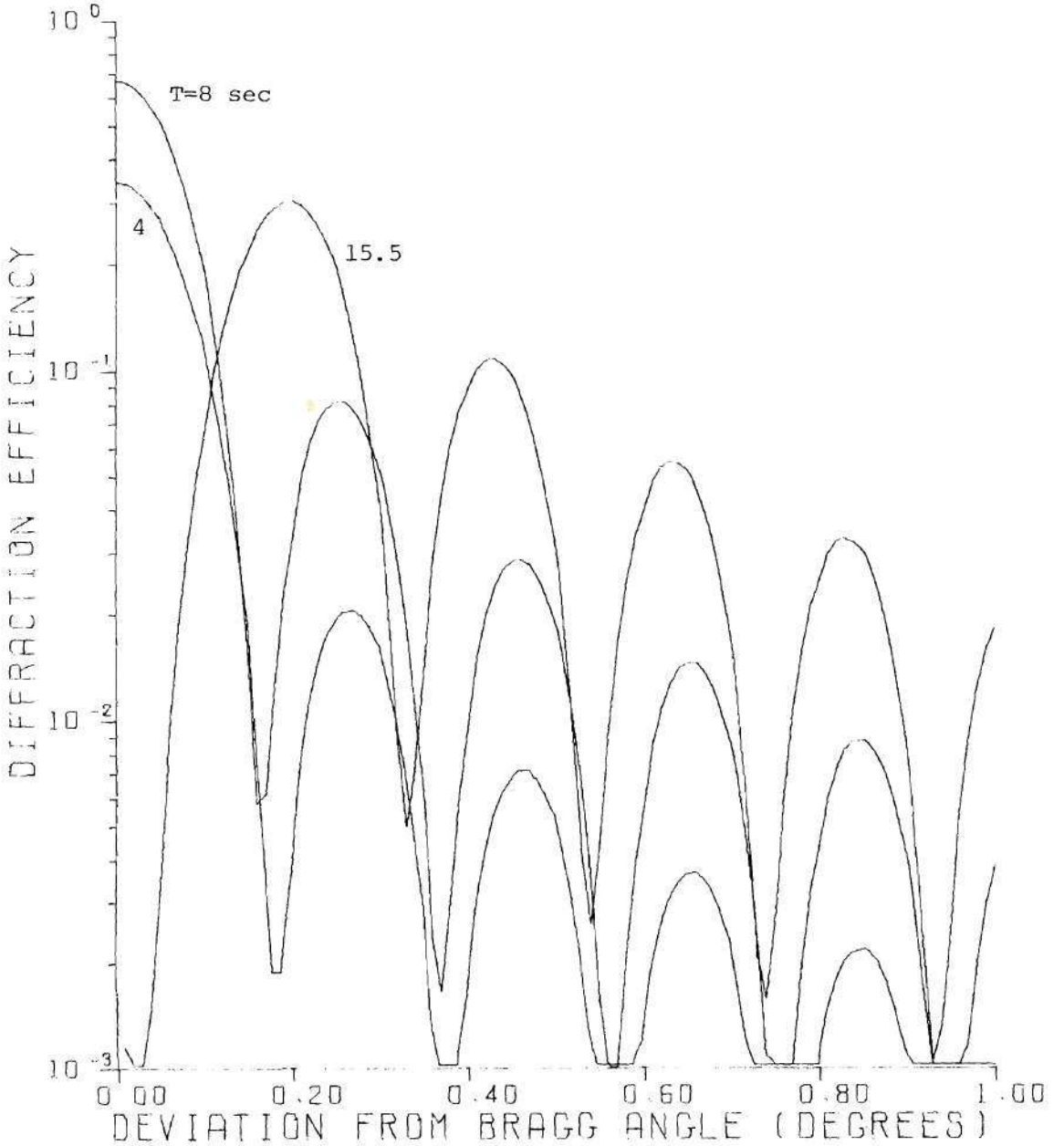

Figure 45. Calculated Temporal Evolution of the Angular Selectivity Characteristic Corresponding to the Hologram with $\phi_n = 0$ in Figure 30.

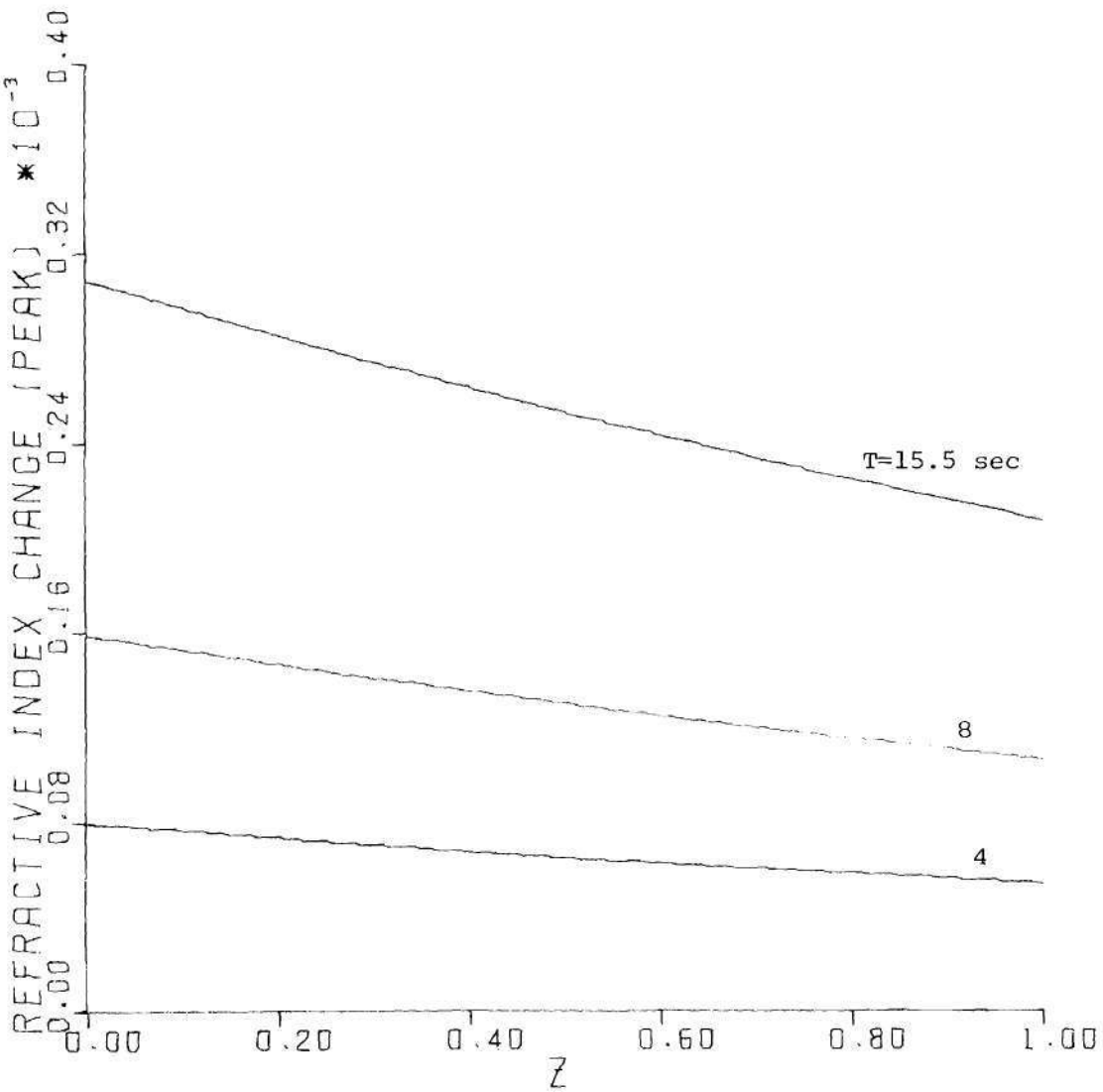

Figure 46. Calculated Temporal Evolution of the Grating Peak Amplitude Corresponding to Figure 45.

particular example, this effect is not strong due to the relative uniformity of the grating. It is seen in Fig. 45 (and in Fig. 30) that the diffracted power can be zero on the Bragg angle. In this case, pronounced sidelobes develop. The patterns of Fig. 45 are symmetric with respect to the Bragg angle and, thus, identical patterns are produced for negative deviations. As usual for $\phi_n = 0°$, the gratings do not bend.

Figure 47 shows the time-evolution of the angular selectivity characteristic for $\phi_n = 45°$. The noteworthy feature is that the characteristic is no longer symmetric. For T = 9.5 sec, the central maximum is displaced slightly from the Bragg angle. Comparing Figs. 47 and 48 indicates that the sidelobes become increasingly less distinct with increasing grating nonuniformity which is a general rule. Figure 49 shows the phases for the gratings under discussion.

In Fig. 50, the case of $\phi_n = 90°$ is presented. The multiple angular selectivity sidelobes disappear as a result of the grating nonuniformity as depicted in Fig. 51. For T = 11 sec, the grating amplitude is zero at the output face of the crystal. For T = 34.5 sec, the nonuniformity is even more pronounced with a grating phase reversal occurring. The patterns of Fig. 50 are symmetric relative to the Bragg angle. Note the increase in the width of the central lobe at T = 11 sec. This is consistent with the fact that, in general, thinner diffracting structures have broader lobes. Since the gratings for $\phi_n = 90°$ do not bend, it is concluded that the asymmetry observed in Fig. 47 is due to the bending of the corresponding gratings alone (as opposed to being

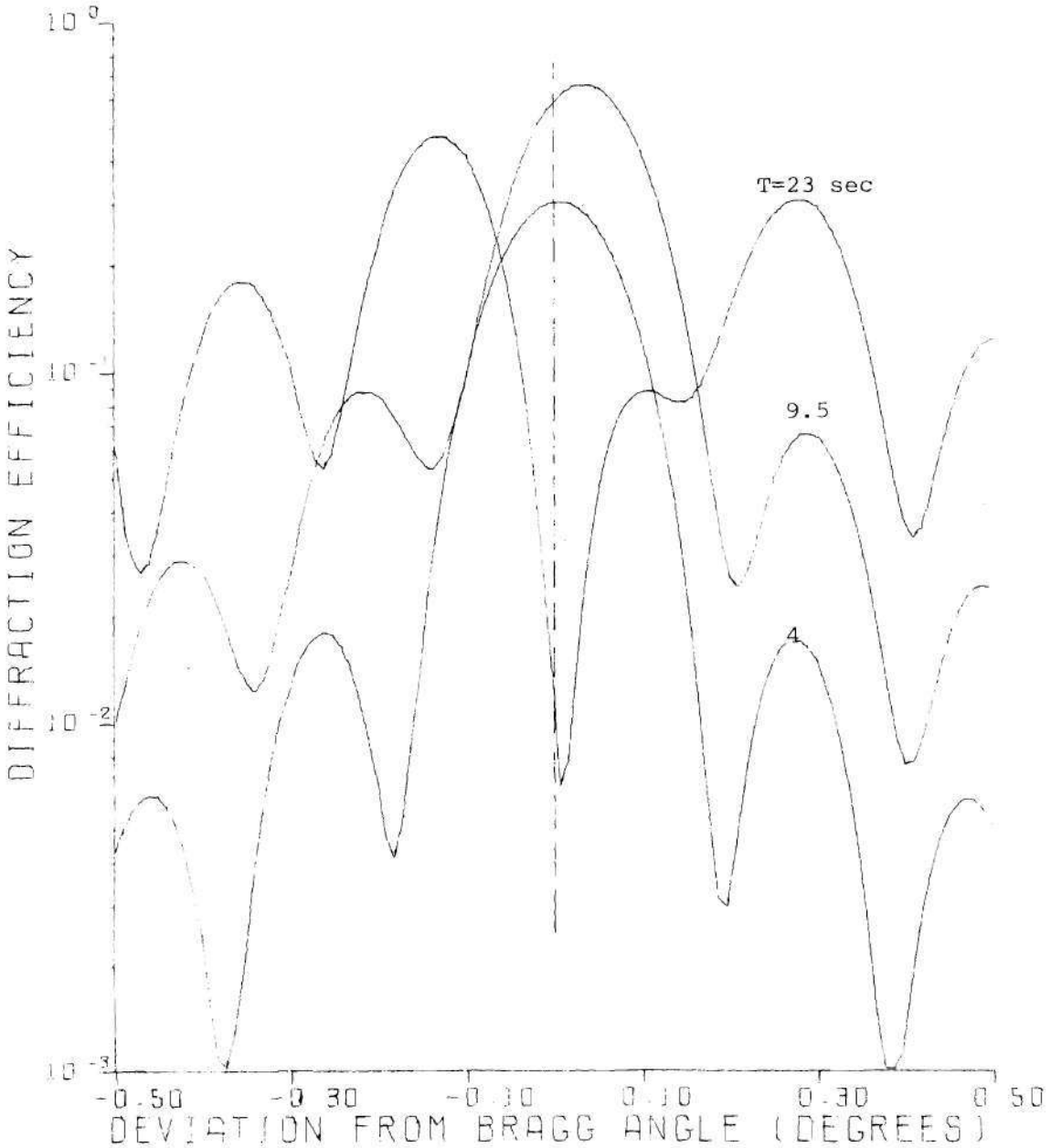

Figure 47. Calculated Temporal Evolution of the Angular Selectivity Characteristic Corresponding to the Hologram with $\phi_n = 45°$ in Figure 30. Vertical Dashed Line Indicates Position of Bragg Angle.

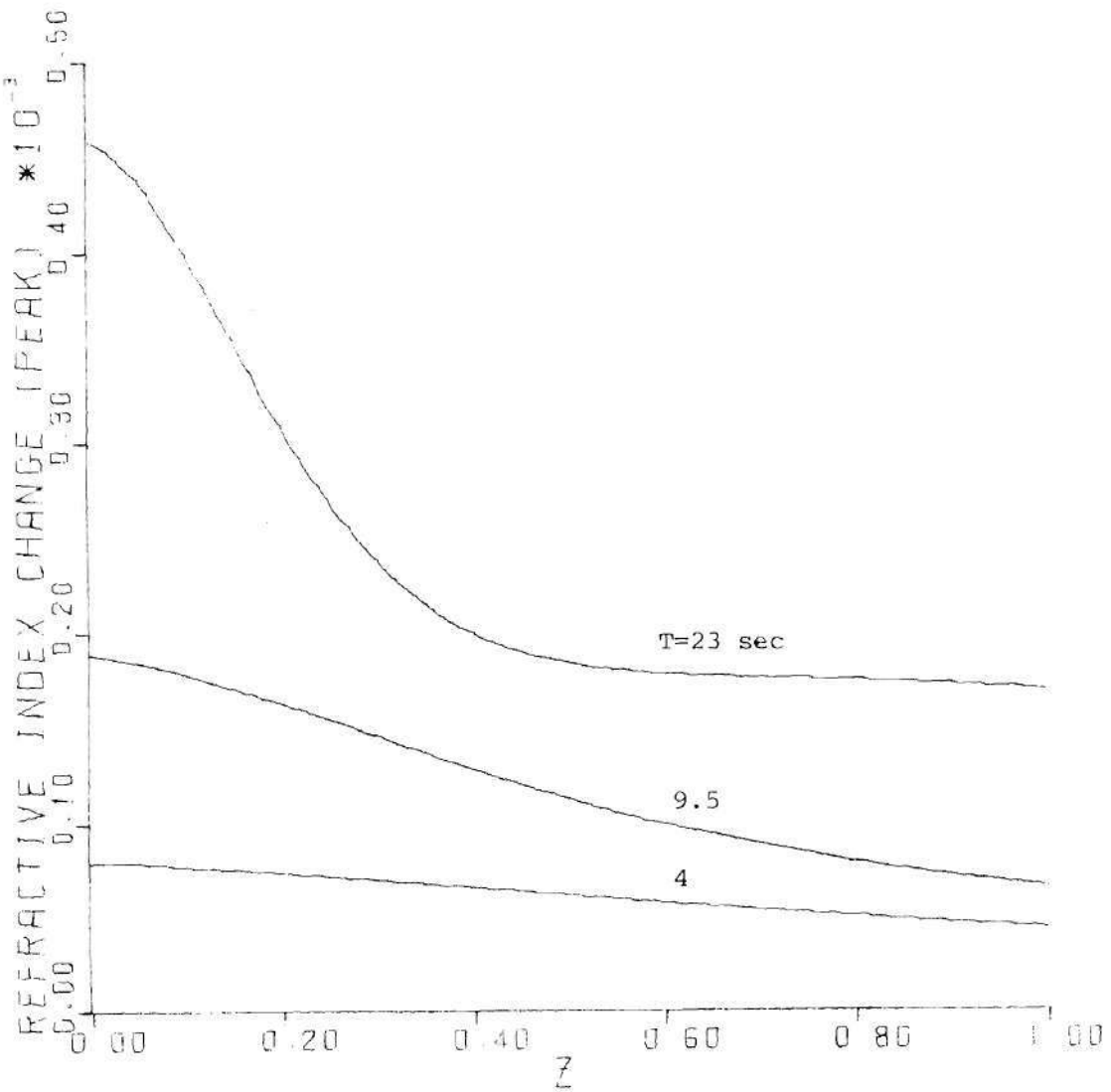

Figure 48. Calculated Temporal Evolution of the Grating Peak Amplitude Corresponding to Figure 47.

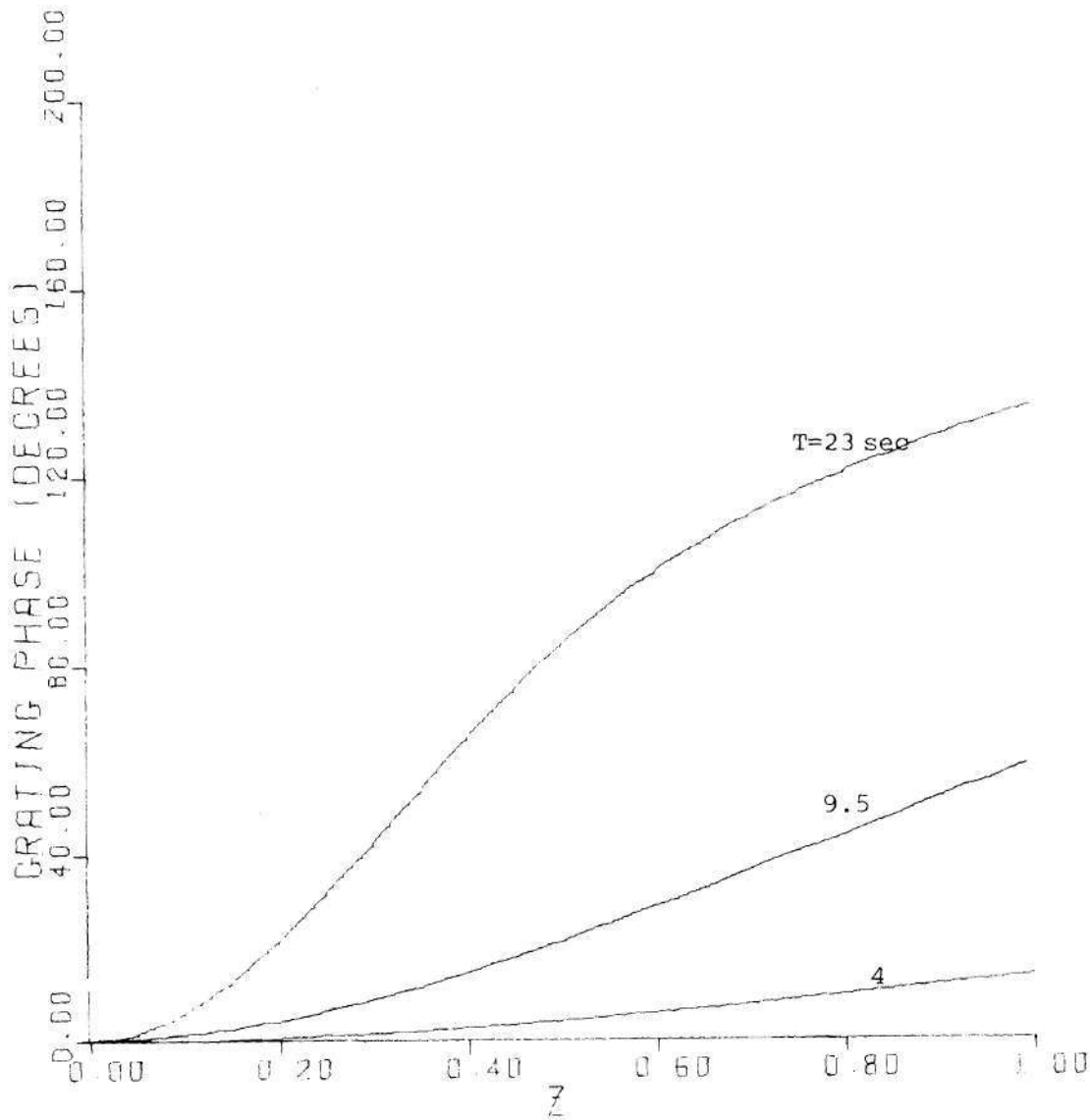

Figure 49. Calculated Temporal Evolution of the Grating Phase Associated with the Grating Peak Amplitudes of Figure 48.

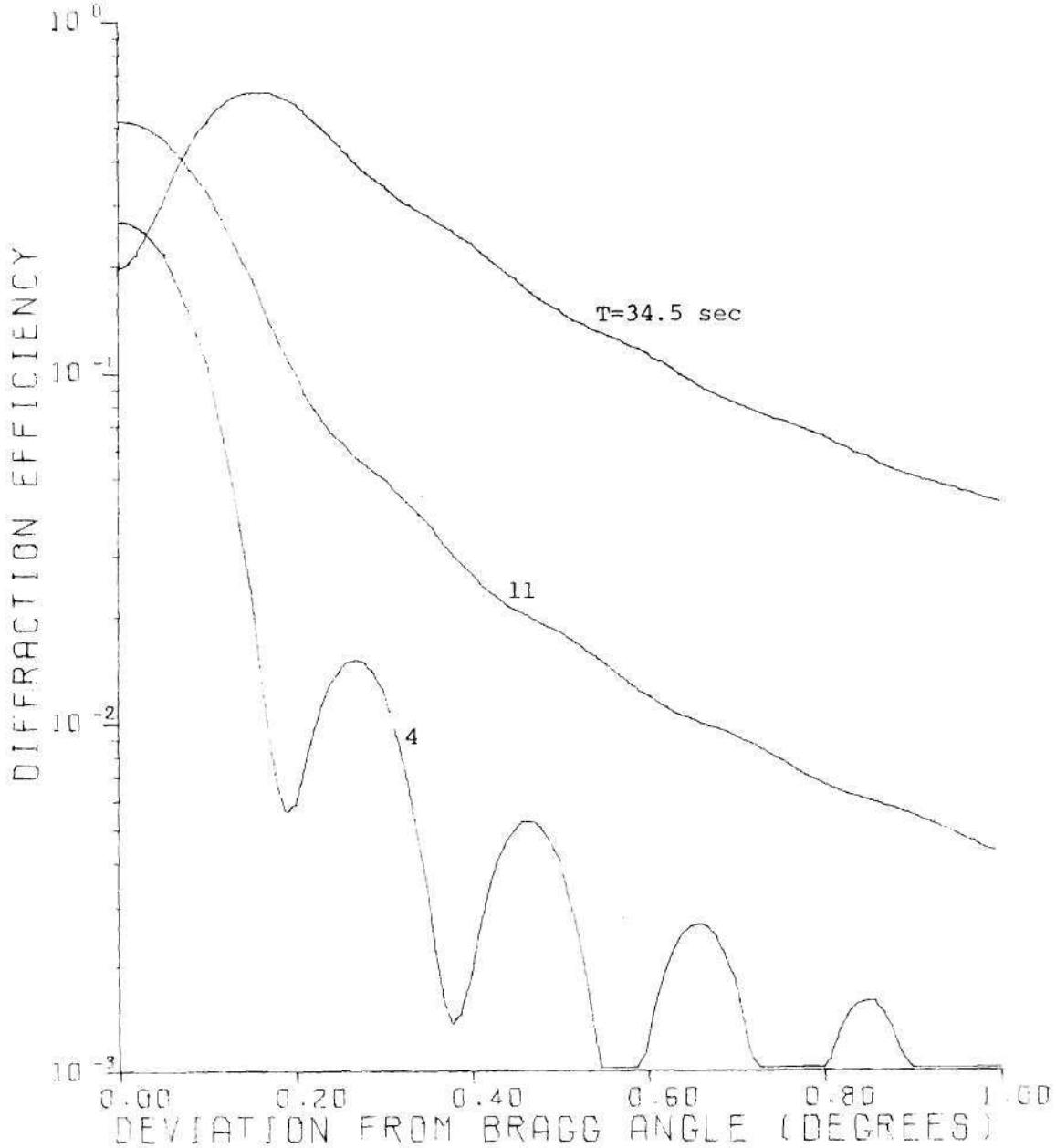

Figure 50. Calculated Temporal Evolution of the Angular Selectivity Characteristic Corresponding to the Hologram with $\phi_n = 90°$ in Figure 30.

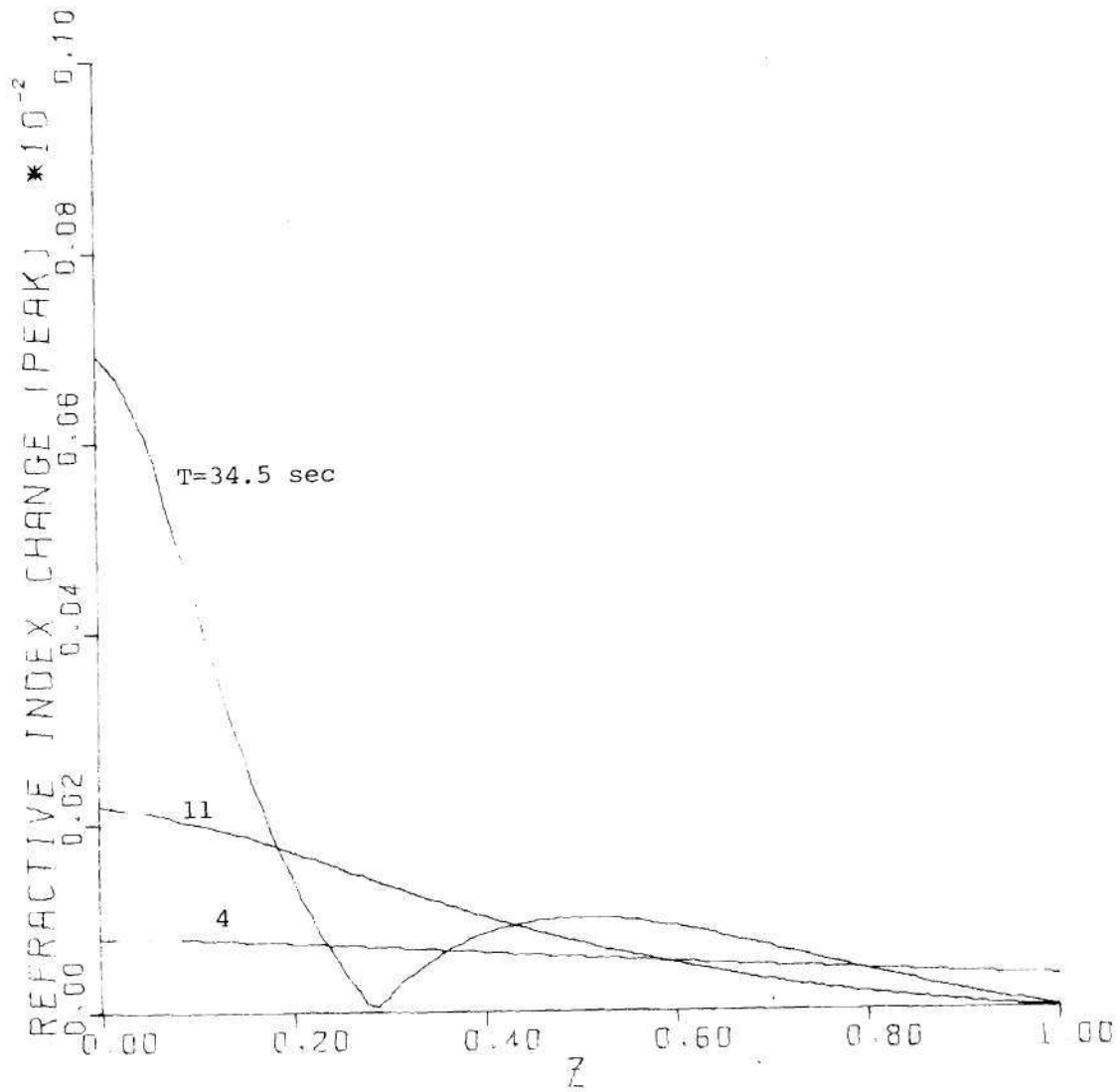

Figure 51. Calculated Temporal Evolution of the Grating Peak Amplitude Corresponding to Figure 50.

due to the nonuniformity). Indeed, as seen from Figs. 47 and 49, the asymmetry is more pronounced for larger bending.

As a final example, the angular selectivity characteristics corresponding to the gratings of Figs. 38 and 39 are given in Fig. 52 for phase shifts $0° < \phi_n < 90°$ which is the probable practical situation. Clearly, asymmetric angular selectivity characteristics are the rule rather than the exception and are to be expected at least for high-exposure high-efficiency thick holographic gratings.

In summary, examples of the angular selectivity characteristics of typical holograms have been given and their general features correlated to structural aspects of the corresponding refractive index gratings. It has been shown that sidelobe obliteration is due to the nonuniformity of the grating modulation amplitude and that the asymmetry is due to grating bending.

4.5 Dynamic Readout of Typical Holograms

Readout of a holographic grating may be regarded as a special case of writing in which one of the writing boundary conditions, R_o or S_o, is set to zero. Thus, a single, relatively strong wave is incident upon the hologram. However, as previously pointed out, there are still two waves in the grating, namely the transmitted component of the incident wave and its diffracted component. These two waves can interact to form (write) a new grating which leads to a continuous modification of the total grating structure and of the corresponding diffraction efficiency (readout) characteristics. The total grating structure thus created, however, is still necessarily sinusoidal as in the case of

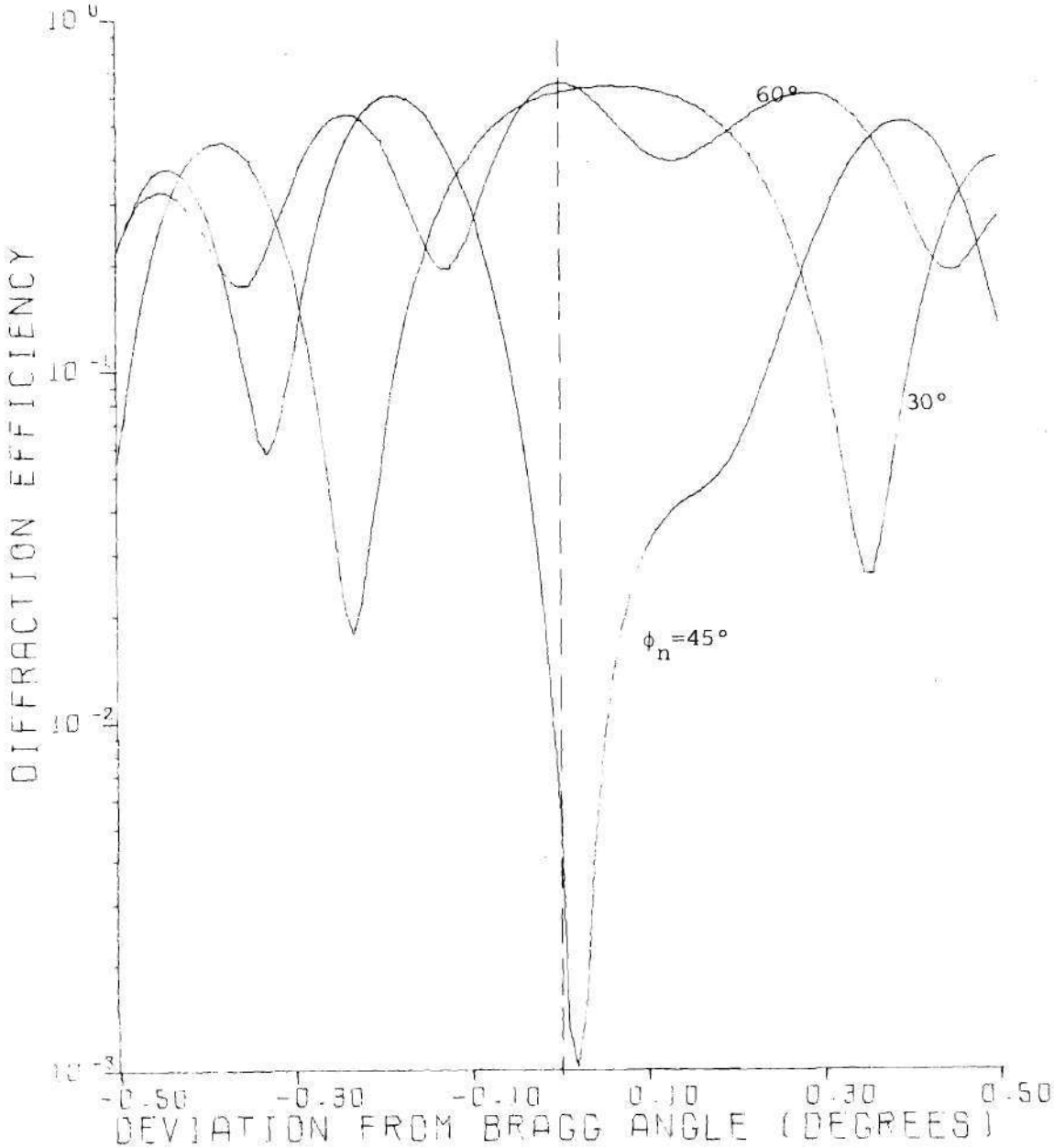

Figure 52. Calculated Angular Selectivity Characteristics Corresponding to the Gratings of Figures 38 and 39. T = 50 sec. Vertical Dashed Line Indicates Position of Bragg Angle.

writing.

In this section, the dynamic readout (as opposed to static readout such as angular selectivity during which no changes are produced in the hologram structure) of the typical holograms whose characteristics are presented in Fig. 30 is discussed. The readout behavior is found to be very sensitive to the exposure (i.e. writing time T in Fig. 30) used to produce the hologram to be read. This is because the previous exposure determines the initial readout diffraction efficiency of the hologram and, thus, affects the internal intensity ratio, ψ, of the transmitted and diffracted waves which in turn influences the effectiveness with which these waves form the new grating (i.e. modify the total grating). In addition, the readout characteristics are strongly influenced by which of the two waves (R wave or S wave) is applied. It is found that R wave readout commonly produces erasure (decrease of diffraction efficiency) and that S wave readout commonly produces enhancement (increase of diffraction efficiency). Exceptions to this are indicated later in this section. As discussed in Chapter III, such behavior has indeed been observed experimentally and studied to some extent.[20,39,48]

Before embarking on the discussion of the calculated results, it may be appropriate to present an intuitive physical explanation of the erasure-enhancement phenomenon since it may, at first, seem puzzling that a mere change in the direction of the readout wave can account for such behavior. The fundamental reason for these effects lies in the nonexplicit assumption of the dynamic theory as applied here that the material of interest is anisotropic (for example, lithium niobate has a crystalline polar axis of a definite polarity; see Appendix D).

This is mathematically represented by constraints on the parameter ϕ_n, that is $0° \leq \phi_n \leq 90°$. Thus, the phase shift between the hologram-forming light interference pattern and the resulting refractive index grating, ϕ_n, is of a single sign. This means that the grating is always shifted in the same direction relative to the crystal axes for a given interference pattern. The dynamic coupled-wave equations [Eqs. (9) and (10)] are not symmetric upon R-S interchange unless $\phi_n \rightarrow -\phi_n$ simultaneously. Therefore, reading with the R wave does not give the same results as S readout. However, if the dynamic theory is used to describe hologram storage in an isotropic medium, the transition $\phi_n \rightarrow -\phi_n$ must accompany R-S interchange since identical behavior must occur for R readout and S readout.

To explain how maintaining a single sign for ϕ_n accounts for the observed differences in the readout characteristics presently under discussion, it is helpful to examine the readout of a low-exposure hologram (short writing time, T) as considered in Appendix B, using the dynamic coupled-wave formalism. From the solutions of the writing equations given there [Eqs. (B11) and (B12)], it is easily shown [using Eq. (A7)] that the resulting grating is of the form cos kx (multiplicative z-dependent coefficients are omitted). Readout (R or S) of this grating is then accomplished by solving the governing equations again using the appropriate boundary conditions. The complex wave amplitudes, R and S, can thus be found (see Appendix B) for R readout and S readout. The interference patterns $(\bar{E} \cdot \bar{E}^*)$ produced in each case are then calculated by constructing $\bar{E} = R\hat{r} \exp(-j\bar{\rho}\cdot\bar{r}) + S\hat{s} \exp(-j\bar{\sigma}\cdot\bar{r})$, which is the total electric field in the grating as given by Eq. (8). The

interference pattern produced upon R readout is thus found to be $I_{rr} \propto -\sin kx$ and that for S readout $I_{ss} \propto \sin kx$. The relative positions of these patterns and the original grating are indicated in Fig. 53(a). The position of the (new) grating resulting from these interference patterns depends on the value of ϕ_n. Suppose, for example, $\phi_n = 90°$. Then, the new grating Δn_{rr} due to I_{rr} would be $\Delta n_{rr} \propto -\sin(kx + \phi_n) = -\sin(kx + 90°) = -\cos kx$, which is 180° out of phase with the original (cos kx) grating [see Fig. 53(b)]. The superposition of these two gratings, therefore, causes reduction in total grating amplitude and a corresponding drop in diffraction efficiency; that is erasure. On the other hand, for S readout with $\phi_n = 90°$, the grating due to I_{ss} is $\Delta n_{ss} \propto \sin(kx + \phi_n) = \sin(kx + 90°) = \cos kx$ which is in phase with the original grating yielding constructive superposition and corresponding enhancement as shown in Fig. 53(b). Note that if ϕ_n is set to -90°, $\Delta n_{ss} \propto -\cos kx$ as is Δn_{rr} (isotropic case). From Fig. 53 it is seen that for S readout the strongest enhancement occurs for $\phi_n = 90°$ and decreases with decreasing ϕ_n. For R readout, maximum erasure is expected for $\phi_n = 90°$ with decreasing rate of erasure as ϕ_n decreases. For $\phi_n = 0°$, the actions of R and S readout are identical. In this instance, the dynamic coupled-wave equations are unaffected by R-S interchange. The ±90° phase difference between Δn and I_{ss} and I_{rr} is a natural result of the usual 90° phase difference between an incident wave and its diffracted wave that occurs in coupled-wave (phase hologram) studies.[7,20]

It must be noted that the above arguments are strictly valid only for the early stages of the hologram since it is clear from Figs. 30 and 42 that a drop in diffraction efficiency can accompany increased

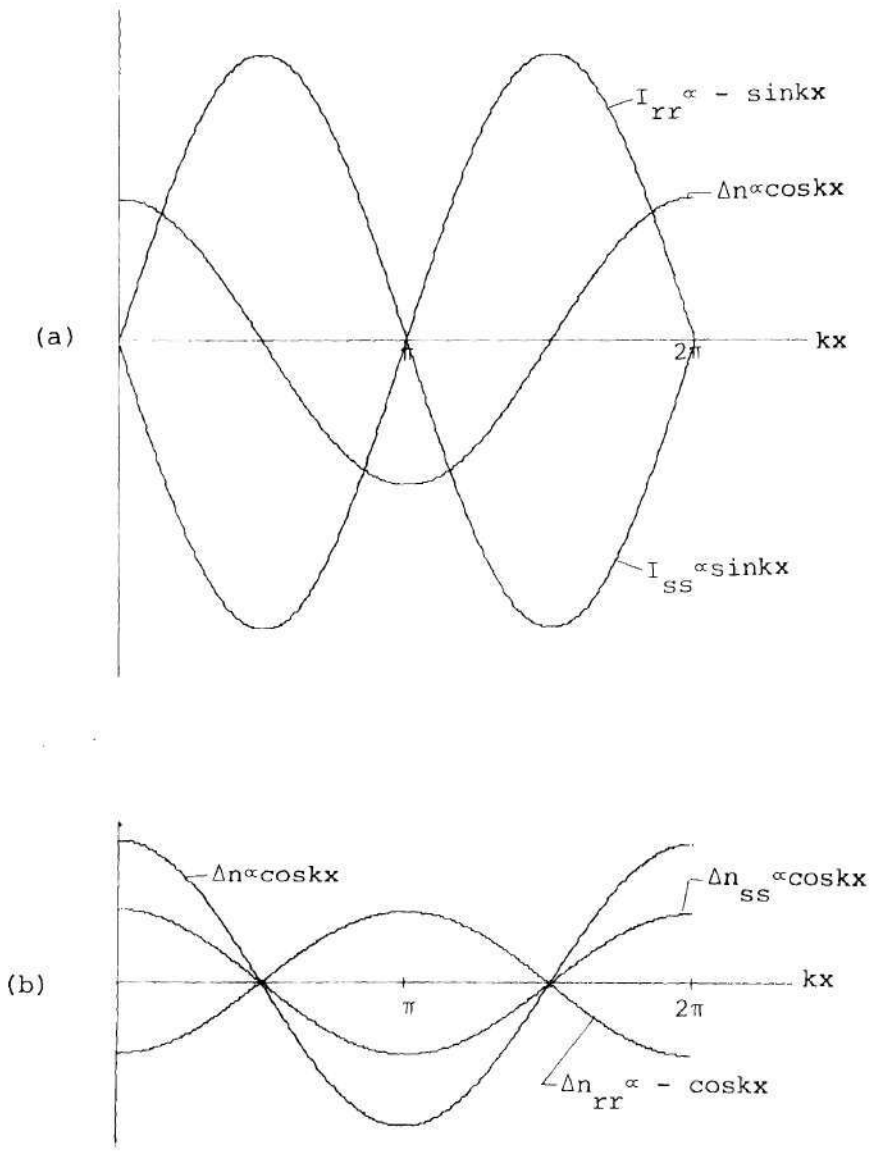

Figure 53. Schematic Explanation of the Erasure-Enhancement Phenomenon. (a) Relative Positions of the Original Grating and the Readout Light Interference Patterns. (b) Relative Grating Positions for $\phi_n = 90°$.

grating amplitude on writing. However, these arguments which are based on ideas by Staebler and Amodei[20] have served to illustrate the basic reasons why R readout may give results different from S wave readout.

The results presented in what follows are calculated under the assumption that the value of ϕ_n is the same for writing and readout. This is a reasonable assumption if the experimental conditions do not vary between writing and readout. The initial reading time (T'=0) for each ϕ_n corresponds to diffraction efficiency at one-half first maximum, at the first maximum, and at the first minimum in Fig. 30. The calculations of Sec. 4.4 also correspond to these values of writing time.

Figures 54 and 55 illustrate R and S readout at one-half maximum diffraction efficiency. At least initially, the behavior is consistent with the explanations set forth above. That is, $\phi_n = 90°$ corresponds to the fastest erasure and enhancement for R and S readout, respectively. For $\phi_n = 0°$, identical solutions are obtained. Note that for $\phi_n = 90°$ in Fig. 55, the maximum diffraction efficiency is $\exp(-2\alpha_o' d/\cos\theta')$ which is in agreement with the conclusions of Sec. 4.2. For $\phi_n = 0°$, the initial slope is zero. For the other phase shifts, the initial slopes for R readout and S readout are approximately equal and opposite.

Figures 56 and 57 are calculated with reading time T'=0 at the diffraction efficiency maxima of Fig. 30. In these figures, erasure occurs for $\phi_n = 0°$. This is because at T'=0, the efficiency is already at the theoretical maximum $\exp(-2\alpha_o' d/\cos\theta')$. In the previous two figures, enhancement occurred for $\phi_n = 0°$. The approximate slope symmetry still prevails although to a somewhat lesser extent than before. Erasure appears to take place slightly faster than enhancement.

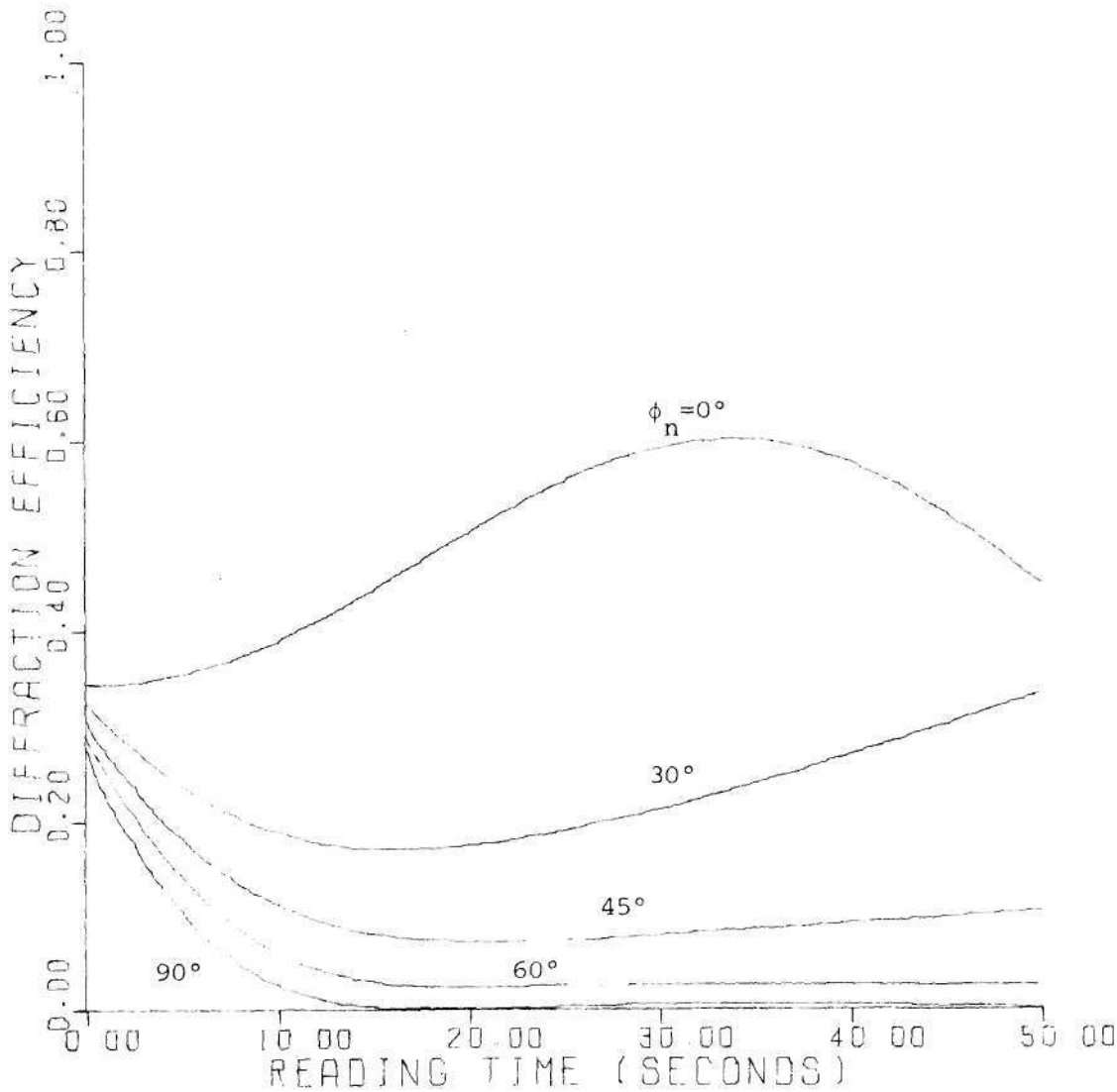

Figure 54. Calculated Readout Characteristics Corresponding to Initial (T'=0) Diffraction Efficiency at One-Half First Maxima in Figure 30. R_o' = 1000 volt/m and S_o' = 0.

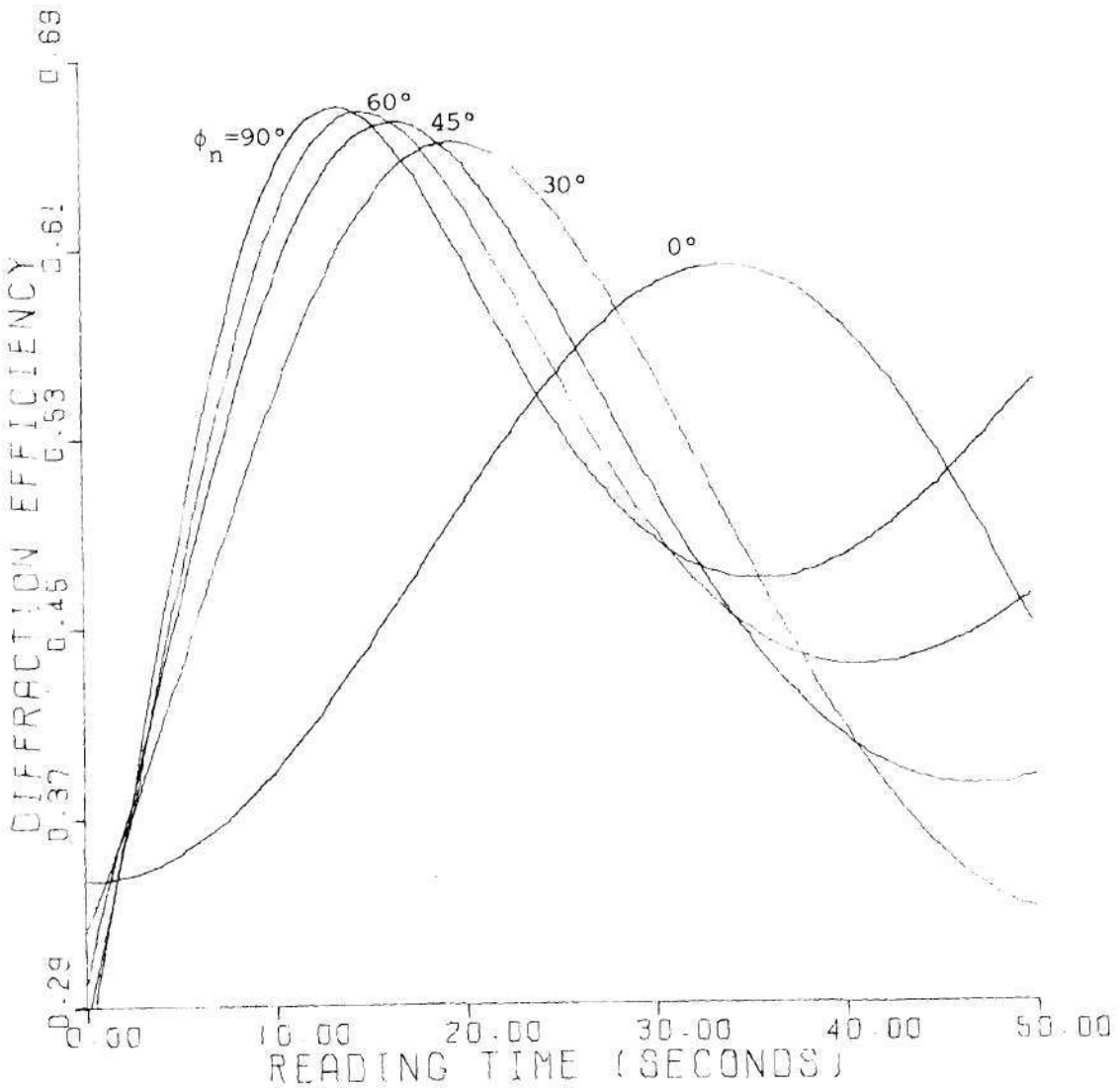

Figure 55. Calculated Readout Characteristics Corresponding to Initial (T'=0) Diffraction Efficiency at One-Half First Maxima in Figure 30. R'_o = 0 and S'_o = 1000 volt/m.

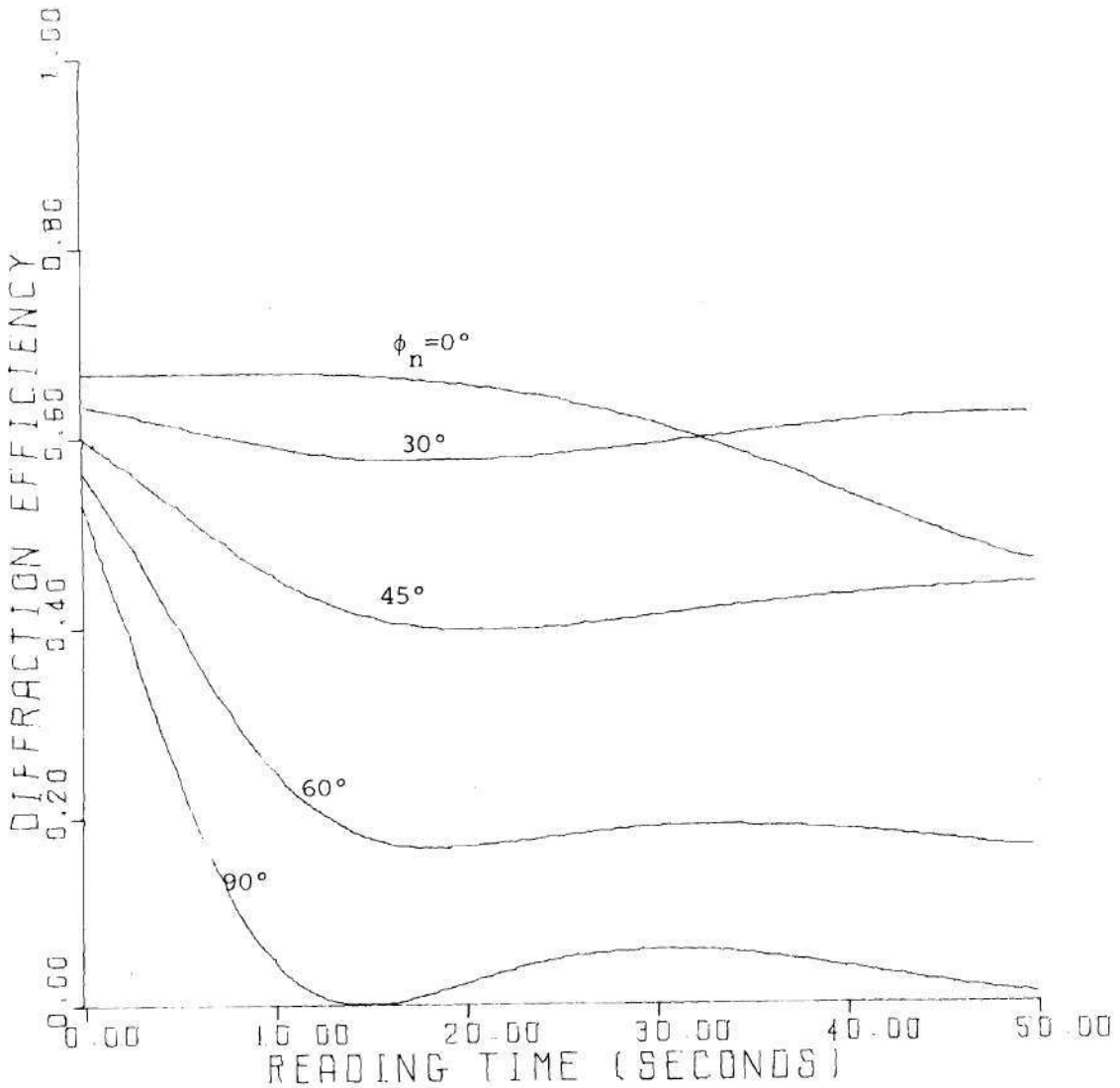

Figure 56. Calculated Readout Characteristics Corresponding to Initial Diffraction Efficiency at the First Maxima in Figure 30. R_o' = 1000 volt/m and S_o' = 0.

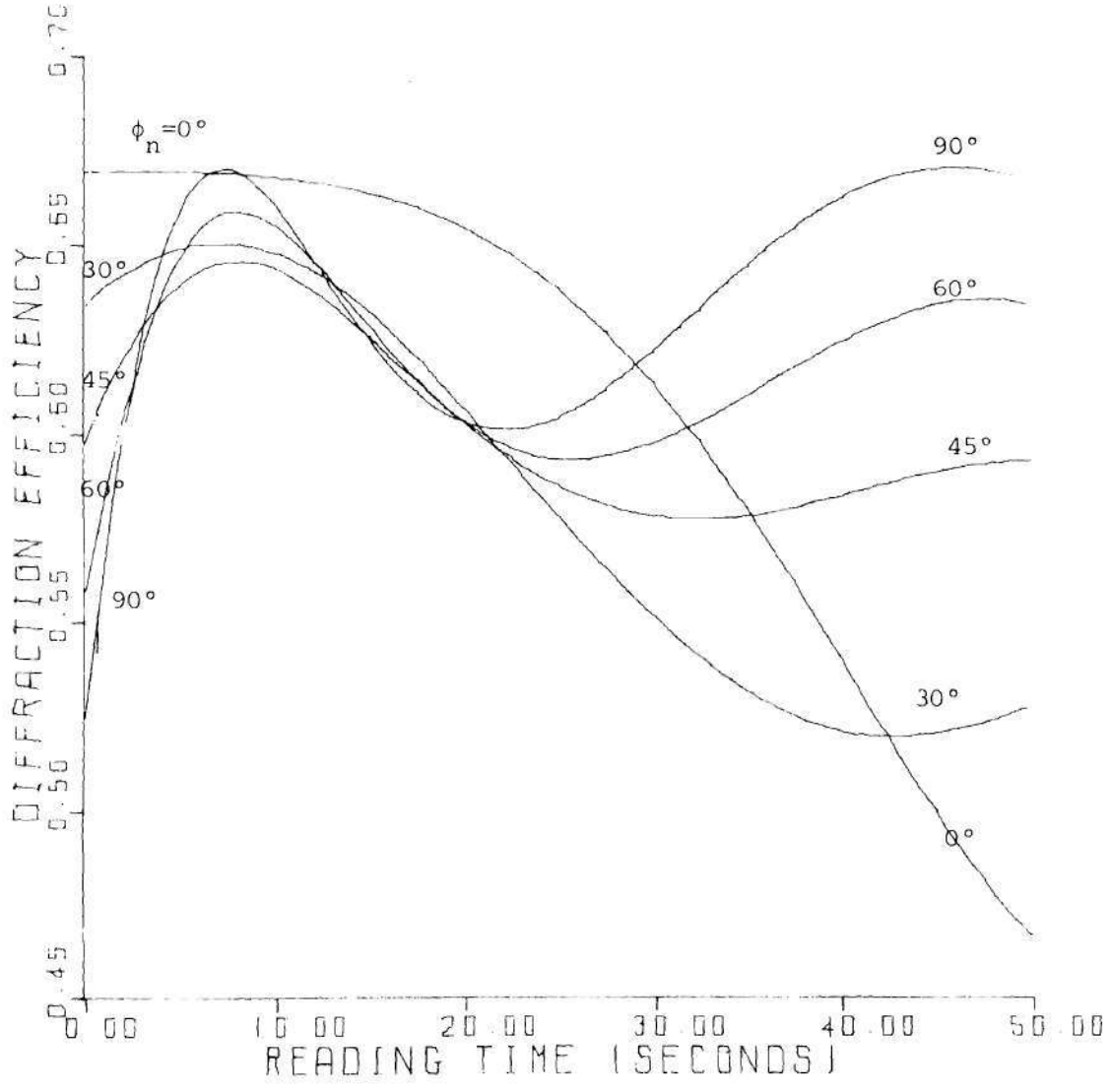

Figure 57. Calculated Readout Characteristics Corresponding to Initial Diffraction Efficiency at the First Maxima in Figure 30. $R_o' = 0$ and $S_o' = 1000$ volt/m.

Figures 58 and 59 show readout with T'=0 at the first diffraction efficiency minima of Fig. 30. In Fig. 58, the efficiency is enhanced for ϕ_n = 0°, 30°, and 45° and oscillates after erasure for ϕ_n = 60° and 90°. In Fig. 59, enhancement is observed for all ϕ_n. For ϕ_n = 90°, the diffraction efficiency reaches the theoretical maximum remaining fairly constant after that. As before, the initial slopes are approximately symmetrical but now with enhancement proceeding a little faster.

In conclusion, it is interesting to note that the above presented results can be used in determining the polarity of the c-axis of a lithium niobate crystal. As substantiated in Chapter V, it is found experimentally that the crystal must be placed with the +c axis in the +x direction in the coordinate system of Fig. 1 to obtain results consistent with the present discussion. Therefore, it is concluded that the crystal shifts the refractive index pattern in the -c direction relative to the light interference pattern that forms it. This is consistent with the results of Staebler and Amodei.[20]

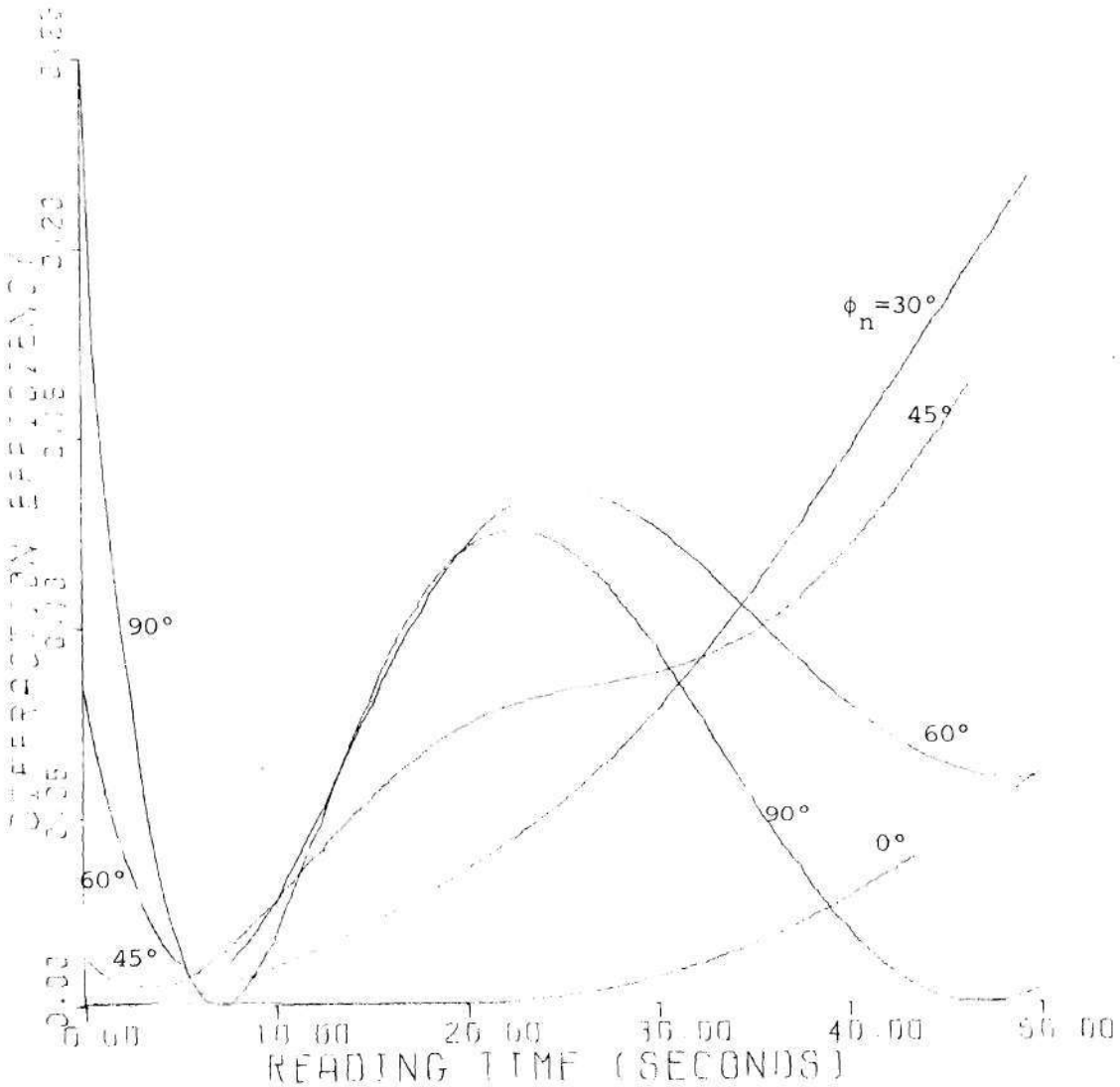

Figure 58. Calculated Readout Characteristics Corresponding to Initial Diffraction Efficiency at the First Minima in Figure 30. R_o' = 1000 volt/m and S_o' = 0.

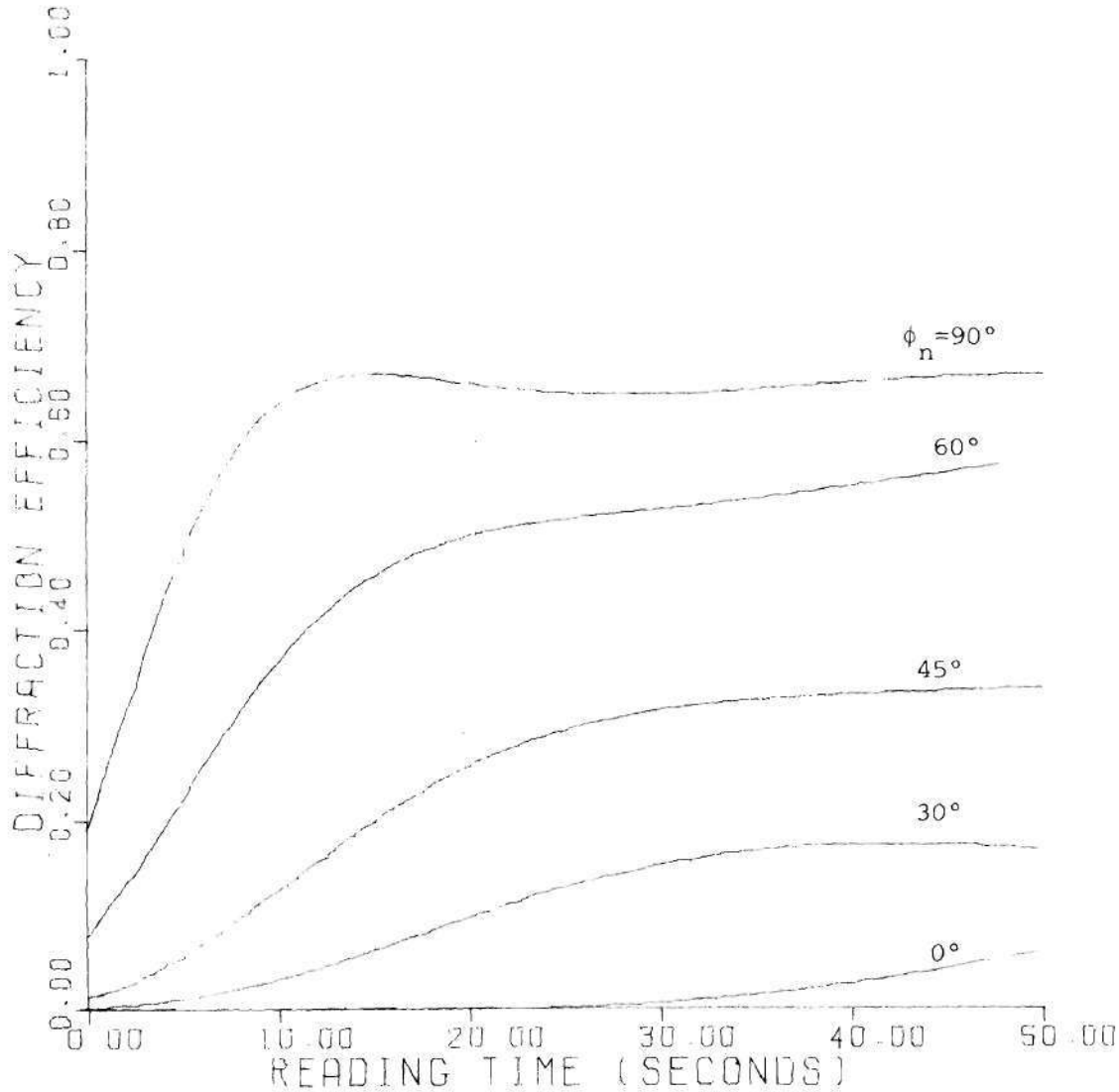

Figure 59. Calculated Readout Characteristics Corresponding to Initial Diffraction Efficiency at the First Minima in Figure 30. $R_o' = 0$ and $S_o' = 1000$ volt/m.

CHAPTER V

QUANTITATIVE THEORY-EXPERIMENT COMPARISON

5.1 Experimental System

The experimental work described in this thesis has been carried out using the system shown in Figure 60. This system is mounted on a rigid, vibration isolation optical table. The holograms are written by interfering two beams from an argon ion laser operating at λ = 0.5145 μm in a crystal of iron-doped $LiNbO_3$, approximately 2 mm thick. The angle between the incident beams (2θ) is 10° and the polarization vectors lie in the plane of incidence (E-mode). The diffraction efficiency is monitored continuously (reading) by a low-power He-Ne laser (λ = 0.6328 μm) aligned at its Bragg angle. The diffracted beam impinges on a photodetector of a conventional, optical power meter that is connected to a graphical recording device, yielding a plot of the diffracted power vs. time.

When reading (a single incident beam), the diffraction efficiency can be monitored as above using the He-Ne laser, or the diffracted power of the argon laser can be measured directly and recorded as indicated in Figure 60.

Angular selectivity measurements are performed with a low-power laser so as not to alter the already written hologram being read. The crystal is rotated with a rotary mechanism and the diffracted power is thus measured as a function of the angle of incidence of the reading

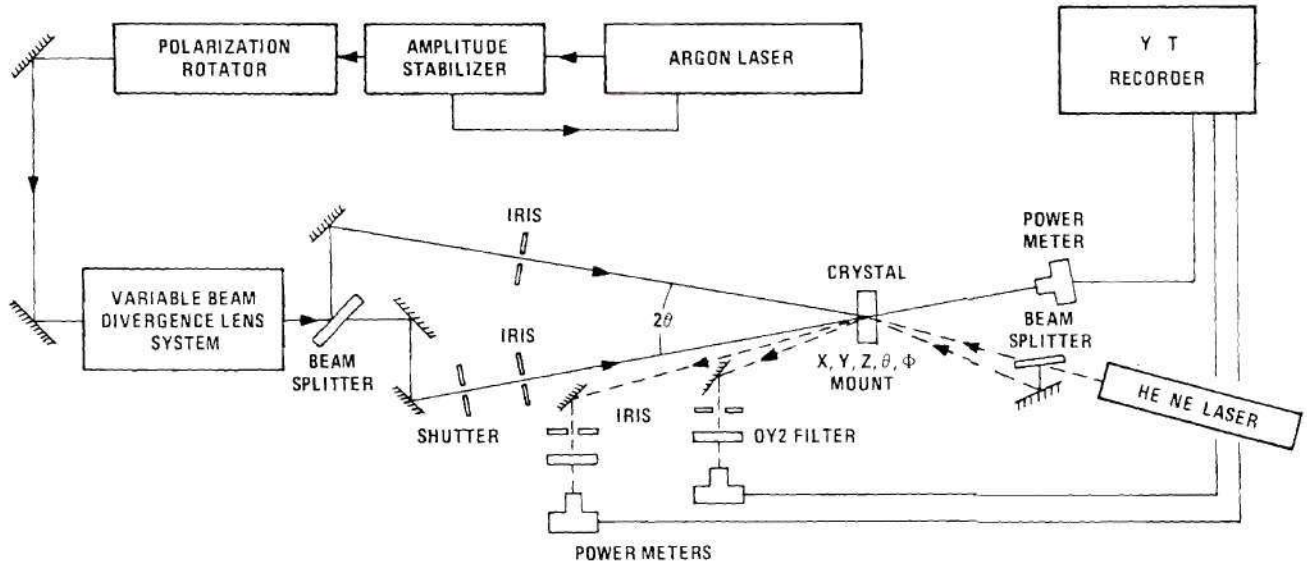

Figure 60. Experimental Configuration for Measuring the Optical Holographic Storage Properties of Electro-Optic Crystals

beam.

5.2 Evaluation of Experimental Parameters

In this section, the evaluation of the experimental parameters that enter the dynamic coupled-wave equations governing volume holographic recording and readout is described. The determination of absorption coefficients, incident field strengths, and refractive index exposure sensitivity is discussed.

5.2.1 Absorption Coefficients

The absorption coefficients of the crystals used in the experiments can be evaluated from intensity measurements at the appropriate wavelengths. If I_o is the intensity (W/m^2) of an incident laser beam with an external angle of incidence α' and I_t is the transmitted intensity, the absorption coefficient, α_o, is given by the usual formula[58]

$$\alpha_o = - \frac{\cos\alpha''}{d} \ln[I_t/I_o(1-R_r)^2], \tag{30}$$

where d is the crystal thickness and α'' is the refraction angle related to α' by Snell's Law $\sin\alpha' = n_o \sin\alpha''$ where n_o is the refractive index of the material appropriate for the particular wavelength and incident angle used. The reflection coefficient, R_r, (for the E-mode polarization) is given by

$$R_r = \tan^2(\alpha'-\alpha'')/\tan^2(\alpha'+\alpha'') \tag{31}$$

for the low-loss material used in this work. The factor $(1-R_r)^2$ in

Eq. (30) accounts for the primary reflections at each surface of the crystal. Thus, it is assumed, to a very good approximation, that most of the light energy is confined in the first two passes through the material with negligible contributions from multiply reflected wavelets. The measured transmitted and reflected intensities are then, respectively, $I_t = I_o(1-R_r)^2\exp(-\alpha_o d/\cos\alpha")$ and $I_r = I_o R_r + I_o(1-R_r)^2 R_r\exp(-2\alpha_o d/\cos\alpha")$. Equation (30) comes from the first of these. Combining these expressions for I_t and I_r and neglecting terms in R_r^3 yields

$$(I_r I_o + 2I_o^2)R_r^2 - (I_t^2 + I_o^2 + 2I_r I_o)R_r + I_r I_o \simeq 0. \qquad (32)$$

This equation can be solved for R_r permitting a simple experimental evaluation of the reflection coefficient. This is useful when the reflection properties of the material have been altered (for example by anti-reflection coatings) and Eq. (31) is not applicable. Equations (31) and (32) are found to be in good agreement for crystals of iron-doped $LiNbO_3$.

5.2.2 Incident Fields and Diffraction Efficiency

The intensity, I, measured by the power meters used in the experiments is the effective, or rms, power density. From such a measurement, the rms amplitude of the associated electric field, E, is computed by[58]

$$E = (Z_o I)^{\frac{1}{2}}, \qquad (33)$$

since the laser beams are taken to be planar waves. Z_o is the impedance of free space ($Z_o \simeq 377$ ohms).

To obtain the incident electric field amplitudes inside the crystal (R_o, S_o, R'_o, S'_o) appropriate for the model used, the similar relation

$$E_o = [Z_o I_o (1-R_r)/n_o]^{\frac{1}{2}} \tag{34}$$

is employed.

The experimental diffraction efficiency is found by

$$\eta = \ell I_d/(1-R_r)^2 I_o, \tag{35}$$

where I_d is the diffracted intensity recorded during the experiment and ℓ is a constant factor accounting for the power losses incurred by the diffracted wave in the optics between the crystal and the detector (see Fig. 60). The factor $(1-R_r)^2$ accounts for the reflection losses at the input and output faces of the crystal [as in Eq. (30)].

It is to be noted that in this work interference effects due to multiple internal reflections are neglected. Experimental tests[59] have indicated that the crystals used here do not satisfy the flatness-and-parallelism requirements necessary for such effects to influence the results significantly. When multiple internal reflections are important, however, the theoretical diffraction efficiency must be corrected by a transmittance factor such as that given by Cornish and Young[59] before comparison with experiment is attempted. This correction applies to (static) readout only and not to the dynamic process of hologram formation. If appreciable multiple internal reflections are present, the grating-forming possibilities of these must be considered

in modeling the total behavior. Multiple internal reflections can be virtually eliminated by applying suitable anti-reflection coatings on the crystal surfaces. Both coated and uncoated crystals have been used in this work. In most cases, the results are very similar, further indicating minimal contributions from the interference effects of multiply reflected beams to the experimental results presented in this thesis.

5.2.3 Exposure Sensitivity

In the limit of a very short exposure time, it is possible to obtain analytical solutions of the dynamic coupled-wave equations. The derivation is shown in Appendix B. The corresponding diffraction efficiency is

$$\eta = e^{-2b_2} \sin^2[b_3(1-e^{-2a_2})/2a_2], \tag{36}$$

where:

$$a_2 = \alpha_o d/\cos\theta,$$

$$b_2 = \alpha_o' d/\cos\theta', \text{ and}$$

$$b_3 = 2\pi a d T R_o S_o \cos^2 2\theta/\lambda'\cos\theta'.$$

This expression is valid for $R_o \simeq S_o$ and $\phi_n = 0$. However, as can be shown by numerical solution of the full coupled-wave equations, the writing characteristics (η vs. T curves) coincide for all ϕ_n for small T (see, for example, Figure 30). Equation (36) is, therefore, useful for calculation of the refractive index exposure sensitivity, a, in terms of the experimental variables selected. Solving Eq. (36)

for a gives

$$a = \{\alpha_o \lambda' \cos\theta' \sin^{-1}[\eta \exp(2\alpha_o' d/\cos\theta')]^{\frac{1}{2}}\}/$$

$$\{\pi T R_o S_o \cos\theta \cos^2 2\theta [1 - \exp(-2\alpha_o d/\cos\theta)]\}. \qquad (37)$$

Equation (37) is important because it allows an evaluation of the theoretically introduced proportionality coefficient, a, that is consistent with the given experimental conditions. In the case of a time dependent exposure sensitivity, Eq. (37) gives its initial value.

5.3 Writing

In this section, experimentally observed writing characteristics are compared with corresponding theoretical characteristics calculated under the same conditions. An example of the results is given in Fig. 61. An exact quantitative agreement between theory and experiment is not obtained. However, the major features are strongly correlated up to $T \simeq 50$ sec if $\phi_n = 30°$ is selected. The deviations are most pronounced at the maxima and minima of the pattern. This kind of disagreement is consistently observed (when ϕ_n is not close to 90°) and has been verified with repeated experiments. Similar deviations, for example, occur in Fig. 62. In this case, the minimum is closer to zero than in the previous figure and the second maximum is somewhat larger than the first one. In Fig. 63, as a final example, the experimental data of Fig. 6 is repeated (corrected for the primary reflections) and shown with the corresponding theoretical curve. This is the only example obtained in this laboratory of diffraction

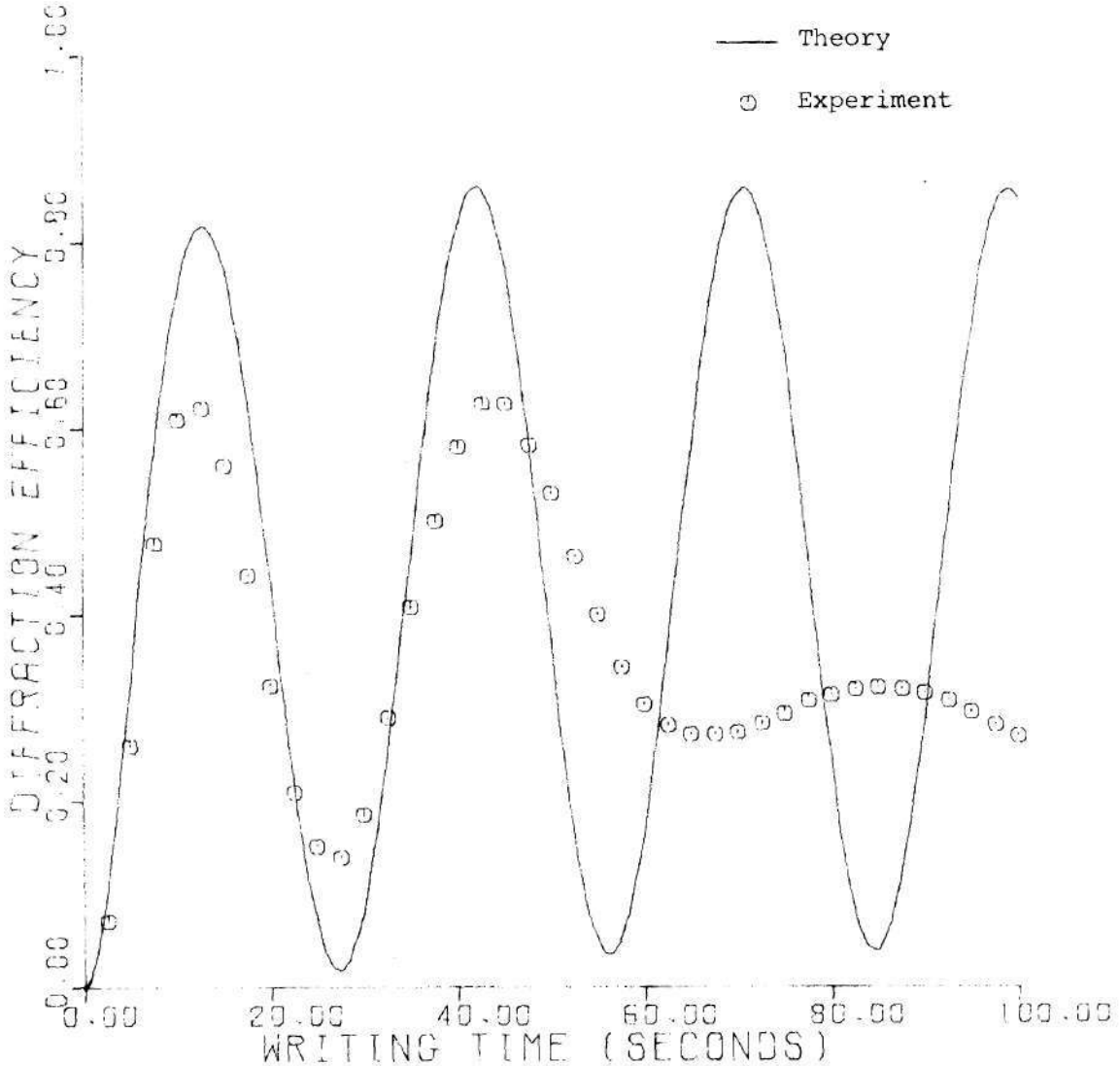

Figure 61. Comparison of Experimental and Theoretical Writing Characteristics. The Recording Material is a Crystal of $LiNbO_3$ Doped with 0.1 Mole % Fe. The Hologram Parameters are: $\lambda = 0.5145$ μm, $\lambda' = 0.6328$ μm, $\alpha_o = 87\ m^{-1}$, $\alpha_o' = 24.8\ m^{-1}$, $d = 1.86$ mm, $\phi_n = 30°$, $a = 2.22 \times 10^{-11} (V/m)^{-2} sec^{-1}$, $R_o = 639$ V/m, and $S_o = 610$ V/m.

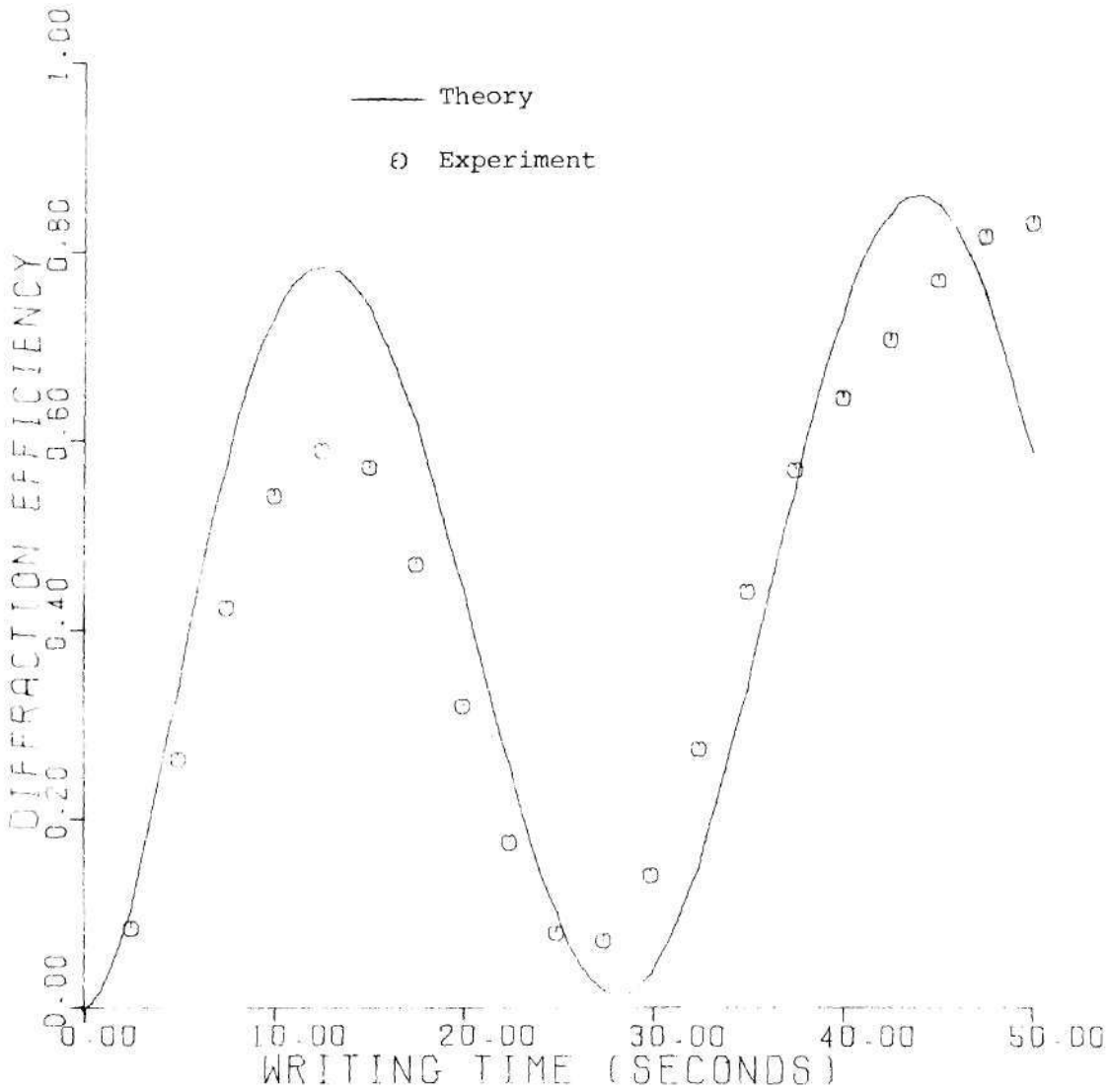

Figure 62. Comparison of Experimental and Theoretical Writing Characteristics. The Recording Material is an Anti-Reflection Coated Crystal of $LiNbO_3$ Doped with 0.02 Mole % Fe. The Hologram Parameters are: λ = 0.5145 μm, λ' = 0.6328 μm, α_o = 111 m^{-1}, α_o' = 19.5 m^{-1}, d = 2.12 mm, ϕ_n = 36°, a = $1.96 \times 10^{-11} (V/m)^{-2} sec^{-1}$, R_o = 671 V/m, and S_o = 639 V/m.

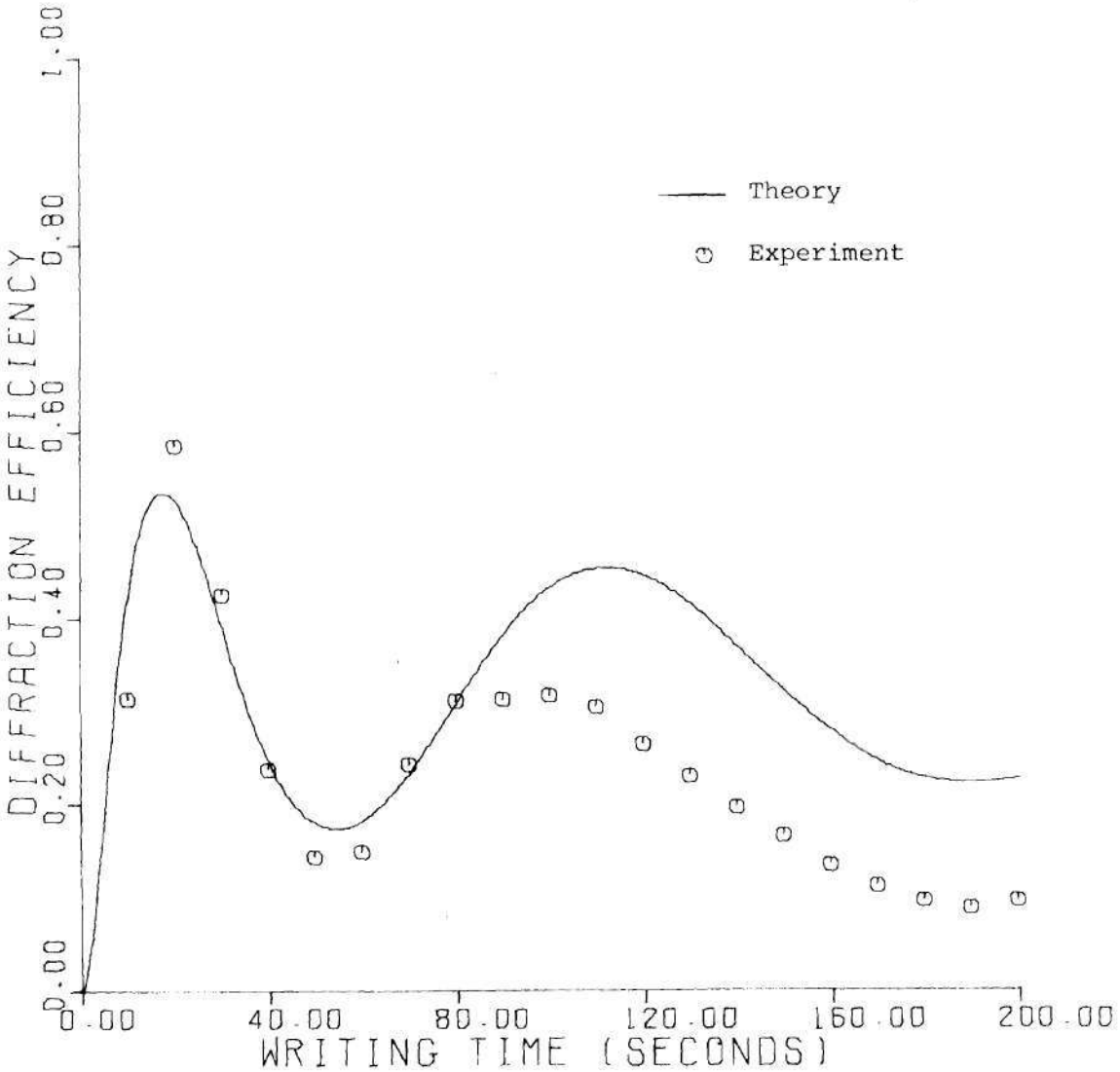

Figure 63. Comparison of Experimental and Theoretical Writing Characteristics. The Recording Material is a Crystal of $LiNbO_3$ Doped with 0.1 Mole % Fe. The Hologram Parameters are: $\lambda = 0.5145$ μm, $\lambda' = 0.6328$ μm, $\alpha_o = 59\ m^{-1}$, $\alpha_o' = 22.8\ m^{-1}$, $d = 1.66$ mm, $\phi_n = 85°$, $a = 5.20 \times 10^{-12} (V/m)^{-2} sec^{-1}$, $R_o = 1181$ V/m, and $S_o = 1130$ V/m.

efficiency behavior exhibiting the features of diffusion-dominated hologram formation (i.e. $\phi_n = 85°$). In this exceptional case, experimental diffraction efficiency is found to be somewhat larger than that calculated at the first maximum.

In contemplating the reasons for the observed deviations between theory and experiment, it should be recalled that the mathematical model employs infinite plane waves while in the laboratory laser beams of bounded extent are used. It is, indeed, believed that this is the most serious deficiency of the present model and the cause of the observed discrepancies. It is easily visualized that laser beams with spatially varying intensity profiles such as the Gaussian beams used in the experimental work will produce a hologram that has spatially varying (x and y directions as well as the z direction; see Fig. 1) diffraction properties. The area within the hologram receiving the highest power density during recording will develop fastest. Thus, some parts of the hologram may actually be increasing in diffraction efficiency while other areas are decreasing (i.e. have reached the first peak on the diffraction efficiency characteristic). This would tend to dampen the diffraction efficiency oscillations in exposure time. As a matter of fact, it has been observed that the oscillations are greatly reduced when diffraction efficiency is measured directly by periodically blocking one of the writing beams briefly during the recording process, thus illuminating the full hologram for readout. In this case, oscillations such as those illustrated in Figs. 61 and 62 are not seen but, instead, much lower-amplitude oscillations at relatively high efficiency are seen, somewhat resembling the data of Kim et. al.[60]

who use this method of measurement. A representative experimentally observed example of this type of behavior is shown in Fig. 64. Furthermore, when the auxiliary readout beam (see Fig. 60) is expanded (its extent is usually maintained somewhat smaller than the hologram) so as to illuminate the hologram fully, similar behavior is observed with the oscillations, again, greatly reduced in amplitude.

The spatially inhomogeneous diffraction properties of thick holograms can also be observed visually during hologram recording. It is frequently noticed that the intensity profile of the diffracted beam develops a null in the center (this would correspond to the first null in the η-t pattern). This intensity minimum may then disappear and reappear and is often associated with spatially inhomogeneous intensity profiles that form approximately concentric distributions of light energy. A strong rim-like intensity concentration at the beam periphery has been experimentally observed. Depending on the material quality and exposure conditions, these may be very nearly radially symmetric distributions or possibly asymmetric, with parts of the intensity rings missing or misaligned. Similar comments apply to the associated zeroth order beam. The intensity variations across the beams have been measured using a scanning, pinhole-masked photodetector. In general, it is found that the beam profiles (writing and readout beams) remain Gaussian only at the early stages of hologram formation with the profile degradation increasing with exposure and hologram development. This further complicates the recording beam interaction and can contribute to the spatial diffraction efficiency inhomogeneity.

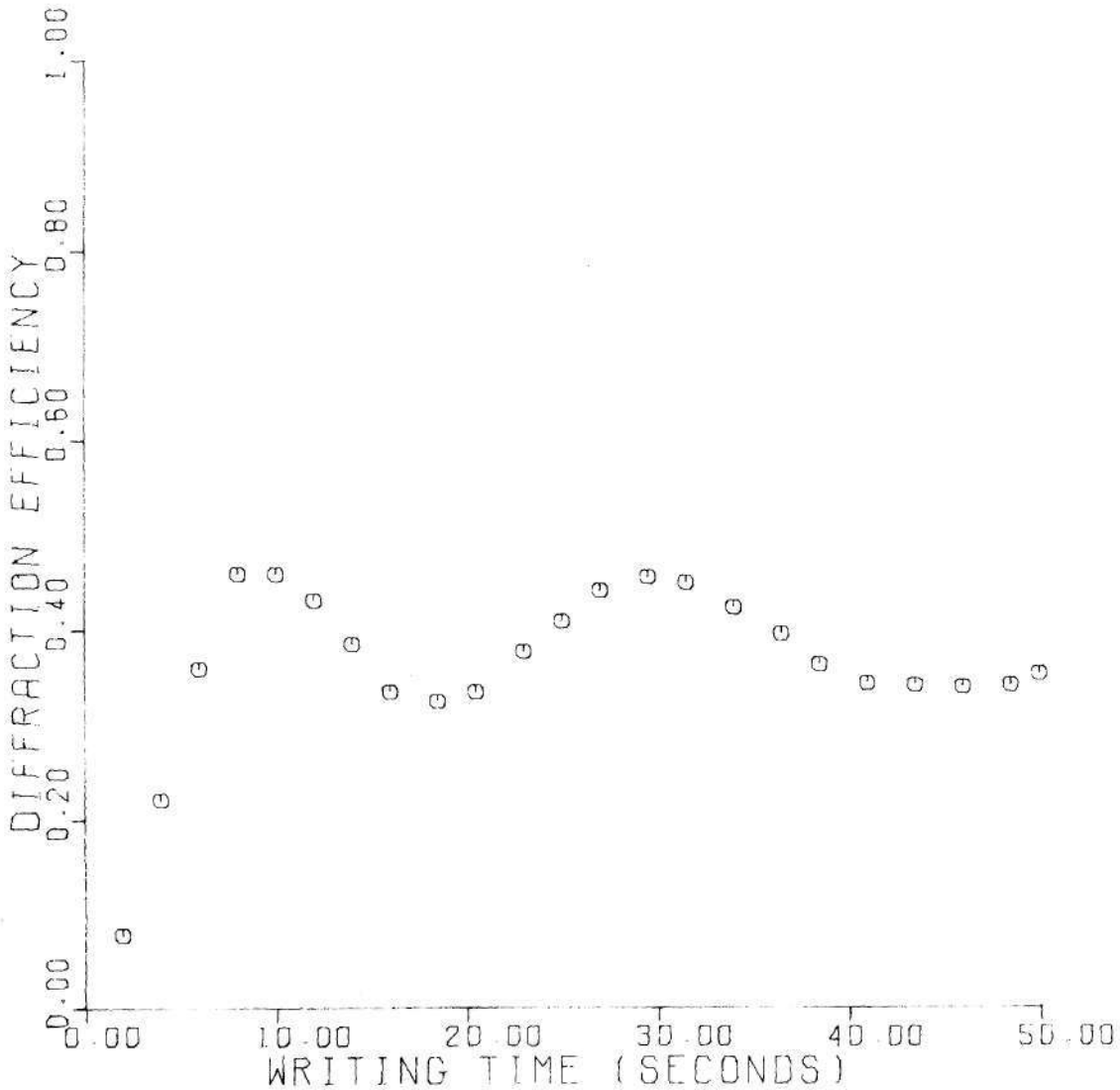

Figure 64. Experimentally Observed Writing Characteristics Measured by Periodically Blocking One of the Recording Beams. Thus, Readout is Performed by a Beam Fully Illuminating the Hologram which Enhances the Influence of the Spatially Varying Diffraction Efficiency. As a Result, the Diffraction Efficiency Oscillations are Reduced in Amplitude.

Effects of a similar nature have been discussed in a recent paper by Chu and Tamir.[61] These workers analyzed the readout of a uniform hologram grating by a Gaussian laser beam. In particular, they found that the modulated medium causes intensity profile distortion of the diffracted and transmitted (coupled) readout beams so that these are no longer Gaussian after a finite propagation distance into the medium. Consequently, complete coupling of energy from one beam to the other cannot be achieved and the diffraction efficiency will necessarily be lower than that predicted by theories using unperturbed infinite plane waves.[61]

The case presently under discussion is considerably more complicated than that treated by Chu and Tamir in that both the recording and readout processes are being described and the writing process alone, as has been indicated above, leaves a spatially nonuniform (x,y,z) hologram that is subsequently to be read. At each instant in writing time, therefore, diffraction from this spatially inhomogeneous structure is measured. As a result, the experimental oscillatory behavior is somewhat dampened (see Fig. 64 for an extreme case) which is the reason for the quantitative discrepancies between experiment and theory as illustrated in Figs. 61 and 62. The actual diffraction efficiency measured may be expressed as

$$\eta(t) = \iint_{-\infty}^{\infty} S(x,y,d,t)S^*(x,y,d,t)dxdy \Big/ \iint_{-\infty}^{\infty} R_o'(x,y,0)R_o'^*(x,y,0)dxdy, \qquad (38)$$

where S is the amplitude of the diffracted readout beam. The moderate

diameter auxiliary readout beam measuring technique used is seen to avoid, to some extent, the effects of the spatial inhomogeneity and thus the major features of the experimental results agree with the theory for a considerable exposure range.

In Figs. 6 and 61 (and during numerous other experiments), significantly reduced third-peak diffraction efficiency oscillations are measured. This reduction can be attributed to the combined effects of increased nonuniformity in the hologram diffraction properties, decreasing exposure sensitivity, and scattering (see Chapter VI). The influence of these increases with increasing exposure. If the first of these dominates, the condition

$$\iint_{-\infty}^{\infty} \frac{d\eta_u(x,y,t)}{dt}\, dxdy \gtrsim 0, \tag{39}$$

where η_u is the diffraction efficiency per unit area, prevails at these high exposure levels. That is, at each time instant there is approximately as much decrease as there is increase in the total diffraction efficiency due to the nonuniform development of the hologram. Thus, after this condition is reached the diffraction efficiency is only weakly modified by further recording. Additionally, saturation effects (i.e. reduction in exposure sensitivity) certainly influence the behavior to some extent. Laser-scattering induced holographic patterns are observed in every experiment using high exposure. Scattering effects strongly influence the data of Fig. 6 after $T \gtrsim 100$ sec.

5.4 Readout

Dynamic readout is a more complicated process than recording in the sense that a new grating is superimposed onto the existing one as a result of wave diffraction and subsequent interference. It can, thus, be expected that a theory that does not completely quantitatively describe the recording process will be somewhat less successful in predicting the dynamic readout process. As shown in Figs. 65, 66, and 67, this is, indeed, found to be the case. Figure 65 illustrates R-beam readout. The efficiency is observed to decrease initially experimentally and theoretically. In Fig. 66, it is seen that S-beam readout, for this particular example, does not alter the diffraction efficiency initially (T'=0) and thus $\phi_n = 0°$ is implied. The theoretical and experimental diffraction efficiency behaviors exhibited in Figs. 65 and 66 are qualitatively similar, with the best quantitative agreement at the beginning of the exposure. Figure 67 gives an example of the effects of R and S readout as observed in the same crystal. The agreement of theory and experiment is quite good for about the first 20 sec. of readout. This result is a theoretical and experimental illustration of the erasure-enhancement effect discussed in Sec. 4.5 and is consistent with the ideas set forth there if the +c axis of the crystal is experimentally chosen to point in the +x direction in the coordinate system of Fig.1. Therefore, this result may be taken as an experimental confirmation that the phase shift ϕ_n is of a single sign (see Sec. 4.5) in anisotropic electro-optic crystals. Furthermore, this indicates

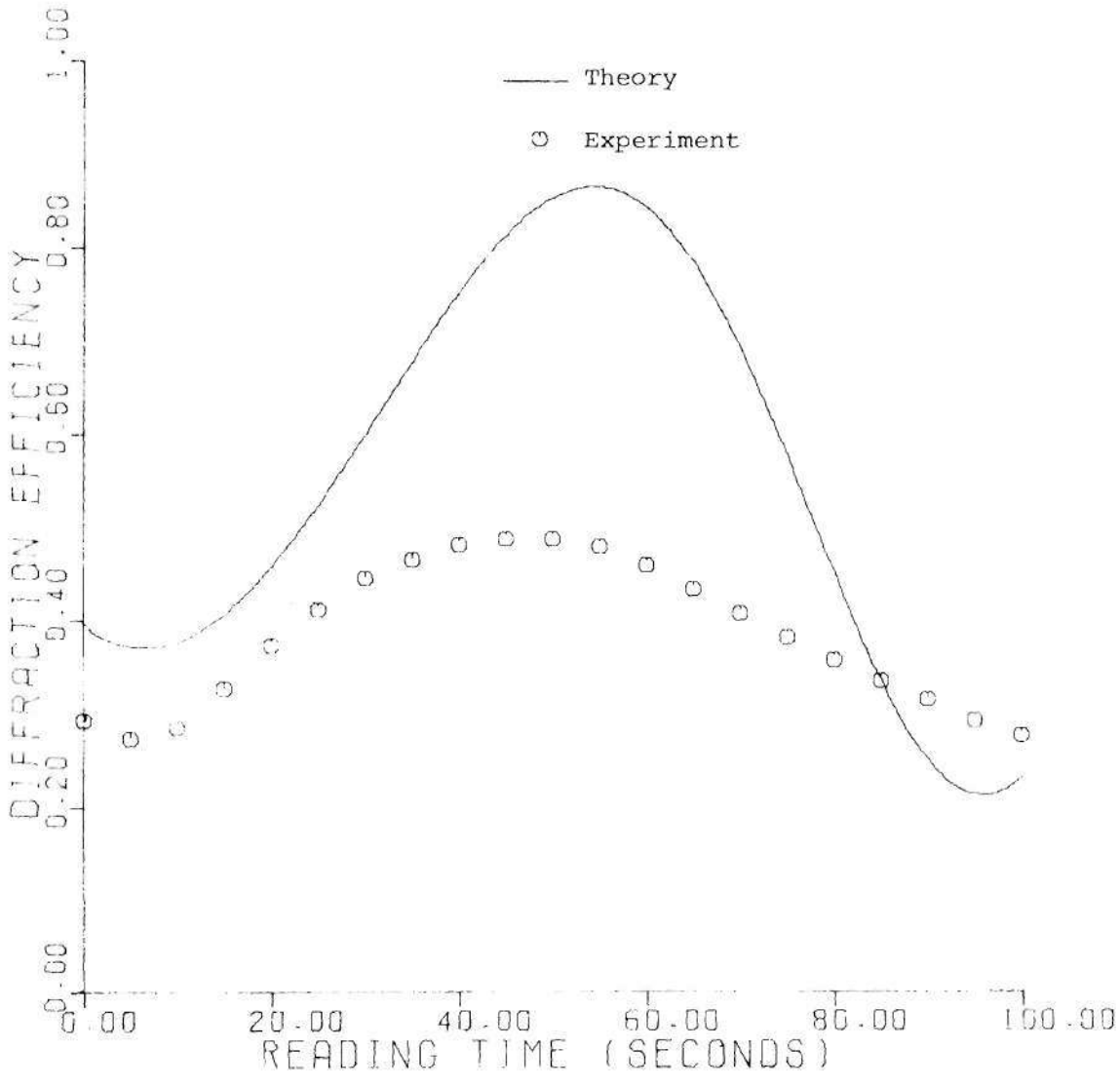

Figure 65. Comparison of Experimental and Theoretical R-Beam Readout Characteristics. The Recording Material is a Crystal of $LiNbO_3$ Doped with 0.1 Mole % Fe. The Hologram Parameters are: $\lambda = 0.5145$ μm, $\lambda' = 0.6328$ μm, $\alpha_o = 87\ m^{-1}$, $\alpha_o' = 25\ m^{-1}$, $d = 1.86$ mm, $\phi_n = 10°$, $a = 2.4 \times 10^{-11} (V/m)^{-2} sec^{-1}$, $R_o = 636$ V/m, $S_o = 605$ V/m, $T = 5$ sec, $R_o' = 633$ V/m, and $S_o' = 0$.

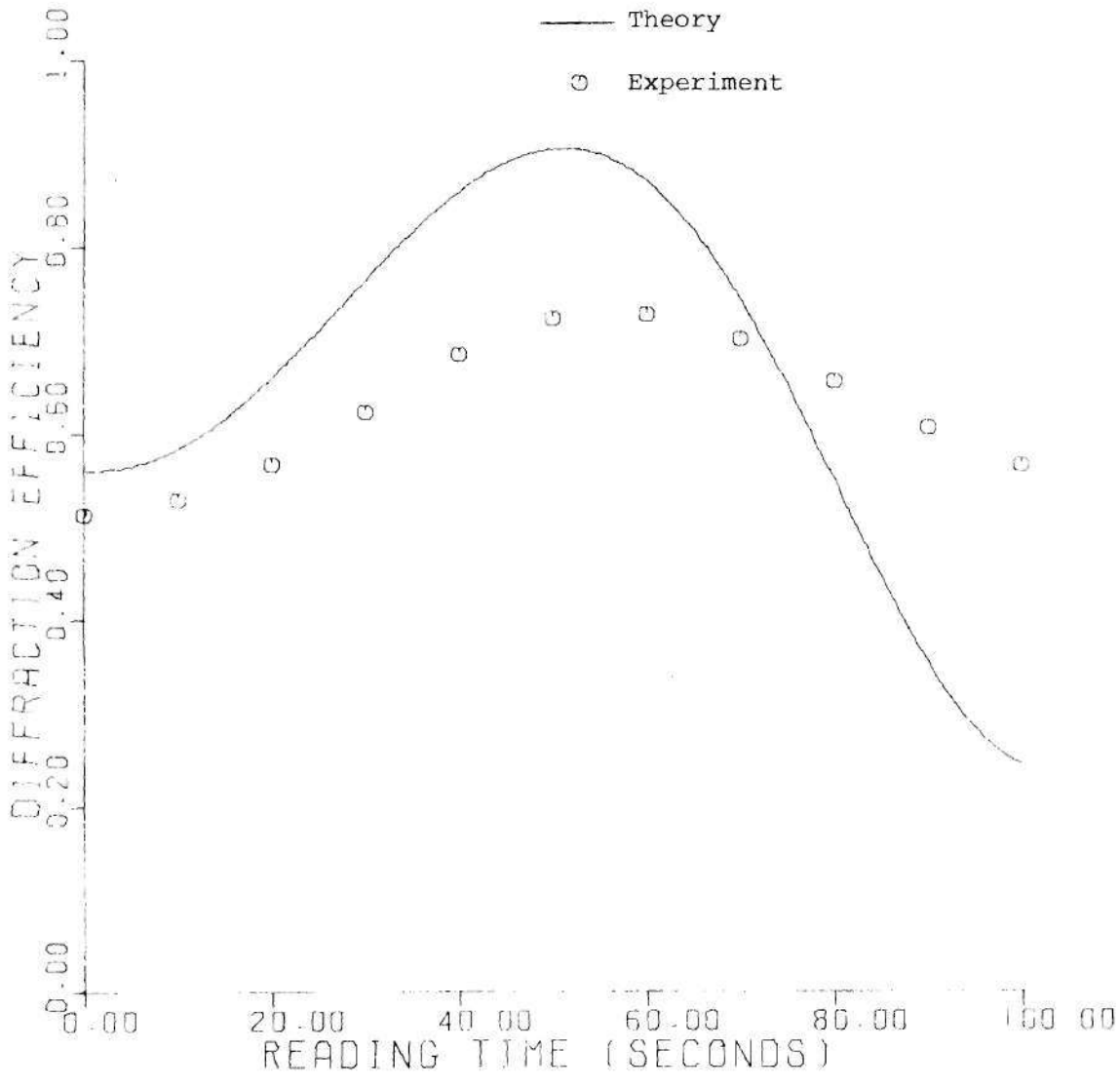

Figure 66. Comparison of Experimental and Theoretical S-Beam Readout Characteristics. The Recording Material is a Crystal of $LiNbO_3$ Doped with 0.1 Mole % Fe. The Hologram Parameters are: $\lambda = 0.5145$ μm, $\lambda' = 0.6328$ μm, $\alpha_o = 87\ m^{-1}$, $\alpha_o' = 25\ m^{-1}$, $d = 1.86$ mm, $\phi_n = 0°$, $a = 2.6 \times 10^{-11} (V/m)^{-2} sec^{-1}$, $R_o = 582$ V/m, $S_o = 545$ V/m, $T = 7$ sec, $S_o' = 539$ V/m, and $R_o' = 0$.

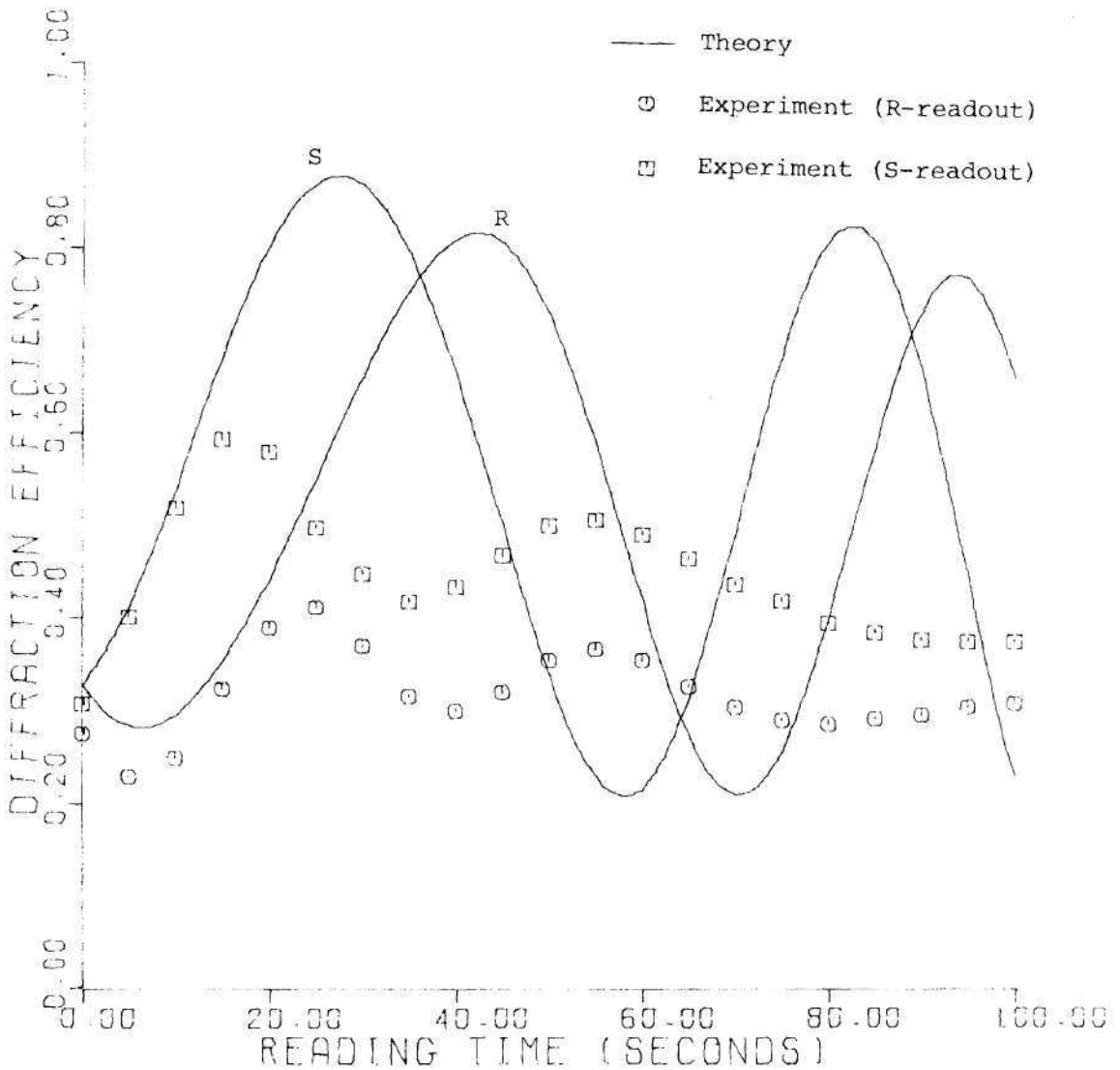

Figure 67. Comparison of Experimental and Theoretical Readout Characteristics. The Recording Material is an Anti-Reflection Crystal of $LiNbO_3$ Doped with 0.1 Mole % Fe. The Hologram Parameters are: $\lambda = 0.5145$ μm, $\lambda' = 0.6328$ μm, $\alpha_o = 158$ m^{-1}, $\alpha_o' = 28.8$ m^{-1}, $d = 2.12$ mm, $\phi_n = 15°$, $a = 1.48 \times 10^{-11}$ $(V/m)^{-2}$ sec^{-1}, $R_o = 1015$ V/m, $S_o = 973$ V/m, $T = 3$ sec, $R_o' = 1015$ V/m, and $S_o' = 947$ V/m.

that the refractive index grating is shifted in the -c direction relative to the light interference pattern (see Fig. 53).

It has been experimentally observed that the beam profiles deviate more quickly from the Gaussian shape during dynamic readout than during recording. The reason is that during recording a more nearly unity beam intensity ratio is maintained longer (at least when ϕ_n is not close to 90° and this seems to be the case in most of the present experiments) and the profiles remain approximately Gaussian longer. On readout, the beam intensity ratio can be significantly different from unity and spatially varying since it depends on the (generally spatially inhomogeneous) diffraction efficiency at each point. The addition to the grating by the dynamic readout process can thus be significantly spatially varying which could allow the condition represented by Eq. (39) to become effective for lower exposure than during recording. (Note the relatively damped oscillations in the experimental data, particularly in Fig. 67, and compare with Fig. 64.) Therefore, beam profile distortion and associated spatial variation of diffraction efficiency may additionally contribute to the theory-experiment discrepancies on readout.

5.5 Angular Selectivity

Angular selectivity refers to the (static) measurement of diffraction efficiency versus the readout beam incident angle at a given location on the hologram recording characteristic. Figure 68 compares theory and experiment for a 1.66 mm thick crystal of $LiNbO_3$. The major features are in a good agreement with the quantitative

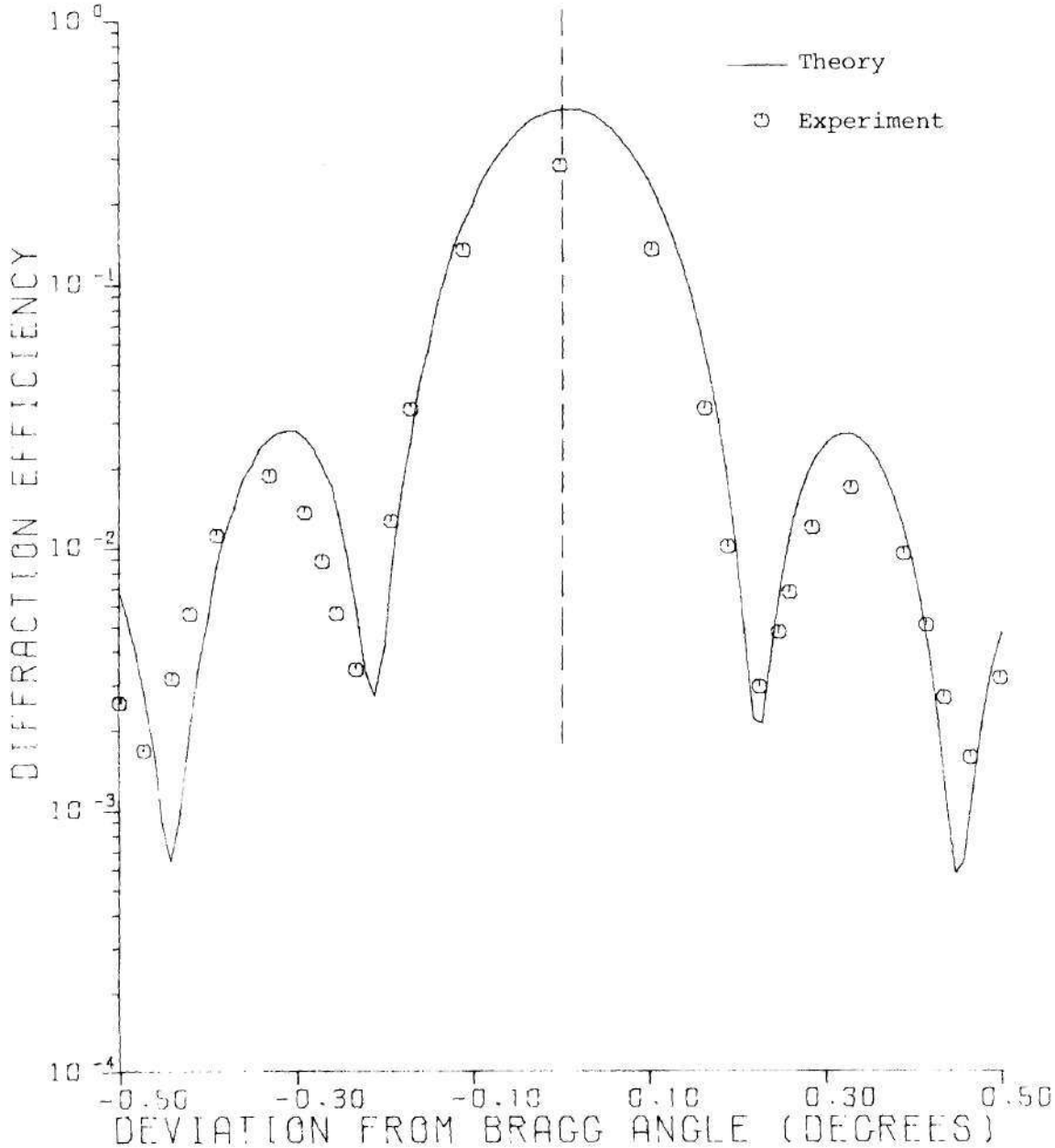

Figure 68. Comparison of Experimental and Theoretical Angular Selectivity Characteristics. The Recording Material is an Anti-Reflection Coated Crystal of $LiNbO_3$ Doped with 0.1 Mole % Fe. The Hologram Parameters are: $\lambda = 0.5145$ μm, $\lambda' = 0.6328$ μm, $\alpha_o = 109\ m^{-1}$, $\alpha_o' = 42.1\ m^{-1}$, $d = 1.66$ mm, $\phi_n = 15°$, $a = 5.16 \times 10^{-12} (V/m)^{-2} sec^{-1}$, $R_o = 1094$ V/m, $S_o = 1064$ V/m, and $T = 10$ sec. Vertical Dashed Line Indicates Position of Bragg Angle.

difference largest at the central peak (i.e. on the Bragg angle). Similar comments apply to Fig. 69 (a 2.12 mm thick crystal). The lobes in the pattern are accordingly narrower than in Fig. 68 both experimentally and theoretically. The data of Fig. 70 are obtained in the same 2.12 mm thick crystal but after a longer exposure. The measurement is performed at a point along the negative slope on the writing characteristics just after the first maximum. It is seen that the central lobe has become somewhat narrower with the experimentally observed and theoretically calculated peaks occurring off the Bragg angle. Again, the major aspects of the theoretical and experimental behavior agree, both exhibiting similar asymmetry with respect to the Bragg angle. Figure 22 shows similar agreement for a larger angular range but for a lower ($\sim$ 1%) efficiency hologram.

In the above cited data it is consistently observed that the experimental and theoretical sidelobe structures are in increasing disagreement in angle with increasing deviation from the Bragg angle. The experimental nulls always occur at larger deviations than do the corresponding theoretical ones. This is presently not fully understood.

5.6 Discussion

This chapter has dealt with the experimental aspects of this research. The terminal characteristics of volume holograms as calculated by the dynamic theory have been compared with corresponding experimentally measured characteristics. A detailed quantitative agreement between theory and experiment is not observed. However, the major features of the experimental and theoretical data are strongly

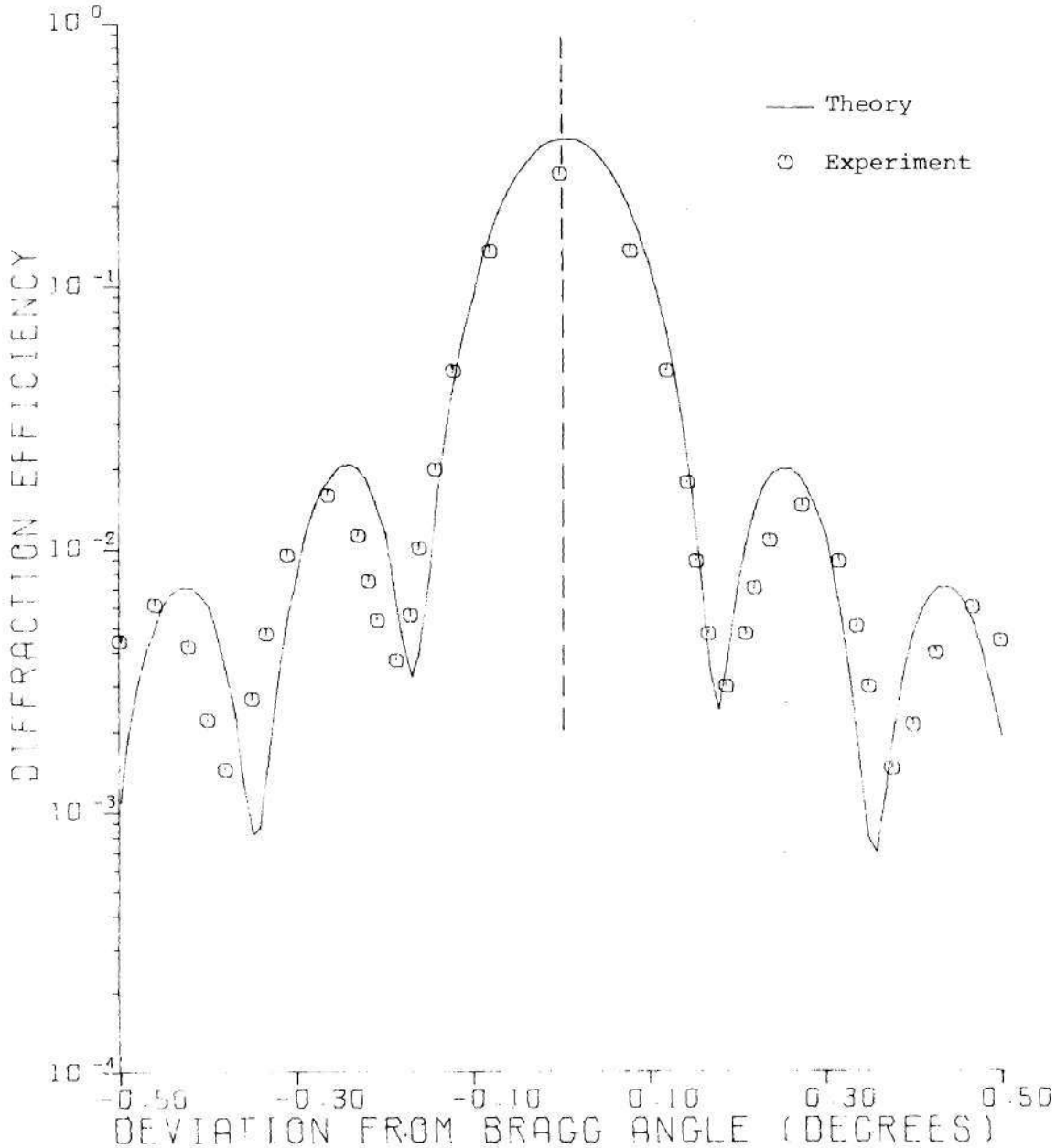

Figure 69. Comparison of Experimental and Theoretical Angular Selectivity Characteristics. The Recording Material is an Anti-Reflection Coated Crystal of $LiNbO_3$ Doped with 0.02 Mole % of Fe. The Hologram Parameters are: $\lambda = 0.5145$ μm, $\lambda' = 0.6328$ μm, $\alpha_o = 107\ m^{-1}$, $\alpha_o' = 25.7\ m^{-1}$, $d = 2.12$ mm, $\phi_n = 20°$, $a = 9.5 \times 10^{-12} (V/m)^{-2} sec^{-1}$, $R_o = 1063$ V/m, $S_o = 1030$ V/m, and $T = 4$ sec. Vertical Dashed Line Indicates Position of Bragg Angle.

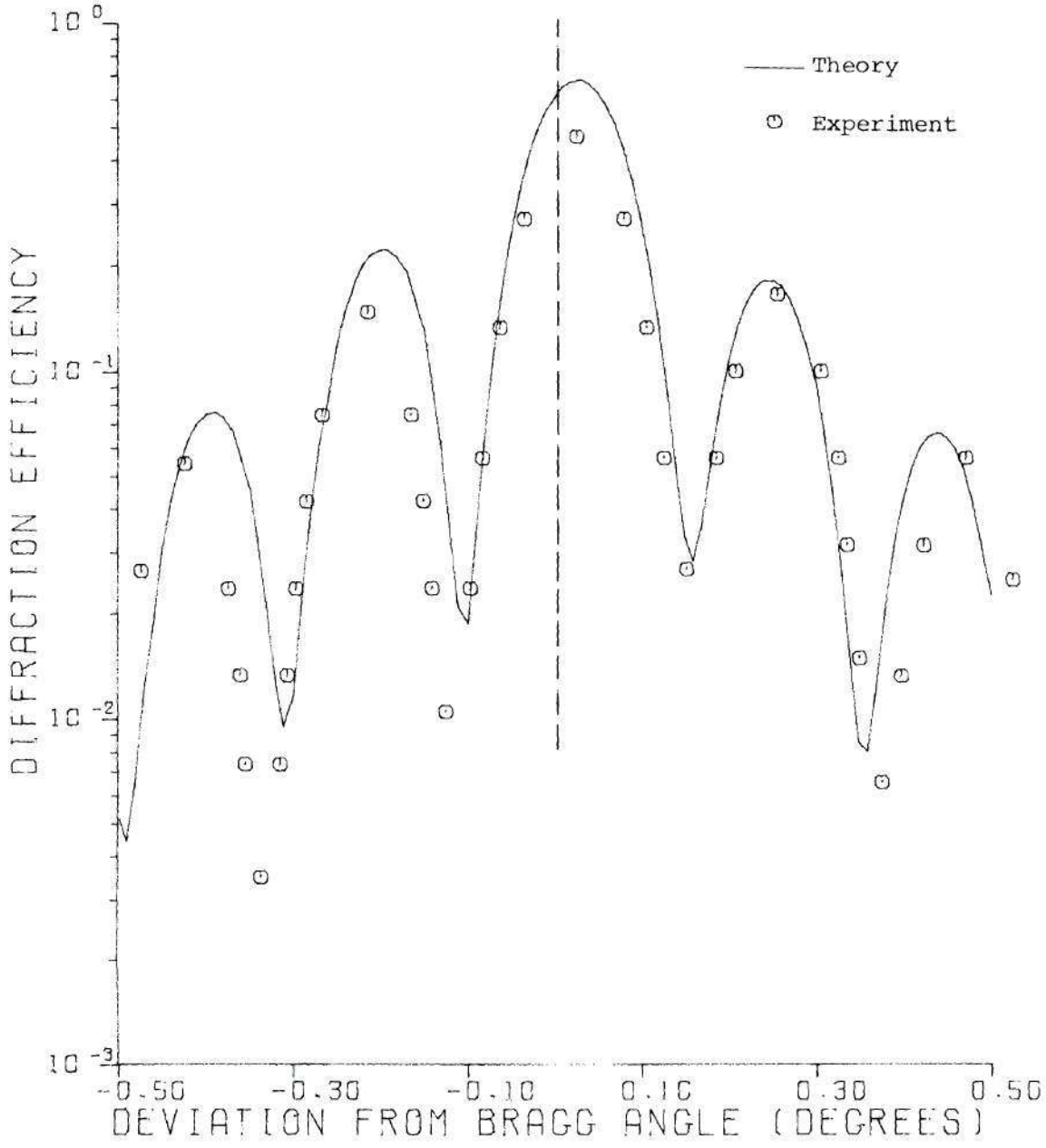

Figure 70. Comparison of Experimental and Theoretical Angular Selectivity Characteristics. The Recording Material is an Anti-Reflection Coated Crystal of $LiNbO_3$ Doped with 0.02 Mole % Fe. The Hologram Parameters are: λ = 0.5145 μm, λ' = 0.6328 μm, α_o = 107 m^{-1}, α_o' = 25.7 m^{-1}, d = 2.12 mm, ϕ_n = 20°, a = $8.0 \times 10^{-12} (V/m)^{-2} sec^{-1}$, R_o = 1082 V/m, S_o = 1049 V/m, and T = 15 sec. Vertical Dashed Line Indicates Position of Bragg Angle.

correlated. The major deviations are believed to stem from the assumption of the theory that infinite planar waves propagate at all times in the material under study. This situation is not realizable in the laboratory where bounded-extent laser beams are used. Spatial laser beam intensity variations (Gaussian profile) and subsequent beam profile distortions (due to the hologram being written) are experimentally found to give rise to spatially varying holographic diffraction efficiency. This, in turn, limits the effectiveness with which light energy is coupled between the directly transmitted and the diffracted beams and, therefore, limits the amplitude of the diffraction efficiency oscillations. Thus, maxima of lower efficiency and minima of higher efficiency than expected for unperturbed infinite plane waves existing at all times and at all points in space are observed (Figs. 61 and 62). A dramatic display of such an effect is given in Fig. 64. The use of a readout beam of a smaller extent than the hologram is found to avoid much of these aperture effects of the hologram and allows measurement of the significant salient features of the behavior. Further improvements in the measurement techniques are expected to bring theory and experiment into closer agreement. In that effort, the goal is to produce experimentally more nearly planar waves and to attempt to reduce the effects of the boundedness of the beams.

During a number of the experiments conducted in this research, it was observed that many higher-order diffracted beams existed while reading at the first Bragg angle. As many as nine simultaneous orders have been seen. The diffraction efficiency of the -1 order can be more than one-third of that in the +1 order, which is nonnegligible.

Such effects are generally not expected in these very thick ($\sim$ 2 mm) crystals. It is believed that the reason for this behavior is related to the formation of nonsinusoidal gratings.

The contribution of experimental errors to the theory-experiment deviations is not great. The experimental diffraction efficiency is a ratio of measured intensities and each measurement has approximately the same percent error. This basically eliminates systematic errors. Further, in the numerous experiments performed in this research, reproducibility has been quite good. For example, the maximum diffraction efficiency obtained on hologram writing for a given set of conditions is consistently within a 2% range. This reproducibility indicates that random errors are very small.

The only parameters entering the dynamic theory that are obtained directly from an absolute intensity measurement are the boundary values (R_o, S_o, R'_o, and S'_o) as seen in Eq. (34). A few percent errors (less than 3% due to power meters) in these causes negligible errors in the resulting numerical calculations. The numerical errors in the algorithm used due to the finite step sizes employed contribute only about 1% error at T = 100 sec for typical hologram parameters (such as in Fig. 61). This error increases approximately linearly in time.

CHAPTER VI

LASER SCATTERING EFFECTS

6.1 Introduction

Light scattering phenomena in photosensitive materials subjected to laser exposure have, in general, been poorly understood. Phillips et al.[30] reported light scattering in transition-metal-doped $LiNbO_3$ that has high sensitivity. Only limited explanation was offered. Moran and Kaminow[62] observed a ring pattern due to laser scattering in polymethyl methacrylate (PMMA) but were not able to account for the effect. Zech[52] found that similar ring structures occur in photodegradable polymers subjected to high exposure levels.

The presence of cones of diffracted light upon illumination of previously laser-exposed crystals of lithium niobate is reported in this chapter. These diffraction cones are shown to result from the internally recorded interference pattern (hologram) resulting from the interference of the original incident laser beam with light scattered from material inhomogeneities. Diffraction cones are observed in iron-doped lithium niobate crystals that were exposed to a single laser beam and in crystals that were exposed to two superposed laser beams (i.e. during conventional holographic recording). In the two beam case, the diffraction cones are present in addition to the first order diffracted beam when the conventional two beam

thick hologram is reconstructed.

The diffraction cones, which have their apex in the exposed region of the crystal, are observed as rings (referred to as scattering rings, or diffraction rings) when a screen or a piece of film intersects the cone of light. Figures 71 and 72 show typical diffraction ring patterns observed in crystals of $LiNbO_3$ during volume holography experimentation. The very clear pattern of Fig. 72 emanated from a crystal of high optical quality. For the single beam case, the observed results in lithium niobate are effectively the same as the experimental observations of Moran and Kaminow[62] for PMMA, which had been exposed to ultraviolet laser light. The cones of diffracted light for this case of a single original exposing beam have been explained by Forshaw[63,64] using the Ewald sphere construction from diffraction theory (see, e.g. Reference 51). This method is extended here to describe the diffraction cones that result when there are two intersecting exposing beams as in conventional holographic recording.

6.2 Analytical Description

The Bragg diffraction condition $\Delta\bar{K}_G = \bar{K}' - \bar{K}$ where $\bar{K}'$ and $\bar{K}$ are the diffracted and incident beam wave vectors, respectively, and $\Delta\bar{K}_G$ is the fundamental holographic grating vector, predicts the direction of the well defined first order diffracted beam. Another diffraction pattern is also produced which is described by $\Delta\bar{K}_s = \bar{K}_s - \bar{K}_i$, where $\bar{K}_s$ is any one of the wave vectors of the scattered wavelets of the original writing beam, and $\bar{K}_i$ is the wave vector of the original incident writing beam. The scattered light within

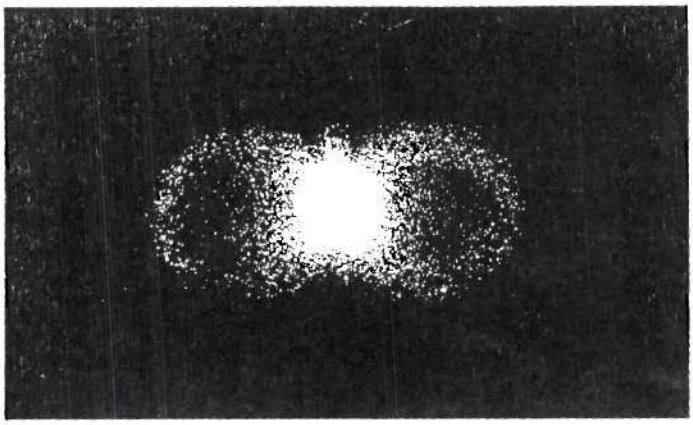

(a)

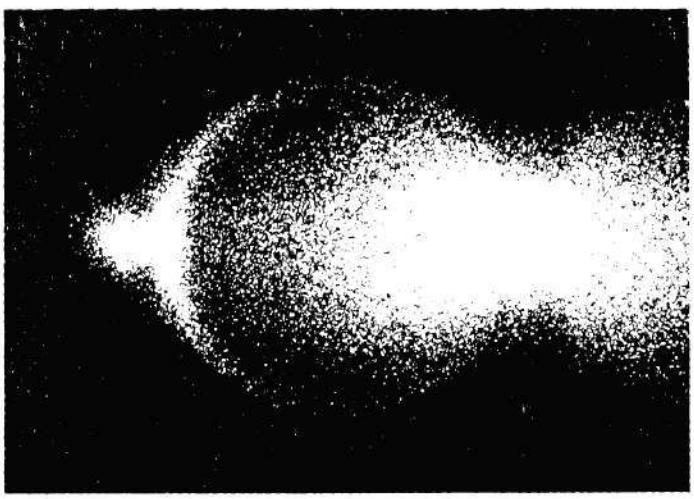

(b)

Figure 71. Typical Observed Diffraction Rings from a Lithium Niobate Crystal in which a Plane Holographic Grating has been Recorded. The Original Writing Beams had a Wavelength λ = 515 nm and the Subsequent Probing Beam for the Above Photographs was of $\lambda' = 633$ nm and had an Angle of Incidence in (a) of $\theta' = 0°$, Resulting in Cone Angles of $\phi_1 = 5.7°$ and $\phi_2 = -5.7°$ and an Angle of Incidence in (b) of $\theta' = 4.5°$, Resulting in a Cone Angle $\phi_1 = 10.6°$. Note in (b) the First Order Diffracted Beam Just to the Left of the Diffraction Ring.

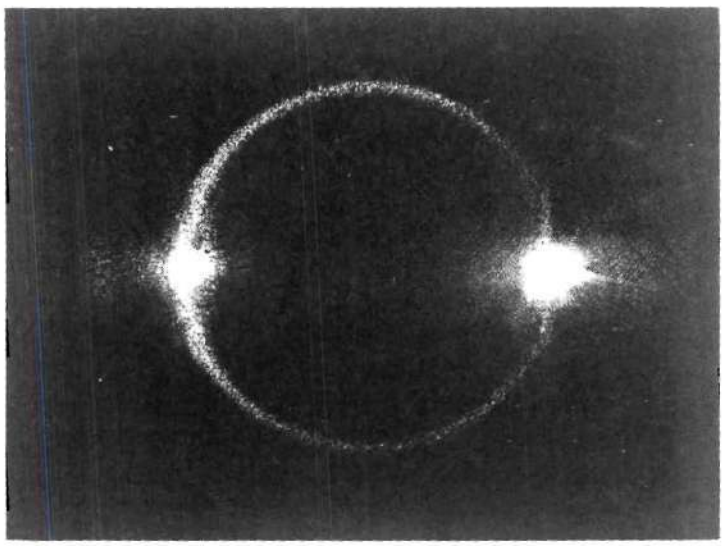

Figure 72. Diffraction Ring Pattern Observed During Holographic Recording in an Iron-Doped Lithium Niobate Crystal. The Readout Beam is Incident at the Bragg Angle. The Diffracted Beam is on the Left and the Transmitted Beam on the Right in the Picture.

the crystal interferes with the original beam and this interference pattern is written into the crystal in the same manner as the basic holographic grating is recorded in the crystal. Figure 73 illustrates the Ewald sphere construction necessary to analyze the diffraction cones that result for the case of two intersecting exposing beams. The surfaces A and B are the primary image loci for the $\Delta\bar{K}_s$ pattern and the surfaces C and D are the corresponding conjugate image loci. That is, the vectors $+\Delta\bar{K}_s$ and $-\Delta\bar{K}_s$, if originating at the intersection of the original writing beams, terminate on the primary and conjugate spheres, respectively. All of these spheres have radii $1/\lambda$ where λ is the writing wavelength. The surface E is the reconstructing sphere with radius $1/\lambda'$ where λ' is the reading wavelength. $\bar{K}_1'$, $\bar{K}_2'$, and $\bar{K}_4'$ are the reconstruction wave vectors and ϕ_1, ϕ_2, and ϕ_4 are the corresponding diffraction cone angles. The intersection of the surface E with each of the other spheres describes a circle. Wave vectors drawn from the center of E to these intersection circles represent the diffraction cones. By trigonometry it can be shown that

$$\phi_1,\ \phi_2 = 2\ \tan^{-1}\left[\frac{\sin(\theta'-\theta_2,\theta_1)}{\cos(\theta'-\theta_2,\theta_1) + \lambda/\lambda'}\right] \tag{40}$$

$$\phi_3,\ \phi_4 = 2\ \tan^{-1}\left[\frac{\sin(\theta'-\theta_2,\theta_1)}{\cos(\theta'-\theta_2,\theta_1) - \lambda/\lambda'}\right] \tag{41}$$

where ϕ_1 and ϕ_3 are the diffraction cone angles associated with the original writing beam that was at angle θ_2. Likewise, ϕ_2 and ϕ_4 are associated with the writing beam that was at θ_1. Angle ϕ_3 is not

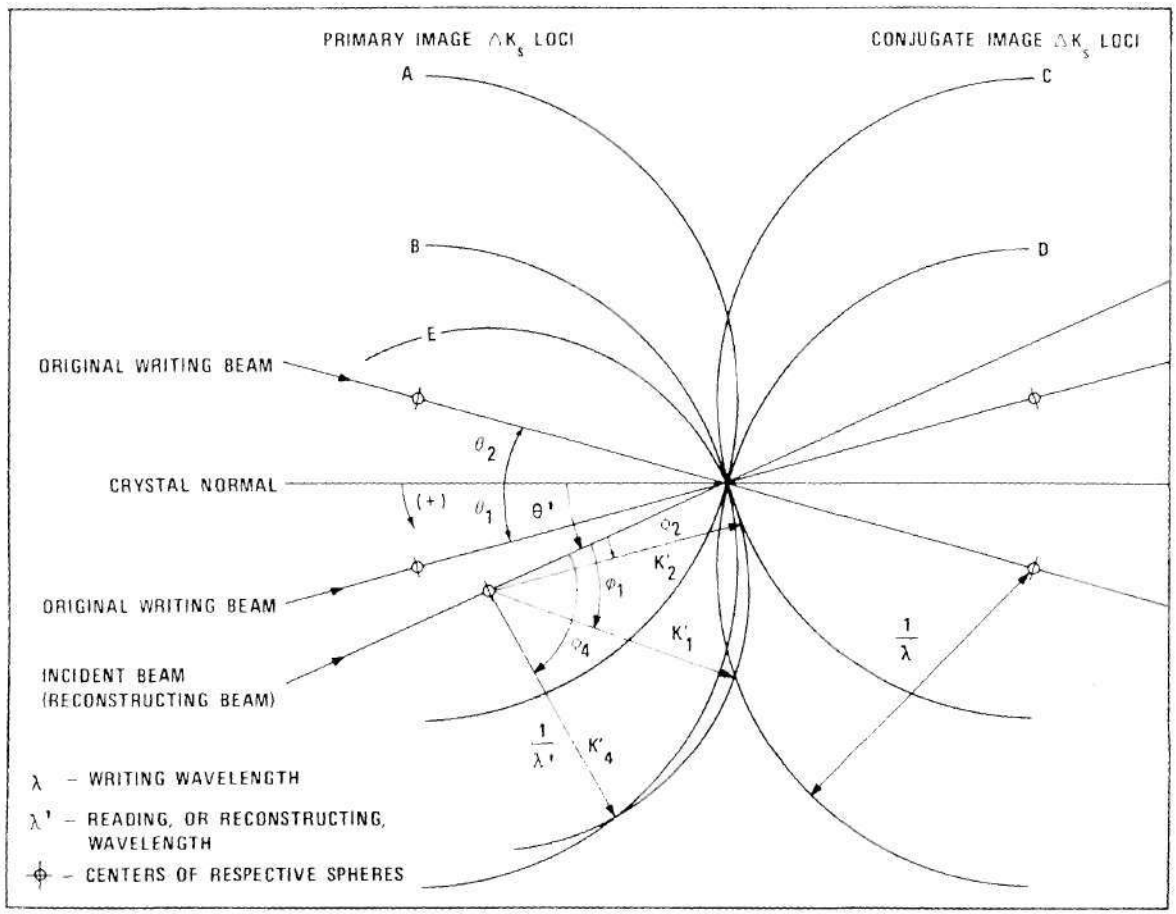

Figure 73. Ewald Sphere Construction Used in Deriving the Relationship Between the Diffraction Cone Angles, ϕ, and the Angle of Incidence, θ'.

shown in Figure 73 because the intersection to which it corresponds (for reconstructing sphere E and primary sphere A) is not pictured. The diffraction cone angles, ϕ_5 and ϕ_6, for the normal incidence single writing beam case are obtained by setting θ_1 and θ_2 equal to zero in the above equations.

$$\phi_5 = \phi_1(\theta_2=0) = \phi_2(\theta_1=0) = 2 \tan^{-1}\left[\frac{\sin\theta'}{\cos\theta'+\lambda/\lambda'}\right] \tag{42}$$

$$\phi_6 = \phi_3(\theta_2=0) = \phi_4(\theta_1=0) = 2 \tan^{-1}\left[\frac{\sin\theta'}{\cos\theta'-\lambda/\lambda'}\right] \tag{43}$$

These equations can be shown to be mathematically identical to Eqs. (3) and (4) in Reference 63, upon appropriate redefinition of angles.

6.3 Results

Equations (40) and (41) are plotted in Fig. 74 as functions of the angle of incidence, θ', for $\theta_1 = +5°$, $\theta_2 = -5°$, $\lambda = 515$ nm, and $\lambda' = 488$ nm, 515 nm, and 633 nm. Experimentally measured values of the cone angle ϕ are also plotted in Fig. 74. These are found to be in excellent agreement with the theoretical predictions. It is seen from Fig. 74 that two rings are visible at all times. These represent the diffraction cones (of angles ϕ_1 and ϕ_2) generated by the intersection of the reconstructing surface with the conjugate writing surfaces. The angles ϕ_3 and ϕ_4 are found to be very sensitive to changes in θ'. Consequently, the corresponding rings are seen only for a very narrow angular range about $\theta' = \theta_1, \theta_2$ at the experimental wavelengths. This may also be seen from Fig. 73 (imagine that θ' varies and observe ϕ_4).

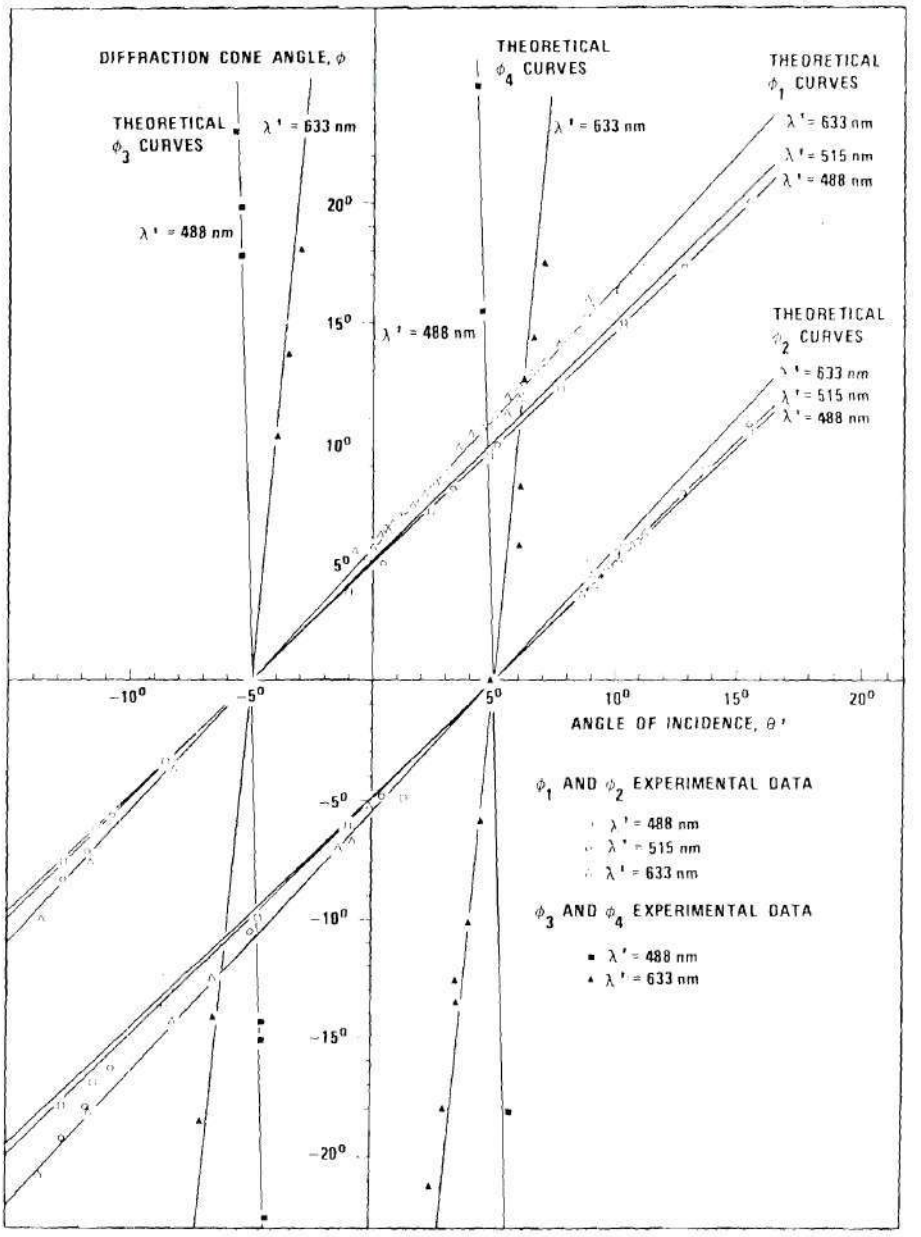

Figure 74. Comparison of Theoretical and Experimental Results for a $LiNbO_3$ Crystal Originally Exposed to Two Intersecting Laser Beams of λ = 515 nm Having Angles of Incidence Equal to +5° and -5° and Subsequently Probed with a Single Low Power Laser Beam of λ' = 488 nm, 515 nm, and 633 nm. The Theoretical Curves are the Same as Those in Figure 75, the Patterns having been Displaced by $\Delta\theta'$ = ±5°.

Equations (42) and (43) for the single exposing beam case at normal incidence (θ_1=0 or θ_2=0) are plotted as functions of the angle of incidence, θ', in Fig. 75 for λ = 515 nm and λ' = 488 nm, 515 nm, and 633 nm. Experimental data for the diffraction cone angle ϕ are also included in Fig. 75. The data are seen to conform very closely to the theoretically predicted values.

6.4 Discussion

The material used in these experiments was a 3.0 mm thick poled single crystal of lithium niobate doped with 0.1 mole percent iron (in the melt). This heavily doped material, which was initially reddish, was oxygen annealed to make it transparent (presumably changing Fe^{2+} to Fe^{3+}). Laser scattering induced holograms were written with a single beam and with two intersecting beams of an argon ion laser operating at λ = 515 nm. Writing exposures to produce a readily observable diffraction cone pattern were typically 1 joule. In the intersecting beam case, the plane wave grating holograms produced had a diffraction efficiency of approximately 20%.

The origin of laser scattering can be quite arbitrary. Surface flaws and bulk imperfections (banding or striae) produced during crystal growth are potential scatterers. The presence of those has been found experimentally to enhance scattering dramatically. Anti-parallel polar domains that can be thermally induced even in poled $LiNbO_3$ crystals have been suggested as possible sources of optical scattering.[65]

The distribution of light energy within the rings contains

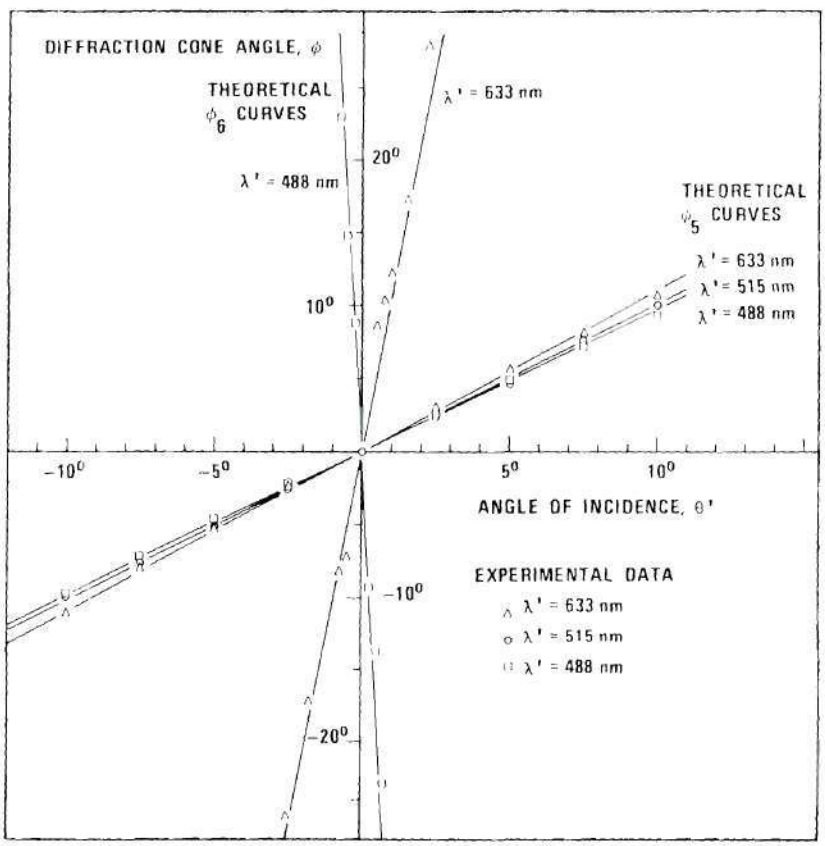

Figure 75. Comparison of Theoretical and Experimental Results for a $LiNbO_3$ Crystal Originally Exposed to a Single Laser Beam of λ = 515 nm at Normal Incidence and Subsequently Probed with a Laser Beam of λ' = 488 nm, 515 nm, and 633 nm.

information about the orientation of the scatterers. In Fig. 71(b), for example, the intensity distribution in the ring indicates that the scatterers are largely vertically oriented. On the contrary, the continuous distribution in Fig. 72 indicates a considerably more isotropic scattering situation.

The presence of diffracted cones of light represents a possible limitation of heavily iron doped lithium niobate for data storage applications because optical power is lost into the scattering induced diffraction cones that could otherwise be used to increase the diffraction efficiency and thus the total bit capacity of the two beam grating hologram. However, it has already been shown by Phillips, Amodei, and Staebler[30] that the scattered light may be erased 1) by illumination with uniform incoherent light, or 2) by writing additional superposed holograms at new angles. In the latter case, scattered light from the previous holograms tends to be erased. Furthermore, these workers found that scattered light intensity initially follows a square law in time (as does $\eta(t)$) and exhibits angular selectivity. All of these observations are consistent with holographically created scattering patterns.

CHAPTER VII

CONCLUSIONS AND RECOMMENDATIONS

7.1 Conclusions

It is shown in this dissertation that the dynamic theory of volume holography qualitatively and, to some degree, quantitatively describes all aspects of experimentally observed thick (phase) hologram terminal characteristics measured in electro-optic crystals such as $LiNbO_3$. That is, the description of the formation (writing), static readout (angular selectivity), and dynamic readout of the hologram are all contained in the dynamic theory formalism. It is believed that no such claim can presently be made by any other theory.

In dynamic theory, the influence of the hologram grating on the electromagnetic fields that produce it is taken into consideration (feedback). Beginning with the wave equation, the governing equations are derived using coupled-wave techniques. Although the dynamic theory is thus, fundamentally, a macroscopic theory, the microphysics of the charge transport processes and the associated driving forces responsible for hologram storage enter the theory in a very important way. The spatial phase difference, ϕ_n, between the refractive index grating and the light grating that formed it is, for example, related to the physical processes (i.e. drift and/or diffusion of photoelectrons) operative during hologram formation. All of the hologram terminal characteristics are very sensitive to the value of ϕ_n.

Therefore, the value of ϕ_n can be determined and valuable information about the microphysics involved can be obtained.

To summarize it is recalled that in Chapter II the model and assumptions of the dynamic theory are presented with the details contained in Appendix A. The dynamic coupled-wave equations have been generalized to allow deviations in readout incident angle and wavelength from the corresponding recording quantities and are given for the E-mode polarization (laboratory case). Additionally, formulas that represent structural features (grating amplitude variation with thickness; grating bending) of the hologram gratings created are presented.

A large number of diverse types of writing, reading, and angular selectivity behavior have been reported in the published literature. In Chapter III, by numerically solving the dynamic coupled-wave equations, it is shown that the dynamic theory qualitatively describes all of these various types of experimental behavior. This indicates the general applicability of the theory to the description of the terminal characteristics of volume holograms.

In Chapter IV, a systematic study of volume hologram behavior is conducted with respect to the parameters that most significantly influence the behavior (i.e. the phase shift (ϕ_n), the absorption coefficients, and the incident beam boundary values). These and the other parameters are selected to have experimentally realistic values. It is shown that the maximum obtainable diffraction efficiency depends on the relative values of

the boundary values R_o and S_o as well as on ϕ_n and α'_o. The maximum diffraction efficiency decreases as ϕ_n increases and the oscillations diminish with increasing ϕ_n. The writing characteristics obtained for $R_o < S_o$ are drastically different from those calculated for $S_o < R_o$ in a manner consistent with the erasure-enhancement effect observed in thick electro-optic holograms. This appears to be in contradiction with a statement by Ninomiya[21] that the intensity ratio of the incident beams does not influence unslanted transmission holograms. It is shown that by judiciously applying unequal boundary values it is possible to compensate partially for loss-induced ($\phi_n = 0°$) grating nonuniformity. Furthermore, the calculations indicate that the grating modulation (peak) amplitude can be significantly nonuniform with thickness and that grating bending and grating phase reversal may occur. These nonuniformities increase with increasing ϕ_n and T. Thus the drop in the maximum diffraction efficiency with increasing ϕ_n can be associated with increasing grating nonuniformities with thickness. In addition, it is found that obliteration of the sidelobes in the angular selectivity pattern is associated with increased grating amplitude nonuniformity while the asymmetry relative to the Bragg angle is associated with grating bending. From a theoretical point of view, it is interesting to note that Kogelnik[66] in analyzing Bragg filtering of structures with nonuniform coupling coefficients and period in the direction of propagation obtains similar sidelobe obliteration (in his reflectivity function) for (linear) nonuniformity in the coupling coefficient and asymetric behavior relative to the Bragg frequency for (quadratic)nonuniformity

in the period. Finally, in Chapter IV, dynamic readout is theoretically studied. It is indicated that the generally erasing action of R-beam readout and the generally enhancing S-beam readout can be understood (at least during initial readout) if the phase shift ϕ_n is considered to be of a single sign ($0° \leq \phi_n \leq 90°$) in these anisotropic materials. The readout behavior is very sensitive to the exposure that was used to form the hologram being read. From the study in Chapter IV it is concluded that under no conditions during recording or readout does the maximum diffraction efficiency exceed $\exp(-2\alpha_o' d/\cos\theta')$.

The experimental work pertinent to this dissertation is discussed in Chapter V. Quantitative comparison of theory and experiment is presented. It is found that the major features of the experimental and theoretical hologram terminal characteristics are strongly correlated. It is believed that hologram aperture effects are responsible for the major deviations. That is, spatially varying beam intensity profiles (as opposed to the theoretical infinite plane waves) and the subsequent distortion of those (due to the hologram being written) are found to give rise to spatially inhomogeneous diffraction efficiency. This causes less efficient light energy coupling between the transmitted and the diffracted beam and thus limits the amplitude of the diffraction efficiency oscillations. Most of the experimental results presented in Chapter V (and much other data not presented) indicate that, usually, $0° \leq \phi_n \lesssim 36°$. Thus, it appears that the electronic transport during hologram formation is dominated by drift in these experiments. However, the contribution of diffusion is still important and cannot, in general, be neglected. Another noteworthy

feature is that the major aspects of the experimental data are described by the theory using a constant exposure sensitivity for a considerable exposure range.

In Chapter VI, the discovery of laser scattering induced holograms in lithium niobate is reported. Light scattered from material inhomogeneities is shown to interfere with the original incident beam(s) and to record scattering holograms. These effects are externally manifested as diffraction, or scattering, rings. An experimental and theoretical description of these phenomena is given.

The interpretation that $\phi_n = 0°$ indicates pure drift and that $\phi_n = 90°$ indicates pure diffusion of electrons has been used throughout this thesis. This is based on the results of theoretical charge transport studies using the assumption of short migration length relative to the grating period. For arbitrary migration lengths these interpretations need to be modified. Experimental conditions in each case dictate the selection of migration length assumptions. The results of this thesis are valid for any migration length but care must be exercised in interpreting these. However, there are strong indications that the short migration length assumption is generally valid in electro-optic crystals.[67]

7.2 Future Research

Future research related to the topic of this dissertation should include measurements of hologram terminal characteristics under conditions more nearly approximating the theoretical model. This involves expanding and collimating the recording and readout

beams to attempt to reduce intensity profile variations and the effects of bounded beams. It is expected that such measurements will give results in closer agreement with the theory. The general problem of aperture effects in volume holography is virtually untreated both theoretically and experimentally.

Another interesting topic is the investigation of recording characteristics and beam-coupling effects in thick electro-optic holograms with respect to externally applied electric fields. It is expected that the hologram-forming electron transport mechanism will be affected by the field. Then ϕ_n and the measured characteristics should vary accordingly. In conjunction with the dynamic theory, this could give valuable information about the physical processes in these crystals under a variety of conditions (e.g. doping concentrations).

The multiple diffracted beam phenomenon mentioned in Sec. 5.6 is of theoretical and experimental interest. In coupled wave studies such as the one presented in this dissertation, only two waves (the first and zeroth orders) are retained in the analysis. When significant other orders are present, a multi-wave analysis is necessary to predict the diffraction behavior of the grating.

APPENDIX A

DERIVATION OF THE DYNAMIC COUPLED-WAVE EQUATIONS FOR THE E-MODE

In this appendix, the dynamic coupled-wave equations that describe the recording and readout of thick hologram gratings are derived. Deviations in the reading angle of incidence and wavelength from the corresponding recording quantities are allowed. Thus, the equations are valid for incident angles that deviate from the Bragg angle. This is an extension of the work of Ninomiya[21] who derived the equations for exact Bragg conditions and H-mode polarization ($\nabla\cdot\overline{E}\equiv 0$). Here, the notation of Ninomiya[21] and the methodology of Kogelnik[7] are adopted.

For the E-mode, the governing wave equation is

$$\nabla^2\overline{E} - \nabla(\nabla\cdot\overline{E}) + K^2\overline{E} = \overline{0}, \tag{A1}$$

where $\overline{E}$ is the total electric field in the material and is assumed to be given by the vector

$$\overline{E}(\overline{r},t) = \overline{R}(\overline{r},t)e^{-j\overline{\rho}\cdot\overline{r}} + \overline{S}(\overline{r},t)e^{-j\overline{\sigma}\cdot\overline{r}} \tag{A2}$$

where $\overline{\rho}$ and $\overline{\sigma}$ are the wave vectors of the reference and signal beams, respectively, and $\overline{r} = (x,y,z)$ using the coordinate system given in Figure 1. In Equation (A2), the factor $\exp(j\omega t)$ has been dropped. The propagation constant is

$$K^2 = (\omega^2/c^2)\epsilon_r - j\omega\mu\sigma_c$$

where $\omega = 2\pi c/\lambda$ is the optical angular frequency, c is the velocity of light, λ is the free-space wavelength, ϵ_r is the relative dielectric constant, μ is the magnetic permeability, and σ_c is the electric conductivity. This can be written as

$$K^2 = \beta^2 - 2j\alpha\beta \tag{A3}$$

where $\beta \equiv 2\pi n/\lambda$, $\alpha \equiv \mu c\sigma_c/2n$, $n = \sqrt{\epsilon_r}$. It is assumed that the local exposure

$$\mathcal{E} = \int_0^T \overline{E}\cdot\overline{E}^* dt$$

induces local changes in the refractive index, n, and absorption, α, as follows:

$$\begin{aligned} n &= n_o(1 + \delta_n) + n_1 \\ \alpha &= \alpha_o(1 + \delta_\alpha) + \alpha_1 \end{aligned} \tag{A4}$$

where n_o and α_o are the constants before exposure, $\delta_n n_o$ and $\delta_\alpha \alpha_o$ are slowly varying spatial changes induced by the exposure, and n_1 and α_1 are the rapidly varying spatial modulations responsible for the holographic diffraction. Using Equations (A4) in Equation (A3) and the assumptions that $n_1 << n$, $\alpha << \beta$, and $\delta_n << 1$, which hold well for many practical photosensitive materials,[21] leads to

$$K^2 = \beta_o^2(1 + 2\delta_n) - 2j\beta_o\alpha_o(1 + \delta_\alpha) + 2\beta_o\Gamma \tag{A5}$$

where $\Gamma = 2\pi n_1/\lambda - j\alpha_1$ is the coupling coefficient and $\beta_o = 2\pi n_o/\lambda$.

For the present case, the index changes are taken to be (see Section 2.3)

$$\delta_n n_o + n_1 = a\int_o^T \bar{E}\cdot\bar{E}^* dt.$$

Letting $\bar{R} = R\hat{r}$, $\bar{S} = S\hat{s}$, with $\hat{r}\cdot\hat{r} = \hat{s}\cdot\hat{s} = 1$, and using Equation (A2) yields

$$\delta_n n_o + n_1 = a\int_o^T [RR^* + SS^* + RS^*(\hat{r}\cdot\hat{s})e^{j(\bar{\sigma} - \bar{\rho})\cdot\bar{r}}$$

$$+ SR^*(\hat{r}\cdot\hat{s})e^{j(\bar{\rho} - \bar{\sigma})\cdot\bar{r}}]dt.$$

The complex wave amplitudes, S and R, are assumed to vary with $\mathbf{z}$ and t only.

The following identifications are now made.

$$\delta_n n_o = a\int_o^T (RR^* + SS^*)dt \tag{A6}$$

and

$$n_1 = a(\hat{r}\cdot\hat{s})\int_o^T [RS^*e^{j(\bar{\sigma} - \bar{\rho})\cdot\bar{r}} + SR^*e^{j(\bar{\rho} - \bar{\sigma})\cdot\bar{r}}]dt$$

$$= 2a(\hat{r}\cdot\hat{s})\int_o^T |RS^*| \cos\{(\bar{\sigma} - \bar{\rho})\cdot\bar{r} + \xi + \phi_n\}dt$$

$$= a\,(\hat{r}\cdot\hat{s})\int_o^T [RS^* e^{j\{(\bar{\sigma} - \bar{\rho})\cdot\bar{r} + \phi_n\}} + SR^* e^{j\{(\bar{\rho} - \bar{\sigma})\cdot\bar{r} - \phi_n\}}]dt, \qquad (A7)$$

where $\cos\xi = \mathrm{Re}\{RS^*\}/|RS^*|$, and where ϕ_n, the phase difference that can exist between the interference pattern of the waves and the resultant refractive index change,[20] has been included. Similar expressions hold for $\delta_\alpha\alpha_o$ and α_1 with a replaced by b and ϕ_n replaced by ϕ_α. The coupling coefficient is then found to be

$$\Gamma = (\hat{r}\cdot\hat{s})\Gamma_1 e^{j(\bar{\sigma} - \bar{\rho})\cdot\bar{r}} + (\hat{r}\cdot\hat{s})\Gamma_2 e^{j(\bar{\rho} - \bar{\sigma})\cdot\bar{r}} \qquad (A8)$$

where

$$\Gamma_1 = (\frac{2\pi}{\lambda}\, a e^{j\phi_n} - jbe^{j\phi_\alpha})\int_o^T RS^*dt$$

and

$$\Gamma_2 = (\frac{2\pi}{\lambda}\, a e^{-j\phi_n} - jbe^{-j\phi_\alpha})\int_o^T SR^*dt.$$

The terms entering Equation (A1) are now computed. First,

$$\nabla^2\bar{E} = \nabla^2(\bar{R}e^{-j\bar{\rho}\cdot\bar{r}} + \bar{S}e^{-j\bar{\sigma}\cdot\bar{r}})$$

$$= \bar{R}(-\rho_x^2)e^{-j\bar{\rho}\cdot\bar{r}} + \bar{S}(-\sigma_x^2)e^{-j\bar{\sigma}\cdot\bar{r}}$$

$$+ \left(\frac{\partial^2\bar{S}}{\partial z^2} - 2j\sigma_z\frac{\partial\bar{S}}{\partial z} - \sigma_z^2\bar{S}\right)e^{-j\bar{\sigma}\cdot\bar{r}}$$

$$+ \left(\frac{\partial^2\bar{R}}{\partial z^2} - 2j\rho_z\frac{\partial\bar{R}}{\partial z} - \rho_z^2\bar{R}\right)e^{-j\bar{\rho}\cdot\bar{r}}. \qquad \text{(A9)}$$

Next,

$$\nabla\cdot\bar{E} = \frac{\partial R_z}{\partial z}e^{-j\bar{\rho}\cdot\bar{r}} + \frac{\partial S_z}{\partial z}e^{-j\bar{\sigma}\cdot\bar{r}},$$

which results because $\bar{\rho}\cdot\bar{R} = 0$ and $\bar{\sigma}\cdot\bar{S} = 0$ and where $\hat{z}\cdot\bar{R} = R_z$ and $\hat{z}\cdot\bar{S} = S_z$. Finally,

$$\nabla(\nabla\cdot\bar{E}) = -je^{-j\bar{\rho}\cdot\bar{r}}\frac{\partial R_z}{\partial z}\bar{\rho} - je^{-j\bar{\sigma}\cdot\bar{r}}\frac{\partial S_z}{\partial z}\bar{\sigma}$$

$$+ \frac{\partial^2 S_z}{\partial z^2}e^{-j\bar{\sigma}\cdot\bar{r}}\hat{z} + \frac{\partial^2 R_z}{\partial z^2}e^{-j\bar{\rho}\cdot\bar{r}}\hat{z}. \qquad \text{(A10)}$$

Equations (A5), (A8), (A9), and (A10) are now substituted into Equation (A1). Waves in the directions $\bar{\sigma} - 2\bar{\rho}$ and $\bar{\rho} - 2\bar{\sigma}$ are neglected. This is allowed because these waves do not propagate according to the Bragg condition.[7] Second derivatives are also neglected, which is permissible for slow energy interchange between the R and S waves and

slow absorption; that is, the variations of R and S with z are not very rapid, which is usually the case in practice.[7] Collecting terms in $\exp(-j\bar{\sigma}\cdot\bar{r})$ and in $\exp(-j\bar{\rho}\cdot\bar{r})$ then yields

$$-2j\rho_z \frac{\partial \bar{R}}{\partial z} + j \frac{\partial R_z}{\partial z} \bar{\rho} + [2\beta_o^2 \delta_n - 2j\beta_o \alpha_o (1 + \delta_\alpha)]\bar{R}$$

$$+ 2\beta_o \Gamma_1 \bar{S}(\hat{r}\cdot\hat{s}) = \bar{0}$$

and

$$-2j\sigma_z \frac{\partial \bar{S}}{\partial z} + j \frac{\partial S_z}{\partial z} \bar{\sigma} + (\beta_o^2 - \sigma^2)\bar{S}$$

$$+ [2\beta_o^2 \delta_n - 2j\beta_o \alpha_o (1 + \delta_\alpha)]\bar{S} + 2\beta_o \Gamma_2 \bar{R}(\hat{r}\cdot\hat{s}) = \bar{0},$$

where $\rho^2 = \rho_x^2 + \rho_z^2 = \beta_o^2$ but $\sigma^2 = \sigma_x^2 + \sigma_z^2 \neq \beta_o^2$ in general. Using $\bar{R} = R\hat{r}$ and $\bar{S} = S\hat{s}$, the first equation is vectorially multiplied (dot product) by $\hat{r}$ and the second by $\hat{s}$. The following equations are then obtained:

$$\frac{\rho_z}{\beta_o} \frac{\partial R}{\partial z} + [j\beta_o \delta_n + \alpha_o (1 + \delta_\alpha)]R = -j\Gamma_1 S(\hat{r}\cdot\hat{s})^2$$

and

$$\frac{\sigma_z}{\beta_o} \frac{\partial S}{\partial z} + j\left(\frac{\beta_o^2 - \sigma^2}{2\beta_o}\right)S + [j\beta_o \delta_n + \alpha_o (1 + \delta_\alpha)]S = -j\Gamma_2 R(\hat{r}\cdot\hat{s})^2.$$

Computing and defining,

$$j\beta_o\delta_n + \alpha_o(1 + \delta_\alpha) = (j\frac{2\pi a}{\lambda} + b)\int_o^T (RR^* + SS^*)dt + \alpha_o = \gamma.$$

Also, $\sigma_z = \rho_z = \beta_c\cos\theta$ for the unslanted gratings considered presently. Therefore, finally,

$$\cos\theta \frac{\partial R}{\partial z} + \gamma R = -j\Gamma_1 S(\hat{r}\cdot\hat{s})^2 \tag{A11}$$

and

$$\cos\theta \frac{\partial S}{\partial z} + (\gamma + j\vartheta)S = -j\Gamma_2 R(\hat{r}\cdot\hat{s})^2, \tag{A12}$$

where $\vartheta = (\beta_o^2 - \sigma'^2)/2\beta_o$ and where σ' is the magnitude of the propagation vector of the diffracted wave upon reading. Equations (A11) and (A12) are the dynamic coupled-wave equations for the E-mode. For exact Bragg conditions ($\sigma' = \sigma = \beta_o$), $\vartheta = 0$, and if $\hat{r}\cdot\hat{s} = 1$ (i.e. H-mode), this reduces to Ninomiya's Equations (21) as it should.

For reading, $\bar{\sigma}$ and $\bar{\rho}$ become the corresponding reading quantities, i.e. $\bar{\sigma}'$ and $\bar{\rho}'$. Thus when considering the readout process, it is necessary to let $\beta_o \to \beta_o'$, $\cos\theta \to \cos\theta'$, but $\hat{r}\cdot\hat{s} = \cos 2\theta$, with θ the original writing angle, remains unchanged.

APPENDIX B

ANALYTICAL SOLUTION OF THE DYNAMIC COUPLED-WAVE EQUATIONS FOR SHORT WRITING TIME

The dynamic hologram theory introduces the proportionality coefficient, a, between the refractive index change and the exposure that produced the change. This coefficient, the exposure sensitivity for the refractive index changes, is unknown since the index changes resulting from a given exposure are not directly measured in this work. It is, therefore, desirable to relate this coefficient to an easily measurable quantity from which its value can be deduced. In this appendix, it is shown that the exposure sensitivity can be obtained from a measurement of diffraction efficiency at the very beginning of recording (i.e. a low exposure hologram). This is because in the short writing time limit ($T \to 0$), it is possible to obtain analytical solutions of the dynamic coupled-wave equations from which an expression for diffraction efficiency containing the exposure sensitivity can be calculated. It is the purpose of this appendix to derive this useful expression.

From the full numerical solutions of the dynamic coupled-wave equations it has been noted that, initially (small T), during writing, the η vs.t curves coincide for all $0^{\circ} \leq \phi_n \leq 90^{\circ}$ (see Figure 30). The convenient choice $\phi_n = 0°$ can thus be used in the present analysis without introducing significant errors. Reading at the Bragg angle also simplifies the task.

In what follows, an unslanted, lossy, phase hologram (b = 0) is written. From the solutions of the writing coupled-wave equations, the coefficients that represent the exposure-induced material changes are computed. These are then substituted into the reading equations whose solutions yield the diffraction efficiency expression sought. This procedure exemplifies the approach that must be sequentially employed in the general numerical solution of the full dynamic coupled-wave equations for small time intervals.

Writing

The starting point is the normalized set of equations:

$$\cos\theta \frac{\partial R}{\partial z} + d\gamma R = -j\Gamma_1 S d\cos^2 2\theta \tag{B1}$$

and

$$\cos\theta \frac{\partial S}{\partial z} + d\gamma S = -j\Gamma_2 R d\cos^2 2\theta, \tag{B2}$$

$$0 \leq z \leq 1,$$

where, approximately (small T),

$$\gamma = j \frac{2\pi a}{\lambda} (RR^* + SS^*)T + \alpha_o$$

and

$$\Gamma_1 = \frac{2\pi a}{\lambda} RS^*T = \Gamma_2^* ,$$

where ϕ_n has been set to zero. It is helpful to note that the differential equation that governs power flow in the present model is

$$\cos\theta \frac{\partial}{\partial z} (RR^* + SS^*) + d(\gamma + \gamma^*)(RR^* + SS^*) = 0. \tag{B3}$$

Since $\gamma + \gamma^* = 2\alpha_o$, this equation has the solution

$$RR^* + SS^* = C_o e^{-2d\alpha_o z/\cos\theta} , \tag{B4}$$

where $C_o = R_o^2 + S_o^2$ because the boundary conditions for writing are $R(0) = R_o$ and $S(0) = S_o$. Substituting for γ and Γ_1 in Equations (B1) and (B2) and using Equation (B4) leads to

$$\frac{\partial R}{\partial z} + ja_1 e^{-2a_2 z} R + a_2 R = ja_3 (RR^* - C_o e^{-2a_2 z}) R \tag{B5}$$

and

$$\frac{\partial S}{\partial z} + ja_1 e^{-2a_2 z} S + a_2 S = ja_3 (SS^* - C_o e^{-2a_2 z}) S \tag{B6}$$

where

$$a_1 \equiv 2\pi a d T C_o / \lambda \cos\theta ,$$

$$a_2 \equiv \alpha_o d / \cos\theta ,$$

and

$$a_3 \equiv 2\pi adT\cos^2 2\theta/\lambda\cos\theta .$$

It is seen that R-S decoupling of the original equations has been accomplished through the use of the power flow equation. In addition, the equations are formally equivalent.

To solve, say, Equation (B5), let

$$R = R_1(z)e^{jr(z)}$$

with R_1 and r purely real. Upon substitution and separation of the real and imaginary parts, the following equations emerge.

$$\frac{\partial R_1}{\partial z} + a_2 R_1 = 0 \tag{B7}$$

and

$$\frac{\partial r}{\partial z} + a_1 e^{-2a_2 z} = a_3(R_1^2 - C_o e^{-2a_2 z}). \tag{B8}$$

Since r(0) = 0, the solutions are

$$R_1 = R_o e^{-a_2 z} \tag{B9}$$

and

$$x = (a_1 + a_3 S_o^2)(e^{-2a_2 z} - 1)/2a_2 \tag{B10}$$

Therefore, the solutions of the writing equations are

$$R(z) = R_o e^{-a_2 z} e^{j(a_1 + a_3 S_o^2)(e^{-2a_2 z} - 1)/2a_2} \tag{B11}$$

and

$$S(z) = S_o e^{-a_2 z} e^{j(a_1 + a_3 R_o^2)(e^{-2a_2 z} - 1)/2a_2}. \tag{B12}$$

Readout

The (static) readout at time T of the dynamically produced hologram is governed by the equations

$$\cos\theta' \frac{\partial R}{\partial z} + d\gamma' R = -j\Gamma_1' S d\cos^2 2\theta \tag{B13}$$

and

$$\cos\theta' \frac{\partial S}{\partial z} + d(\gamma' + j\vartheta) S = -j\Gamma_2' R d\cos^2 2\theta, \tag{B14}$$

with

$$0 \leq z \leq 1,$$

where the coefficients representing the writing-induced material

variations,

$$\gamma' = j \frac{2\pi a}{\lambda'} (RR^* + SS^*)T + \alpha_o',$$

and

$$\Gamma_1' = \frac{2\pi a}{\lambda'} RS^*T = \Gamma_2'^*,$$

are fixed by the solutions, Equations (B11) and (B12), of the previous writing equations. Primed quantities represent the values associated with the readout process. The readout beam is assumed to be at its Bragg angle. Thus, $\vartheta = 0$.

Using Equations (B11) and (B12) yields

$$\gamma' = j \frac{2\pi a}{\lambda'} TC_o e^{-2a_2 z} + \alpha_o'$$

and

$$\Gamma_1' = \frac{2\pi a}{\lambda'} TR_o S_o e^{-2a_2 z} e^{j(S_o^2 - R_o^2)a_3 (e^{-2a_2 z} - 1)/2a_2}.$$

For the common laboratory condition $S_o = R_o$, Γ_1' is particularly simple. Note also that the coefficient a_3 is typically two or three orders of magnitude smaller than $2a_2$, which justifies neglecting the imaginary exponential term even when R_o and S_o are not exactly equal. Thus, it is reasonable to use

$$\Gamma_1' = \frac{2\pi a}{\lambda'} TR_o S_o e^{-2a_2 z}.$$

These results for γ' and Γ_1' are next substituted into Equations (B13) and (B14). This leads to

$$\frac{\partial R}{\partial z} + (jb_1 e^{-2a_2 z} + b_2)R = -jb_3 e^{-2a_2 z} S \tag{B15}$$

and

$$\frac{\partial S}{\partial z} + (jb_1 e^{-2a_2 z} + b_2)S = -jb_3 e^{-2a_2 z} R, \tag{B16}$$

where

$$b_1 \equiv 2\pi adTC_o/\lambda'\cos\theta',$$

$$b_2 \equiv \alpha_o' d/\cos\theta',$$

and

$$b_3 \equiv 2\pi adTR_o S_o \cos^2 2\theta/\lambda'\cos\theta'.$$

To solve Equations (B15) and (B16), it is convenient to effect the change of variable

$$W \equiv e^{-2a_2 z}/2a_2.$$

Then,

$$\frac{\partial f}{\partial W} = - \frac{\partial f}{\partial z} e^{2a_2 z},$$

where f is any function of z. The equations are thus transformed into

$$\frac{\partial R}{\partial W} - pR = jb_3 S \tag{B17}$$

and

$$\frac{\partial S}{\partial W} - pS = jb_3 R \tag{B18}$$

where $p = p(W) \equiv jb_1 + b_2/2a_2 W$. Substitution of

$$R = R_2 e^{\int p dW}$$

and

$$S = S_2 e^{\int p dW}$$

into Equations (B17) and (B18) gives

$$\frac{\partial R_2}{\partial W} = jb_3 S_2 \tag{B19}$$

and

$$\frac{\partial S_2}{\partial W} = jb_3 R_2. \tag{B20}$$

These are then combined into

$$\frac{\partial^2 S_2}{\partial W^2} + b_3^2 S_2 = 0 \tag{B21}$$

which has the solution

$$S_2(W) = A\cos b_3 W + B\sin b_3 W \tag{B22}$$

where A and B are to be found from the boundary conditions. The proper boundary conditions for S_2 and R_2 must be derived from those for S and R. It is given for reading that

$$R(z = 0) = R(W = 1/2a_2) = R'_o$$

and

$$S(z = 0) = S(W = 1/2a_2) = 0.$$

With

$$R_2 = Re^{-\int p dW}$$

and

$$S_2 = Se^{-\int pdW},$$

where $\int pdW = jb_1W + \frac{b_2}{2a_2}\ell nW$, it is found that

$$S_2(W = 1/2a_2) = 0$$

and

$$\frac{\partial S_2}{\partial z}(W = 1/2a_2) = jb_3R'_o e^{-(jb_1 + b_2\ell n(1/2a_2))/2a_2}$$

which are sufficient to evaluate A and B. The result is

$$B = jR'_o\cos(b_3/2a_2)e^{-(jb_1 + b_2\ell n(1/2a_2))/2a_2}$$

and

$$A = -B\tan(b_3/2a_2).$$

Therefore, using Equation (B22),

$$S_2 = jR'_o\sin(b_3W - b_3/2a_2)e^{-(jb_1 + b_2\ell n(1/2a_2))/2a_2}. \qquad \text{(B23)}$$

Diffraction efficiency is defined by

$$\eta = S(z = 1)S^*(z = 1)/R'^2_o.$$

With $W = e^{-2a_2}/2a_2$ at $z = 1$, this corresponds to

$$\eta = S_2 e^{\int pdW} S_2^* (e^{\int pdW})^* / R_o'^2$$

evaluated at $W = e^{-2a_2}/2a_2$. Using the above results then gives

$$\eta = e^{-2b_2} \sin^2[b_3(1 - e^{-2a_2})/2a_2], \tag{B24}$$

which is the expression sought. Note that in the limit $\alpha_o \to 0$ (for which uniform gratings are created on writing with $\phi_n = 0°$), the result Equation (B24) corresponds to Kogelnik's result for lossy dielectric gratings.[7] His n_1 corresponds to $2a\cos 2\theta R_o S_o T$ in the present work which is consistent with Equation (A7) in Appendix A. Equation (B24) may be solved to give the initial value of the refractive-index exposure sensitivity, a. The result is

$$a = \{\alpha_o \lambda' \cos\theta' \sin^{-1}[\eta \exp(2\alpha_o' d/\cos\theta')]^{\frac{1}{2}}\}/$$

$$\{\pi T R_o S_o \cos\theta \cos^2 2\theta [1 - \exp(-2\alpha_o d/\cos\theta)]\}. \tag{B25}$$

APPENDIX C

DIFFRACTED WAVE VECTOR MAGNITUDE

Upon recording, the interference of the signal and reference waves that have wave vectors $\bar{\sigma}$ and $\bar{\rho}$, respectively, creates a periodic grating with grating vector $(\bar{\sigma} - \bar{\rho})$ (see Equation (A7) in Appendix A). When a readout wave of wave vector $\bar{\rho}'$ is incident upon this grating, the signal wave of wave vector $\bar{\sigma}'$ is reconstructed via diffraction according to Bragg's Law,

$$\bar{\rho}' + (\bar{\sigma} - \bar{\rho}) = \bar{\sigma}'. \tag{C1}$$

Since the vectors $\bar{\rho}$, $\bar{\sigma}$, and $\bar{\rho}'$ are known, $\bar{\sigma}'$ is given by Equation (C1). Thus (see Figure 1),

$$\bar{\sigma}' = \beta_o' \cos\theta' \hat{z} + \beta_o' \sin\theta' \hat{x} - 2\beta_o \sin\theta \hat{x}.$$

The magnitude of $\bar{\sigma}'$ enters the dynamic hologram theory and is, therefore, of interest. It is given by

$$\sigma' = (\beta_o'^2 - 4\beta_o\beta_o' \sin\theta \sin\theta' + 4\beta_o^2 \sin^2\theta)^{1/2}. \tag{C2}$$

It is noted that $\sigma' = \beta_o' = \beta_o = \sigma$ if and only if $\theta' = \theta$ and $\lambda' = \lambda$. For readout with the S beam, the magnitude of the wave vector of the diffracted wave, ρ', is also given by Equation (C2).

APPENDIX D

DETERMINATION OF C-AXIS POLARITY FOR LITHIUM NIOBATE CRYSTALS

According to IEEE convention, the +c-face of the crystal becomes negative upon compression.[68] Another way to specify the +c-face is to perform a pyroelectric experiment. The +c-face becomes positive upon cooling.[46,69] Both of these criteria have been used in the present work and are found to be mutually consistent. However, the first test is easier to apply and is used to routinely determine the c-axis polarity for the lithium niobate crystals used in the experiments. These crystals exhibit the piezoelectric effect along the b- and c-axes but not along the a-axis. In the present case, the laser beams enter the material through the b-face during holography experimentation.

A small vise with insulated jaws supporting aluminum electrodes is used to supply the compression. The crystal is placed between the electrodes with the suspected +c-face up against one electrode. A 100 ohm resistor is connected across the crystal to reduce the source resistance. A nanovolt null detector (Keithley Model 147) is used to measure the voltage pulse developed across the resistor when pressure is applied to the crystal with the vise. If the positive terminal of the meter input lead happens to be at the +c-face, a negative deflection is observed on compression. An equal and opposite deflection is obtained when the pressure is released. The deflection is, typically, around

0.2 μV. To check the results, the leads are reversed and the test is repeated. If compression is applied along the a-axis, considerably smaller, rather erratic deflections are seen. The axis not exhibiting the piezoelectric effect (a-axis) is thus clearly distinguished from the c-axis.

APPENDIX E

NUMERICAL ALGORITHM

To solve the differential equations encountered in this thesis, a fourth-order Runge-Kutta method is used. The equations to be solved have the form

$$\frac{\partial R}{\partial z} = f(R(z),S(z))$$

and

$$\frac{\partial S}{\partial z} = g(R(z),S(z))$$

with the given boundary conditions $R(z_o) = R_o$ and $S(z_o) = S_o$. The numerical solution is obtained using the following algorithm[70]

$$R_{i+1} = R_i + (k_1 + 2k_2 + 2k_3 + k_4)/6$$

$$S_{i+1} = S_i + (q_1 + 2q_2 + 2q_3 + q_4)/6$$

where

$$k_1 = (\Delta z)\, f(R_i,S_i)$$

$$q_1 = (\Delta z)g(R_i, S_i),$$

$$k_2 = (\Delta z)f(R_i + k_1/2,\ S_i + q_1/2),$$

$$q_2 = (\Delta z)g(R_i + k_1/2,\ S_i + q_1/2),$$

$$k_3 = (\Delta z)f(R_i + k_2/2,\ S_i + q_2/2),$$

$$q_3 = (\Delta z)g(R_i + k_2/2,\ S_i + q_2/2),$$

$$k_4 = (\Delta z)f(R_i + k_3,\ S_i + q_3),$$

and

$$q_4 = (\Delta z)g(R_i + k_3,\ S_i + q_3),$$

where i is an index and Δz the step size. The iteration is initialized using the given boundary conditions and is continued until the range of the independent variable, z, has been covered.

BIBLIOGRAPHY

1. D. Gabor, "A New Microscopic Principle," Nature, vol. 161, pp. 777-778, May 1948.

2. E. N. Leith and J. Upatnieks, "Reconstructed Wavefronts and Communication Theory," Journal of the Optical Society of America, vol. 52, pp. 1123-1130, October 1962.

3. E. N. Leith and J. Upatnieks, "Wavefront Reconstruction with Continuous-Tone Objects," Journal of the Optical Society of America, vol. 53, pp. 1377-1381, December 1963.

4. E. N. Leith and J. Upatnieks, "Wavefront Reconstruction with Diffused Illumination and Three-Dimensional Objects," Journal of the Optical Society of America, vol. 54, pp. 1295-1301, November 1964.

5. Y. N. Denisyuk, "On the Reproduction of the Optical Properties of an Object by the Wave Field of Its Scattered Radiation," Optics and Spectroscopy, vol. 15, pp. 279-284, October 1963.

6. P. J. van Heerden, "Theory of Optical Information Storage in Solids," Applied Optics, vol. 2, pp. 393-400, April 1963.

7. H. Kogelnik, "Coupled-Wave Theory for Thick Hologram Gratings," The Bell System Technical Journal, vol. 48, No. 9, pp. 2909-2947, November 1969.

8. M. R. B. Forshaw, "Thick Holograms: A Survey," Optics and Laser Technology, vol. 6, pp. 28-35, February 1974.

9. B. H. Crawford, "The Preparation of Ultra-Fine Grain Photographic Emulsions," Journal of Scientific Instruments, vol. 31, pp. 333-335, September 1954.

10. J. N. Latta and R. C. Fairchild, "Two-Element Hologram Telescope Lens," Journal of the Optical Society of America, vol. 63, p. 487, March 1973.

11. R. Shubert and J. H. Harris, "Optical Guided-Wave Focusing and Diffraction," Journal of the Optical Society of America, vol. 61, pp. 154-161, February 1971.

12. H. Kogelnik and C. V. Shank, "Stimulated Emission in a Periodic Structure," Applied Physics Letters, vol. 18, pp. 152-154, February 15, 1971.

13. H. Kogelnik and T. P. Sosnowski, "Holographic Thin-Film Couplers," The Bell System Technical Journal, vol. 49, pp. 1602-1608, September 1970.

14. M. L. Dakss, L. Kuhn, P. F. Heidrich, and B. A. Stott, "Grating Coupler for Efficient Excitation of Optical Guided Waves in Thin Films," Applied Physics Letters, vol. 16, pp. 523-525, June 15, 1970.

15. J. M. Hammer, "Digital Electro-Optic Grating Deflector and Modulator," Applied Physics Letters, vol. 18, pp. 147-149, February 15, 1971.

16. K. S. Pennington and L. H. Lin, "Multicolor Wavefront Reconstruction," Applied Physics Letters, vol. 7, pp. 56-57, August 1, 1965.

17. G. W. Stroke and A. E. Labeyrie, "White-Light Reconstruction of Holographic Images Using the Lippmann-Bragg Diffraction Effect," Physics Letters, vol. 20, pp. 368-370, March 1966.

18. T. K. Gaylord, "Optical Memories: Filling the Storage Gap," Optical Spectra, vol. 8, pp. 29-34, June 1974.

19. C. B. Burckhardt, "Diffraction of a Plane Wave at a Sinusoidally Stratified Dielectric Grating," Journal of the Optical Society of America, vol. 56, pp. 1502-1509, November 1966.

20. D. L. Staebler and J. J. Amodei, "Coupled-Wave Analysis of Holographic Storage in $LiNbO_3$," Journal of Applied Physics, vol. 43, pp. 1042-1049, March 1972.

21. Y. Ninomiya, "Recording Characteristics of Volume Holograms," Journal of the Optical Society of America, vol. 63, pp. 1124-1130, September 1973.

22. P. Phariseau, "On the Diffraction of Light by Progressive Supersonic Waves," Proceeding of the Indian Academy of Science, vol. A44, pp. 165-170, October 1956.

23. S. F. Su and T. K. Gaylord, "Calculation of Arbitrary-Order Diffraction Efficiencies of Thick Grating with Arbitrary Grating Shape," Journal of the Optical Society of America, vol. 65, pp. 59-64, January 1975.

24. D. Kermisch, "Efficiency of Photochromic Gratings," Journal of the Optical Society of America, vol. 61, pp. 1202-1206, September 1971.

25. D. Kermisch, "Nonuniform Sinusoidally Modulated Dielectric Gratings," Journal of the Optical Society of America, vol. 59, pp. 1409-1414, November 1969.

26. N. Uchida, "Calculation of Diffraction Efficiency in Hologram Gratings Attenuated along the Direction Perpendicular to the Grating Vector," Journal of the Optical Society of America, vol. 63, pp. 280-287, January 1973.

27. S. F. Su, "Determination of Grating Shape and Physical Mechanisms in Lithium Niobate Holographic Recording," Ph.D. Thesis, Georgia Institute of Technology, 1976.

28. T. K. Gaylord, T. A. Rabson, and F. K. Tittel, "Optically Erasable and Rewritable Solid-State Holograms," Applied Physics Letters, vol. 20, pp. 47-49, January 1, 1972.

29. F. Micheron and G. Bismuth, "Holographic Optical Storage Using Electrical Control of Fixation and Erasure in Ferroelectrics," Digest of Technical Papers, 1972 IEEE International Solid-State Circuits Conference, pp. 104-105, February 1972.

30. W. Phillips, J. J. Amodei, and D. L. Staebler, "Optical and Holographic Storage Properties of Transition Metal Doped Lithium Niobate," RCA Review, vol. 33, pp. 94-109, March 1972.

31. L. H. Lin, "Holographic Measurements of Optically Induced Refractive Index Inhomogeneities in Bismuth Titanate," Proceedings of the IEEE, vol. 57, pp. 252-253, February 1969.

32. F. S. Chen, J. T. LaMacchia and D. B. Fraser, "Holographic Storage in Lithium Niobate," Applied Physics Letters, vol. 13, pp. 223-225, October 1, 1968.

33. J. J. Amodei, W. Phillips, and D. L. Staebler, "Improved Electro-optic Materials and Fixing Techniques for Holographic Recording," Applied Optics, vol. 11, pp. 390-396, February 1972.

34. A. Ishida, O. Mikami, S. Miyazawa, and M. Sumi, "Rh-Doped $LiNbO_3$ as an Improved New Material for Reversible Holographic Storage," Applied Physics Letters, vol. 21, pp. 192-193, September 1, 1972.

35. R. W. Damon, D. H. McMahon, and J. B. Thaxter, "Materials for Optical Memories," Electro-Optical Systems Design, vol. 2, pp. 68-77, August 1970.

36. F. Micheron and G. Bismuth, "Field and Time Thresholds for the Electrical Fixation of Holograms Recorded in $(Sr_{0.75}Ba_{0.25})Nb_2O_6$ Crystals," Applied Physics Letters, vol. 23, pp. 71-72, July 15, 1973.

37. T. A. Shankoff, "Phase Holograms in Dichromated Gelatin," Applied Optics, vol. 7, pp. 2101-2105, October 1968.

38. W. Phillips and D. L. Staebler, "Control of the Fe^{2+} Concentration in Iron-Doped Lithium Niobate," Journal of Electronic Materials, vol. 3, pp. 601-617, 1974.

39. D. L. Staebler and W. Phillips, "Fe-Doped $LiNbO_3$ for Read-Write Applications," Applied Optics, vol. 13, pp. 788-794, April 1974.

40. J. P. Huignard, J. P. Herriau, and F. Micheron, "Coherent Selective Erasure of Superimposed Volume Holograms in $LiNbO_3$," Applied Physics Letters, vol. 26, pp. 256-258, March 1, 1975.

41. D. L. Staebler, W. J. Burke, W. Phillips, and J. J. Amodei, "Multiple Storage and Erasure of Fixed Holograms in Fe-Doped $LiNbO_3$," Applied Physics Letters, vol. 26, pp. 182-184, February 15, 1975.

42. J. J. Amodei, D. L. Staebler, and A. W. Stephens, "Holographic Storage in Doped Barium Sodium Niobate ($Ba_2NaNb_5O_{15}$)," Applied Physics Letters, vol. 18, pp. 507-509, June 1, 1971.

43. F. Micheron and G. Bismuth, "Electrical Control in Photo-Ferroelectrics for Optical Storage," Digest of Technical Papers, Topical Meeting on Optical Storage of Digital Data, pp. MB3-1-MB3-4, March 19-21, 1973.

44. T. K. Gaylord, T. A. Rabson, F. K. Tittel, and C. R. Quick, "Pulsed Writing of Solid State Holograms," Applied Optics, vol. 12, pp. 414-415, February 1973.

45. R. L. Townsend and J. T. LaMacchia, "Optically Induced Refractive Index Changes in $BaTiO_3$," Journal of Applied Physics, vol. 41, pp. 5188-5192, December 1970.

46. J. J. Amodei and D. L. Staebler, "Holographic Pattern Fixing in Electro-Optic Crystals," Applied Physics Letters, vol. 18, pp. 540-542, June 15, 1971.

47. D. L. Staebler and J. J. Amodei, "Thermally Fixed Holograms in $LiNbO_3$," Ferroelectrics, vol. 3, pp. 107-113, 1972.

48. T. K. Gaylord, T. A. Rabson, F. K. Tittel, and C. R. Quick, "Self-Enhancement of $LiNbO_3$ Holograms," Journal of Applied Physics, vol. 44, pp. 896-897, February 1973.

49. E. N. Leith, A. Kozma, J. Upatnieks, J. Marks, and N. Massey, "Holographic Data Storage in Three-Dimensional Media," Applied Optics, vol. 5, pp. 1303-1311, August 1966.

50. K. Biedermann, S. I. Ragnarsson, and P. Komlos, "Volume Holograms in Photographic Emulsions of Extended Thickness," Optics Communications, vol. 6, pp. 205-208, October 1972.

51. V. V. Aristov and V. Sh. Shektman, "Properties of Three-Dimensional Holograms," Soviet Physics Uspekhi, vol. 14, pp. 263-277, November-December 1971.

52. R. G. Zech, "Data Storage in Volume Holograms," Ph.D. Thesis, University of Michigan, 1974.

53. D. R. Bosomworth and H. J. Gerritsen, "Thick Holograms in Photochromic Materials," Applied Optics, vol. 7, pp. 95-98, January 1968.

54. T. K. Gaylord and F. K. Tittel, "Angular Selectivity in Lithium Niobate Volume Holograms," Journal of Applied Physics, vol. 44, pp. 4771-4773, October 1973.

55. S. F. Su and T. K. Gaylord, "Unified Approach to the Formation of Phase Holograms in Ferroelectric Crystals," Journal of Applied Physics, vol. 46, pp. 5208-5213, December 1975.

56. G. A. Alphonse, R. C. Alig, D. L. Staebler, and W. Phillips, "Time-Dependent Characteristics of Photo-Induced Space-Charge Field and Phase Holograms in Lithium Niobate and Other Photo-Refractive Media," RCA Review, vol. 36, pp. 213-229, June 1975.

57. W. D. Cornish, M. G. Moharam, and L. Young, "Effects of Applied Voltage on Hologram Writing in Lithium Niobate," Journal of Applied Physics, vol. 47, pp. 1479-1484, April 1976.

58. See, for example, R. F. Harrington, Time-Harmonic Electromagnetic Fields, McGraw-Hill Book Company, New York, 1961).

59. W. D. Cornish and L. Young, "Influence of Multiple Internal Reflections and Thermal Expansion on the Effective Diffraction Efficiency of Holograms Stored in Lithium Niobate," Journal of Applied Physics, vol. 46, pp. 1252-1254, March 1975.

60. D. M. Kim, R. R. Shah, T. A. Rabson, and F. K. Tittel, "Study of the Equivalent Electron Drift Field Characteristics in $LiNbO_3$ by Phase Holography," Applied Physics Letters, vol. 29, pp. 84-86, July 15, 1976.

61. R. S. Chu and T. Tamir, "Bragg Diffraction of Gaussian Beams by Periodically Modulated Media," Journal of the Optical Society of America, vol. 66, pp. 220-226, March 1976.

62. J. M. Moran and I. P. Kaminow, "Properties of Holographic Gratings Photoinduced in Polymethyl Methacrylate," Applied Optics, vol. 12, pp. 1964-1970, August 1973.

63. M. R. B. Forshaw, "Explanation of the Two-Ring Diffraction Phenomenon Observed by Moran and Kaminow," Applied Optics, vol. 13, pg. 2, January 1974.

64. M. R. B. Forshaw, "Explanation of the "Venetian Blind" Effect in Holography, Using the Ewald Sphere Concept," Optics Communications, vol. 8, pp. 201-206, July 1973.

65. T. Yasuhira, T. Morikawa, J. Shimada, and K. Sakurai, "Thermally Induced Bubblelike Patterns in Fe-Doped $LiNbO_3$ Single Crystals," Journal of Applied Physics, vol. 47, pp. 1229-1231, April 1976.

66. H. Kogelnik, "Filter Response of Nonuniform Almost-Periodic Structures," The Bell System Technical Journal, vol. 55, pp. 109-126, January 1976.

67. S. F. Su and T. K. Gaylord, "Time Evolution and Refractive-Index Profiles of Phase Holograms in Electro-Optic Crystals," Journal of the Optical Society of America, vol. 66, p. 1084, October 1976.

68. "Standards on Piezoelectric Crystals," Proceedings of the IRE, vol. 37, pp. 1378-1395, December 1949.

69. G. D. Boyd, R. C. Miller, K. Nassau, W. L. Bond, and A. Savage, "$LiNbO_3$: An Efficient Phase Matchable Nonlinear Optical Material," Applied Physics Letters, vol. 5, pp. 234-236, December 1, 1964.

70. M. L. James, G. M. Smith and J. C. Wolford, Applied Numerical Methods for Digital Computation with FORTRAN, International Textbook Co., Scranton, Pennsylvania, 1967, pg. 350.

VITA

Robert Magnusson was born in Reykjavik, Iceland, on July 15, 1948. He is the son of Magnus Halldorsson and Þorunn Juliusdottir. He was brought up by his grandparents, Julius Gudlaugsson and Sigridur Helgadottir, in the town of Gardur, Iceland.

He received the degree Bachelor of Science in Engineering from Florida Technological University in 1971. From 1972 to 1976 he was a Graduate Research Assistant and a Graduate Teaching Assistant in the School of Electrical Engineering at the Georgia Institute of Technology. In 1973, he received the degree Master of Science in Electrical Engineering from that institution.